Characterization of Onset and Transition to Instability in Supersonic Retropropulsion

Lauren Jones

A thesis
submitted in partial fulfillment of the
requirements for the degree of

Master of Science

University of Washington

2022

Committee:
Owen Williams
Carl Knowlen

Program Authorized to Offer Degree:

Aeronautics and Astronautics

University of Washington

Abstract

Characterization of Onset and Transition to Instability in Supersonic Retropropulsion

Lauren Jones

Chair of the Supervisory Committee:
Owen Williams
Aeronautics and Astronautics

There is a need in supersonic retropropulsion (SRP) to understand the characteristics of shock unsteadiness and the parameters that determine transition to unsteady regimes. Data collected in the NASA Unitary Wind Tunnel[1] were studied to determine instability characteristics in shocks as angle of attack, Mach number, and nozzle configuration was varied. Data were also collected at the University of Washington in order to better understand the point at which a shock will transition from steadiness to unsteadiness as forebody size, gas combination, and jet Mach number vary. The transition data taken at UW consisted of nozzle forebody diameters at 1/8 inch, 1/4 inch, and 3/8 inch nozzles at both Nitrogen-Nitrogen and Carbon Dioxide-Helium gas combinations, with several Carbon Dioxide-Helium 1/8 inch nozzle cases taken at a freestream Mach of 3. Shock standoff distance and oscillation amplitude was increased with increasing forebody diameter and increasing freestream Mach number. Carbon Dioxide-Helium cases also exhibited both higher oscillation amplitude and shock standoff distance than corresponding Nitrogen-Nitrogen cases. Transition to unsteadiness occurred at lower pressures than previously thought: between P_e/P_{02} of 0.2 and 0.8, depending on forebody diameter, gas combination, and freestream Mach number. Transition to unsteadiness does not always follow the previous predictions of a total pressure ratio unity or P_e/P_{02} of 1. A range of unsteadiness modalities was observed, including bimodal unsteady cases and cases exhibiting intermittent unstable behavior.

TABLE OF CONTENTS

LIST OF FIGURES

NOMENCLATURE

α: Angle of attack

A_B: Area of the forebody

A_E: Area of the jet exit

C_T: Thrust coefficient

D_B: Diameter of the forebody

D_E: Diameter of the jet exit

F: Focal length of a lens or a mirror

H: Shock Standoff Distance

M: Mach number

P_J: Jet exit pressure

P_E/P_{02}: Jet exit pressure to jet stagnation pressure

$P_{0J}/P_{0\infty}$: Jet total pressure to freestream total pressure

P_{EJ}/P_{∞}: Jet exit pressure to freestream pressure

Q: Dynamic pressure

T: Jet thrust

ACKNOWLEDGMENTS

First and foremost, I would like to thank my research advisor, Owen Williams. I could not have completed this work without your guidance and encouragement. You pushed me to improve, to set and reach my goals, and to care for every detail. I would also like to thank my dearest friends and fellows in my research, Elliot Jennis and Hariprasad Annamalai. You both provided friendship and laughter through the most difficult parts of these two years. We shared frustration, joy, and companionship and I would not have made it without you two.

DEDICATION

To my mom, for your constant love and comforting hugs.

To my dad, who pushes me and always cheers me on.

To Kathryn and Matt, who will support me through anything.

And to Graham, who I hope will grow up to love aerospace as much as I do.

Chapter 1

INTRODUCTION

As demand grows for continuing advances in space technology launch capabilities, the launch rate of vehicles into orbit and to other planets is increasing. Entry, descent, and landing (EDL) technologies are continually becoming more important as with each successive mission, payload size and weight grow, testing the limits of current EDL technology. Supersonic retropropulsion (SRP) is a method of rocket and spacecraft deceleration where engines are fired into the oncoming flow. While conceptualized and investigated as far back as the 1960s [4, 13], interest in this technology has received significant growth in recent years. It is viewed as an enabling technology for return and reuse of first-stage rocket boosters and has the ability to decelerate large payloads within thin atmospheres such as those found on Mars. SRP benefits from employing relatively simple hardware, as only one system is needed to decelerate the vehicle throughout EDL. In addition, the systems needed, such as heat shielding and engines, are already considered robust, readily available, and scalable for almost any size mission.

One area of SRP studies that requires further exploration are the onset and mechanisms underpinning shock instabilities present in the flow field. It is difficult to predict when the onset of instability can be expected and how changing flowfield or hardware parameters will affect the type of instability present. Since the source of this instability is still unknown, the ability to mitigate unstable shocks is not well developed. The flow field surrounding the jet exit nozzle of an SRP system is complex, but there are several known regimes of unsteadiness, including shock oscillation, shock flapping, and shock penetration. This unsteadiness is undesirable due to the negative effects dynamic loading can have on a vehicle structure and its controls.

Korzun and Cassel [6], from the data gathered in Berry [1], concluded that instability can be expected when two conditions are met: the pressure at the exit of the nozzle is greater than the post-shock stagnation pressure and the thrust coefficient exceeds unity. Ho [5] and Yang[14] collected data at the University of Washington and found that at total pressure ratios of 0.5 and 5, shocks were steady, while at a total pressure of 1, the shock exhibited either bow shock penetration or oscillation. Romeo and Sterrett[15] also noted a dependence in transition to unsteadiness based on total pressure ratio, with the critical total pressure ratio being around 7. Finding a conclusive, predictable transition point from steady to unsteady shocks is crucial for instability mitigation in EDL technologies.

Questions have been raised through these past studies, which this thesis will aim to address, such as: How does each changing parameter affect unsteadiness characteristics, including angle of attack, Mach number, and coefficient of thrust? How does the jet-to-forebody diameter affect unsteadiness and its onset? Can the onset of unsteadiness be predicted across any SRP flow? This study utilizes SRP data taken by NASA in the unitary wind tunnel over a range of Mach numbers, angles of attack, and coefficients of thrust in order to better characterize the regimes of unsteadiness seen. Transitions between types of unsteadiness were found to depend upon nozzle configuration and coefficient of thrust primarily, with amplitude of unsteadiness being highly dependent upon angle of attack. The transition regions for each case varied greatly, suggesting that previous expectations of where transition occurred were incorrect.

Chapter 2

BACKGROUND & THEORY

2.1 Types of Instability

Supersonic retropropulsion experiments have been categorized by type of unsteadiness as early as Romeo & Sterrett [3] in 1963. Cases are typically classified as being steady, oscillating, or exhibiting the a shock penetration mode. In penetrating cases, the shock is often pushed several nozzle diameter lengths in front of the nozzle face and the jet flow penetrates the bow shock. Figure 2.1 compares a steady shock, on the left, to a shock exhibiting the long penetration mode, on the right [2]; cases exhibiting the long penetration mode typically have a high coefficient of thrust.

2.2 Onset of Instability

Romeo & Sterrett[3] characterized instability by plotting Mach number against total pressure ratio, as shown in Figure 2.2. They found that the long penetration case occurred to the left of the line shown, at low total pressure ratio values, and the stable cases occurred to

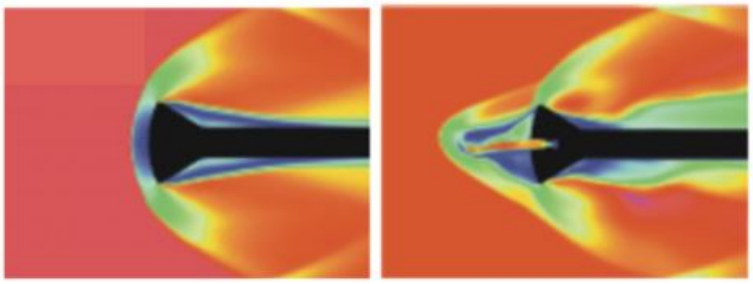

Figure 2.1: Steady shock (left) and long penetration mode (right), Ho[2]

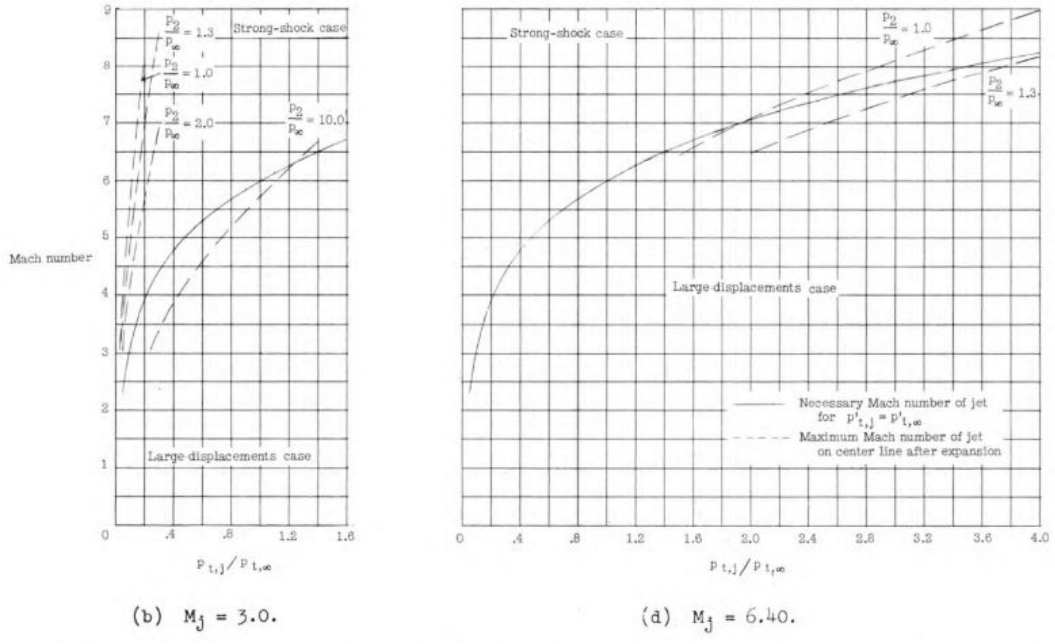

Figure 2.2: Shock transition to instability, Romeo & Sterrett[3]

the right of it, with higher total pressure ratios. Jarvenin & Adams[4] later used a metric called the engine scaling parameter (ESP) to look at the shift from a steady shocks to an unsteady shock. Shown in Figure 2.3, the transition line between shock penetration and a steady shock is at a pressure ratio around 7. Both of these plots will be recreated using the data utilized in this study to verify these findings.

Ho [5] studied the effects of nozzle forebody size on the SRP flowfield. This study found that the appearance of either bow shock oscillation or shock penetration depended on the forebody size and jet pressure. At a nozzle diameter of 1/8 inch, as stagnation pressure ratio was increased, the RMS band thickened and a bulge directly in front of the nozzle formed, as shown in Figure 2.4, resulting in a shock penetration mode for the higher pressure cases. The 1/4 inch nozzle and 3/8 inch nozzle proved to have a similar trend with increasing stagnation pressure ratio. As forebody size decreased, there was a shift from bow shock oscillation to bow shock penetration, proving a relationship between forebody size and the unsteadiness

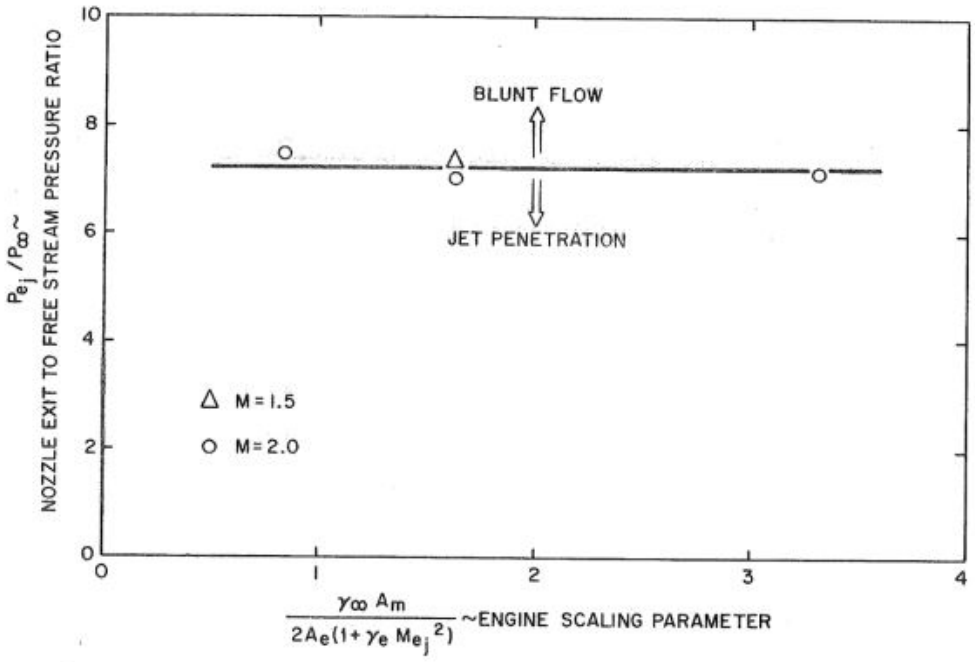

Figure 2.3: Engine scaling parameter plot,Jarvenin & Adams[4]

regime for the nozzle. Yang[14], who looked at the transition to unsteadiness using the same set of forebody and total pressure ratio combinations, concluded that at a total pressure ratio of unity for each case tested, unsteadiness was present. This finding coincides with Shang et al.'s [9] conclusion that P_{crit} for any case falls between a pressure ratio of 0.8 and 1.05. Korzun and Cassel[6] found that shock standoff increased along with coefficient of thrust, with the exception of low C_T cases, in which there was a jump in the shock standoff distance for the data taken by Jarvinen Adams[4]. The data from Berry[10] in this figure was taken with a different forebody diameter size, freestream Mach number, and jet Mach number, potentially causing the shock standoff distance not to increase drastically at low C_T. This figure does, however, support their hypothesis that self-similarity exists for under-expanded nozzle flows when P_e/P_{02} exceeds unity. The abrupt change in shock standoff distance in the Jarvinen data suggests that the jet flow becomes under-expanded at low C_T values.

In general, at very low coefficient of thrust values, the shock can be expected to be steady. With an increase in C_T, the flow tends to become unsteady, which may present in the form of shock oscillation, flapping, penetration, or any combination of these instability regimes. At high C_T values, the flow transitions back to producing a steady shock. This unsteady shock phenomenon is shown in Figure 2.6. While the exact C_T values each transition occurs at are currently unknown, this study will attempt to better quantify how shock unsteadiness is onset and evolves as parameters of the flow change. Unsteadiness in the NASA dataset and transition data taken in the following sections exhibited primarily shock oscillation, the motion of the shock forward and backward from the nozzle. Many of these oscillating cases also exhibited flapping, where the shock billowed periodically from the front point of the shock down to where the shock and the shear layer intersect. Some cases exhibited oscillation in conjunction with shock penetration, where the shock both moved forward and backward, as well as being penetrated by the jet flow.

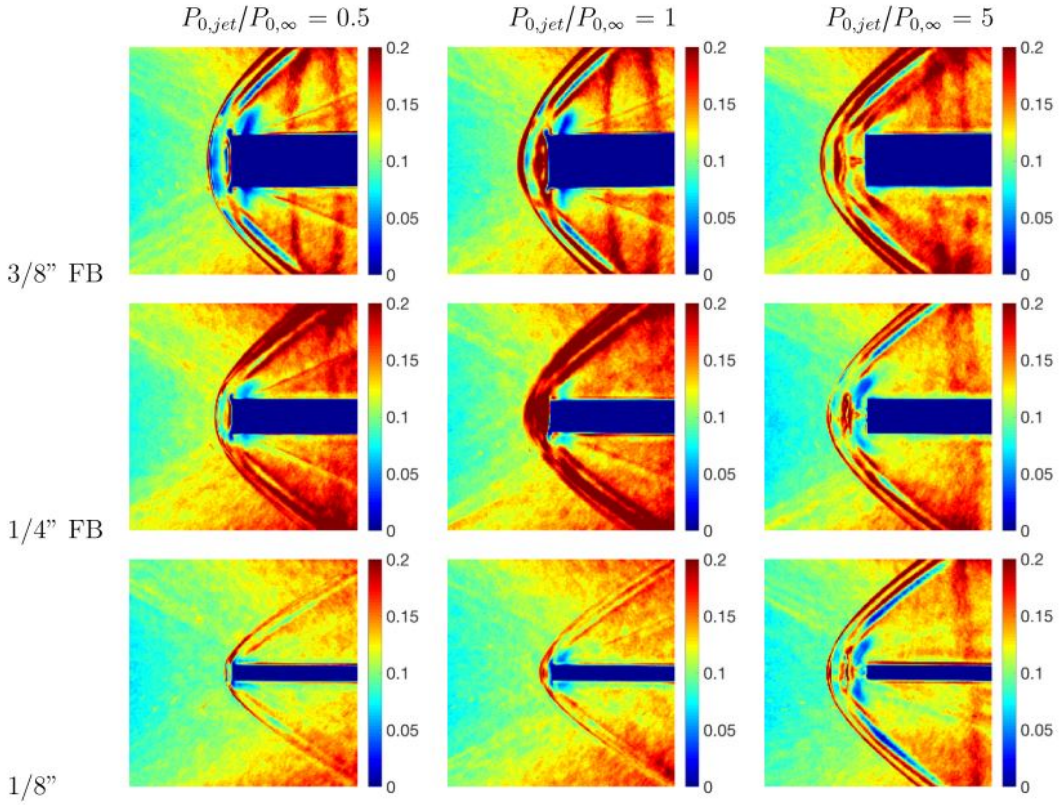

Figure 2.4: RMS images for each forebody tested by Ho [5] at stagnation pressures of 0.5, 1, and 5.

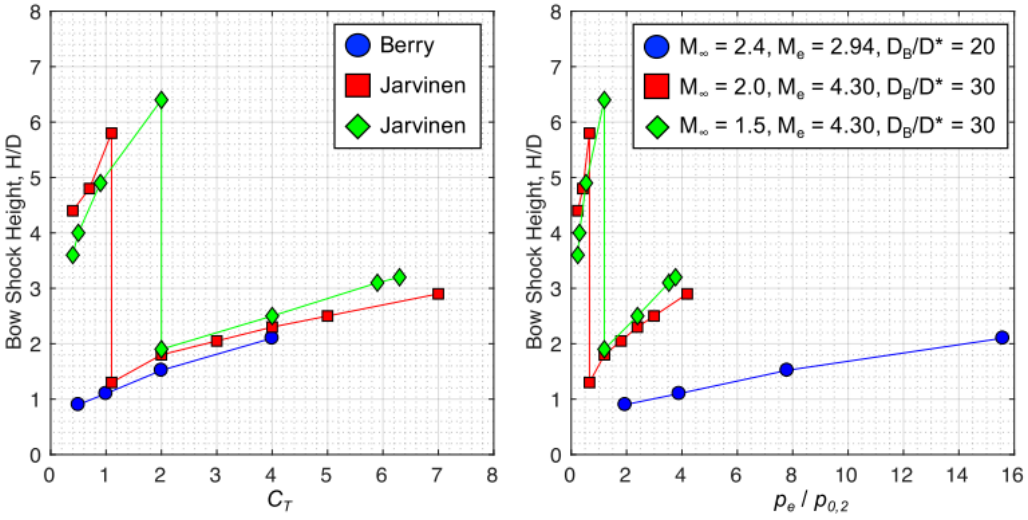

Figure 2.5: Shock standoff distance displaying jump in H/D at low C_T [6].

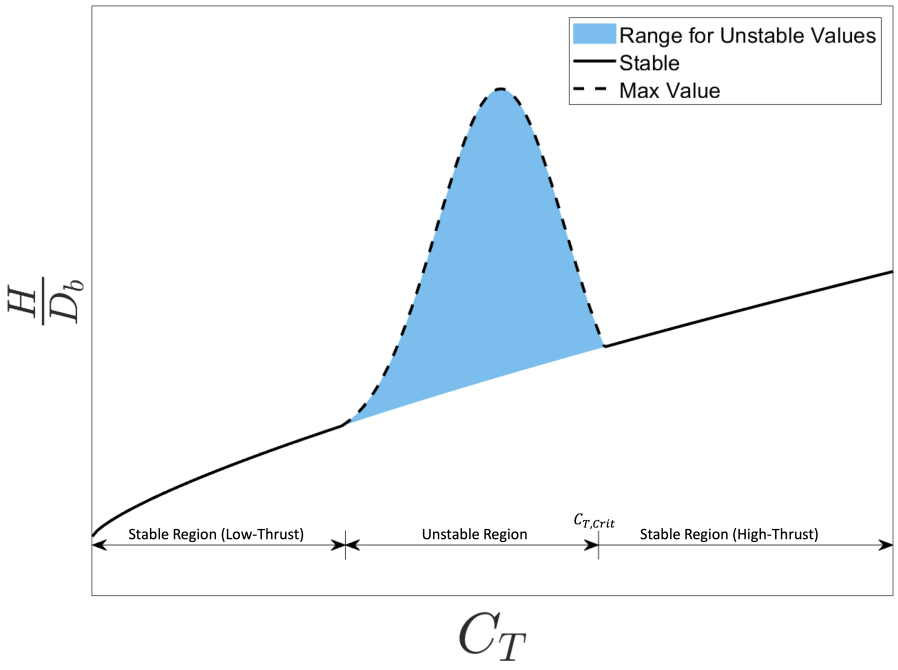

Figure 2.6: Flow topology describing the shift from stable shock to unsteady shock and back to stable.

2.3 NASA Dataset

Extensive SRP data was taken in the NASA Langley unitary wind tunnel using center, tri-, and quad-nozzle configurations at angles of attack ranging from -8 to 20 degrees, coefficients of thrust from 0 to 6, and freestream Mach numbers at 2, 3, and 4. Nozzle geometry and a nozzle section view from the nozzle used in this study is shown in Figure 2.7. Berry [1] [16] found that for center nozzle cases, the bow shock became unsteady above 10-degrees angle of attack and the predominant frequencies of motion were between 1.7 to 2.3 kHz. The tri-nozzle was found to be more unsteady overall than the center nozzle configuration as well as having shorter shock standoff distances. Unsteadiness tended to increase with increasing Mach number. Quad nozzle cases were stated to provide mixed results, where some cases were steadier than their corresponding tri-nozzle cases and some were not. A more extensive look at how the parameters presented in this dataset affect unsteadiness will be detailed later in this paper.

Using the Mach 4.6 cases from this same dataset, Codoni [17] conducted a frequency analysis using Welch's method. This study looked at center nozzle cases at thrust coefficients of 0.2, 0.46, 0.9, and 1.97 and angle of attack ranging from -8 to 20 degrees to find peak frequency characteristics. The coefficient of thrust 1.97 runs had the highest and sharpest frequency peaks. The shape of frequency peaks was found to suggest periodicity, where sharp, distinct peaks suggest a frequency with periodicity of the unsteady nature of the flow while a flatter, more broad peak is aperiodic. An angle of attack dependency was also found where for angles from 0 to 8 degrees, peaks were sharper and more distinct, while at angle of attack 12 and above, peaks were broader, suggesting they were aperiodic. Tri-nozzle cases with similar C_T values and angles of attack were studied, showing that tri-nozzle peaks occur at lower frequencies than their corresponding center nozzle cases. Peaks are typically smaller and broader, suggesting aperiodicity. Quad nozzle trends were more complex, as at C_T 0.91, peaks were similar to those of tri-nozzle cases: small and broad. At C_T 1.92, the frequency peaks followed similar trends to the center nozzle case, where from angle of attack 0 to 8 peaks

were sharp and tall, at 12 degrees and higher, peaks became flat and broad, indicating an aperiodic nature of the unsteady flow. Codoni[18] later conducted another frequency study that revealed similar findings, stating more simply that for center nozzle cases as angle of attack increases, peak frequency location decreases and peak structure changes, suggesting that this may be due to the characteristic length increasing.

Bathel [19] used the same nozzle plenum and wind tunnel as the Codoni papers, but at Mach 10. In this study, peak frequencies were found to all be around 2 kHz, which corresponds to the peak frequencies found in Codoni. This suggests that peak frequency may always be around 2 kHz, independent of freestream Mach number. Bathel also suggests that this peak frequency is independent of jet pressure ratio for the nozzle configuration used.

2.4 Instability in Spiked Body Nozzles

While shock unsteadiness in nozzles with a spiked body differs from the unsteadiness present in blunt nozzle shocks, the physics of the flow is similar in many ways. The mechanisms for why unsteadiness occurs in a spiked body nozzle can give an insight into why unsteadiness is present for blunt nozzles as well. In an oscillating case for a spiked body nozzle, the bow shock exhibits a periodic flapping motion throughout the run of the jet. Shock oscillation consists of three phases: collapse, withhold, and inflation[20]. Figure 2.8 [7] shows these three phases for a flat forebody nozzle with a spike. This periodic process consists of charging along the separated shear layer and mass ejection at the end of the shear layer by way of large scale structures. The cycle begins when detached shocks (or shocklets) are generated at the separation point, near the front of the spiked body. These shocklets, along with eddies, propagate downstream towards the base of the spike, where the reattachment point is located. As the large scale structures move downstream to the re-circulation zone, they grow, carrying mass. This creates a cone around the base of the spike. When the large scale structures and shocklets come into contact with the reattachment shock, the shocklet hits the forebody and bounces off, creating a reflected shock that moves back and forth between

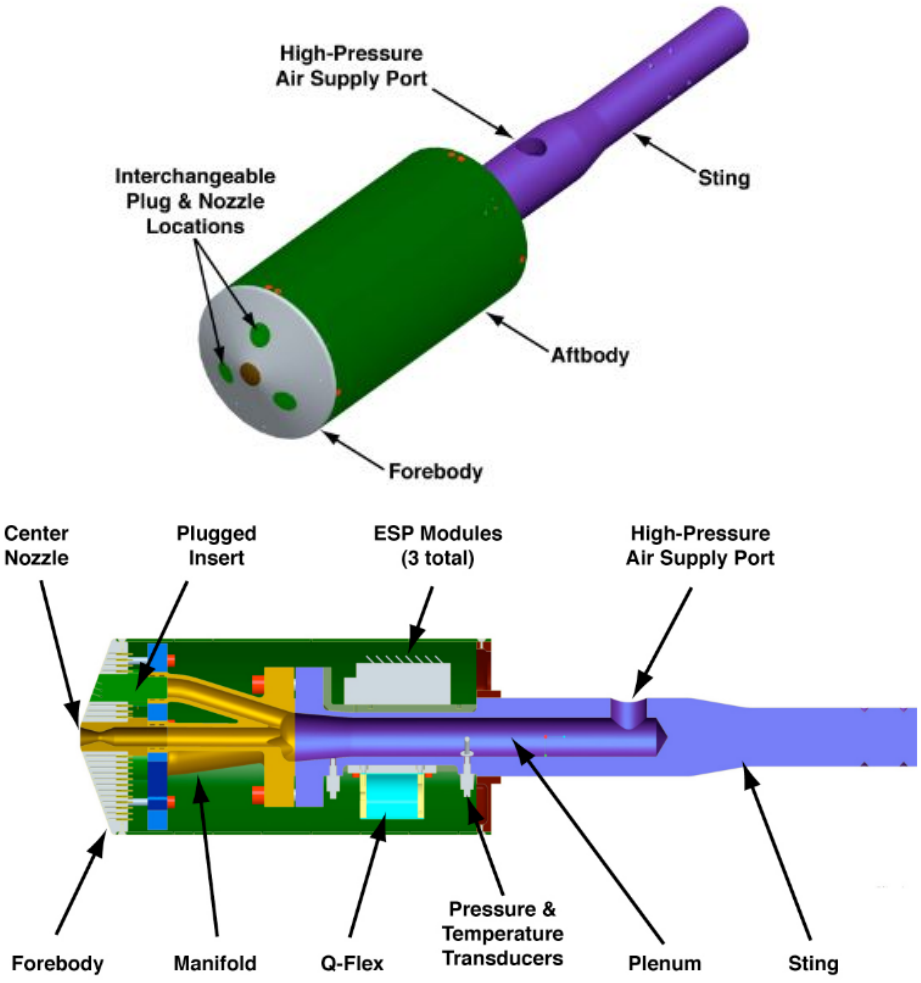

Figure 2.7: NASA nozzle geometry and section view[1].

the separation and reattachment points. When the reflected shocklets come into contact with the original, incoming shocklets, both velocities are affected. Along with this, when the large scale structures come into contact with the reattachment shock, the shock is displaced. Due to these interactions, fluid mass is ejected from the re-circulation bubble out into the freestream, forcing an opening between the shock and the edge of the forebody for the mass to exit through. The reflected waves continue to travel upstream towards the separation point, continuing to come into contact with the incoming shocklets, which disturbs the separation point, causing more large scale structures to form and travel downstream, continuing the instability. This describes why, with a larger forebody, the flow tends to oscillate more. When the forebody is smaller, the mass does not need to create an opening for ejection, however, with a larger forebody, the shock will oscillate and flap quite a bit to create this opening.

Shang et al. [9] found that any disturbance to this feedback loop will interrupt the instability cycle. A disturbance to the feedback loop could also be caused by raising the stagnation pressure ratio between the freestream and the counter-flow jet. Figure 2.10 shows particle traces of an open and closed feedback loop created by Shang. This explains why at lower pressure ratios, the bow shock tends to oscillate and when the pressure ratio is increased, the flow becomes steady. Shang found the transition pressure ratio, P_{crit} for a freestream of Mach 6 and a nozzle exit of 254 mm to be 0.9, but predicted that for any case, the transition is expected to be between 0.8 and 1.05.

Qin et al. [7] studied the instability and asymmetry of the flow in cases with a non-zero angle of attack by collecting pressure data on the windward and leeward sides of a nozzle. The pressure sensor on the windward side of the nozzle recorded a higher pressure than that of the leeward side. Therefore, the shear layer on the leeward side of the nozzle does not reattach to the edge of the forebody, as it does on the windward side, where the resulting reattachment shock becomes stronger, as seen on the bottom portion of the nozzle in Figure 2.11. Any air entering the dead-air region, whether on the leeward or windward side of the nozzle, must be ejected on the leeward side. Figure 2.11 shows two colored streamlines,

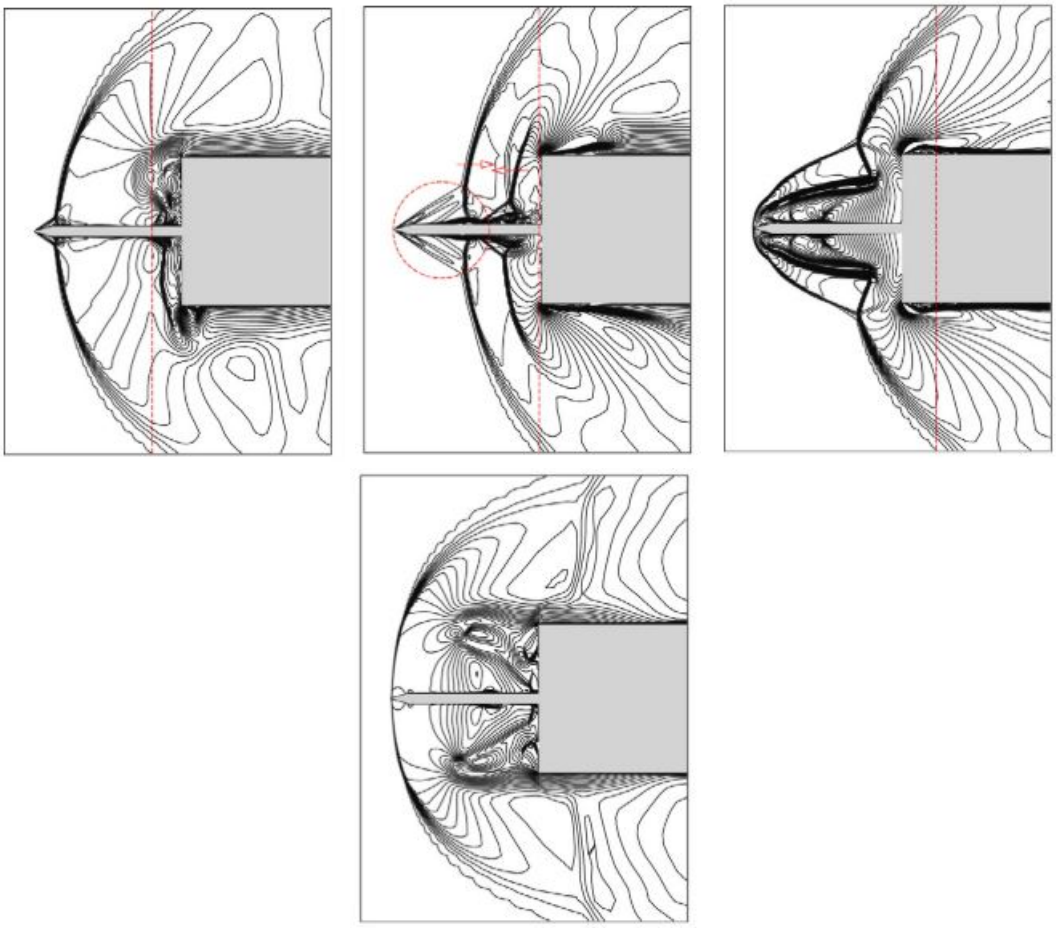

Figure 2.8: Shock Oscillation Phases: Collapse, Withhold, Inflation-Qin[7].

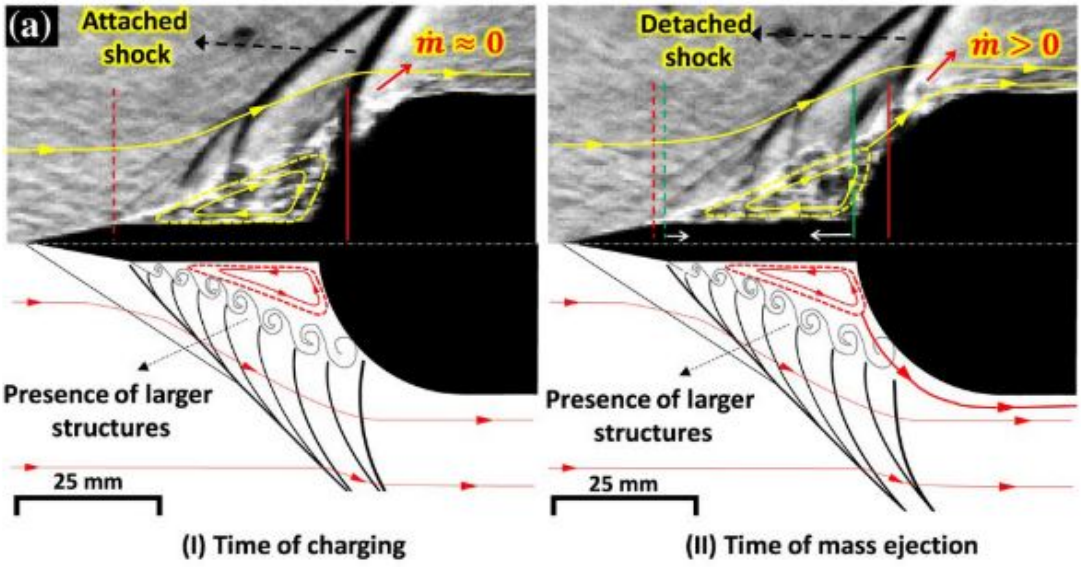

Figure 2.9: Instantaneous snapshots showing the motion of separation shock and reattachment shock during the time of charging and ejection, Sahoo[8]

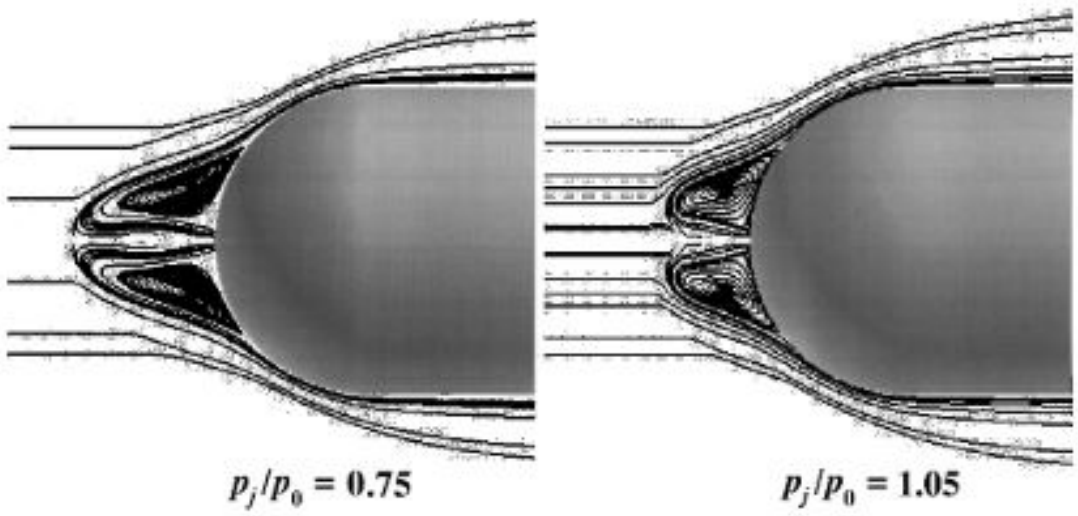

Figure 2.10: Closed feedback loop (left) and open feedback loop (right)-Shang[9]

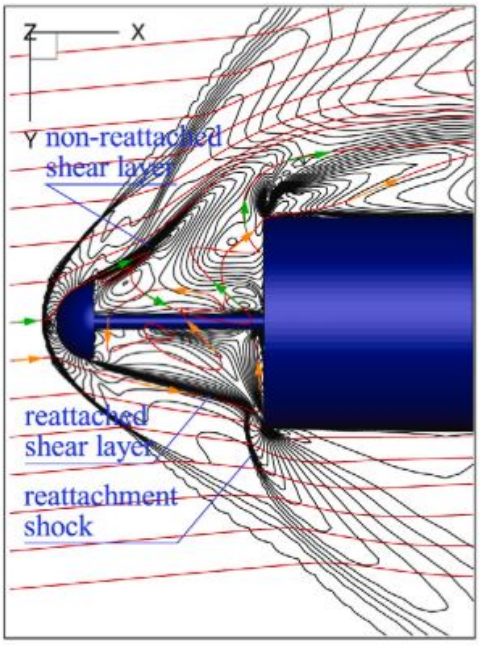

Figure 2.11: Streamlines around an angled nozzle, Qin[7]

representing paths through the dead-air region. The green streamline enters on the leeward side of the spike and the orange enters on the windward side. Both streamlines travel into the dead-air region, are caught in various upstream and downstream directions, and are ejected on the leeward side of the forebody, causing an asymmetric flowfield around the nozzle.

2.5 Scaling Parameters

There are several pressure ratios utilized in this paper to discuss trends in unsteadiness. The ratio of jet exit pressure to jet stagnation pressure is denoted by P_e/P_{02}. The total pressure ratio, or stagnation pressure ratio, is denoted by $P_{0j}/P_{0\infty}$. The nozzles are described by either the ratio of forebody area to nozzle exit area, A_b/A_e or the ratio of forebody diameter to nozzle exit diameter, D_b/D_e. The jet thrust coefficient, C_T, combines both the pressure ratio of the SRP flow and the area ratio of the nozzle. The definition of C_T is

$$C_T = \frac{T}{q_\infty A_b} \tag{2.1}$$

and it is found by

$$C_T = \frac{c_t p_{0j} A^*}{q_\infty A_{ref}} \tag{2.2}$$

The engine scaling parameter (ESP) describes the flow conditions using the heat capacity ratio, area ratio, and jet exit Mach number and is found by

$$\frac{\gamma_\infty A_b}{2A_e(1 - \gamma_\infty M_e^2)} \tag{2.3}$$

The mass flux ratio, a parameter combining area ratio and velocity of the flow, is calculated by

$$\frac{\rho_e U_e A_e}{\rho_\infty U_\infty A_b} \tag{2.4}$$

As forebody areas, exit and freestream Mach numbers, and pressure ratios vary across differing datasets, these scaling parameters will provide direct comparison in the attempt to identify characteristics and transition points of unsteadiness.

Chapter 3

EXPERIMENTAL FACILITIES & METHODS

3.1 UW Ludweig Tube

3.1.1 Facilities

The data gathered at the University of Washington for this study was collected using a 10 foot Ludwieg shock tube capable of producing Mach 2 freestream flow from a 2 inch exit diameter for a run time of approximately 16 ms. Nitrogen and Carbon Dioxide freestream gasses were used, as well as Nitrogen and Helium retrojet gasses. The arrangement of the Ludwieg tube and retrojet nozzle can be seen in Figure 3.1. A double diaphragm system was used for this tunnel. The Ludwieg tube 3-meter long driver section is filled to the desired test pressure for the freestream gas up to the first of two diaphragms made of 4 mil-thick Mylar. The desired test pressure for perfectly expanded freestream flow is 124 psig for Nitrogen and 115 psig for Carbon Dioxide. The chamber in between the two Mylar diaphragms is pressurized to approximately half the driver section pressure in order to create a barrier between the tube section and the room at ambient pressure. To trigger the start of the flow, the chamber between the two diaphragms is opened, depressurizing this section and causing the Mylar diaphragms to burst.

Schlieren imaging of the tests was taken using a high-speed camera. Like many SRP experiments, schlieren photography was chosen because it can show spatial variations in density, making visualization of shock dynamics possible. A schematic of the schlieren system used is shown in Figure 3.2. An LED light source pulsing at a rate of 1 micro-second(μs) was paired with the camera frame rate using a BNC Model 565 Pulse/Delay Generator. This light source was developed by Yang [14] and also used in Ho [5]. Images were captured with a Vision Research Phantom v641 high-speed camera using a 105 mm lens. The produced

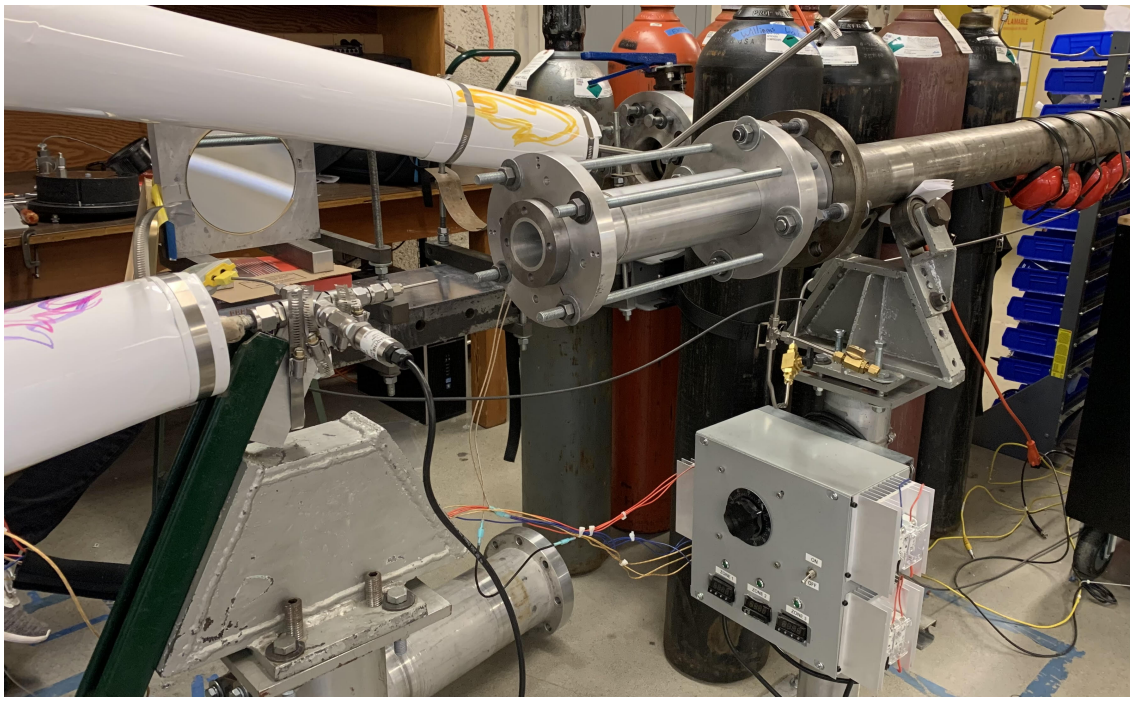

Figure 3.1: Ludwieg tube used for SRP testing

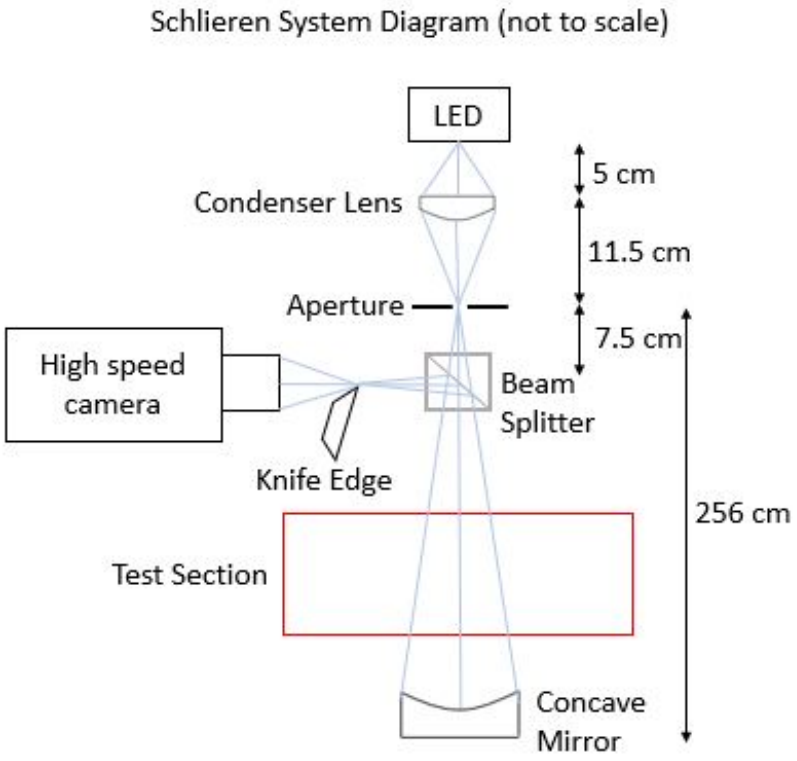

Figure 3.2: Schematic of the schlieren system used for SRP data collection

image resolution was 208 pixels by 240 pixels with an exposure time of 1.76 μs and a frame rate of 31,000 frames per second. The light produced by the LED passed through a condenser lens with focal length of 115 mm and then to a pinhole which was placed at the focal length of the condenser lens. The beam then passed through the test section and was reflected by a concave mirror with a focal length of 256 cm. The beam returned along the same path to a 50:50 beam splitter which reflected the light 90 degrees into the camera lens. A knife edge, necessary for showing changes in density, was placed vertically between the beam splitter and camera lens.

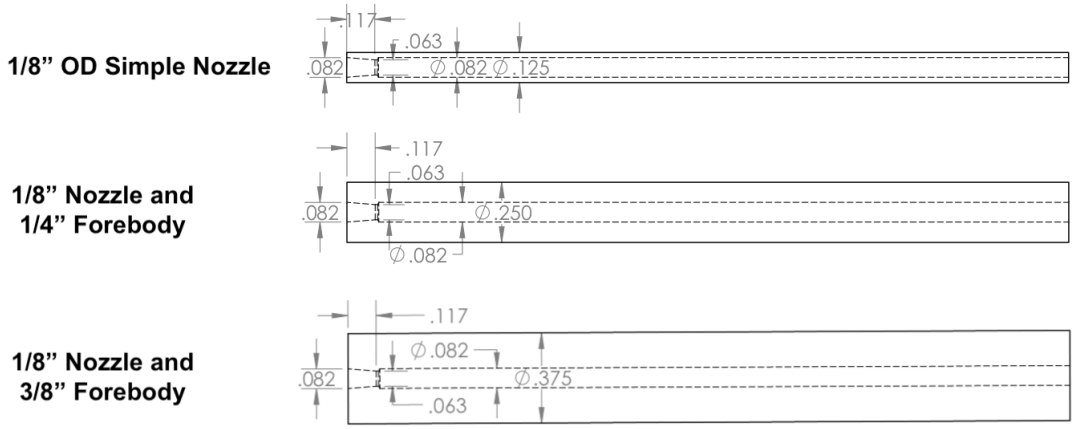

Figure 3.3: Mach 2 retro-nozzles used for this study. These are conical, with a four degree divergence angle. The nozzles depicted are for nitrogen gas. Similar nozzles were created for other gasses but with different minimum exit areas.

3.1.2 Test conditions

Two Mach 2 gas combinations were chosen for this study: Carbon Dioxide freestream with a Helium retro-gas and Nitrogen freestream with Nitrogen as the retro-gas. Three nozzle types were tested for each of the gas combinations, depicted in Figure 3.3. The outer diameters of the three nozzles chosen were 1/8 inch, 1/4 inch, and 3/8 inch, which is how each nozzle type will be referred to throughout this paper. Cases for Nitrogen-Nitrogen using the 1/8 inch nozzle were also taken at Mach 3 and at Mach 3 with the retro-gas heated to 170 $^{\circ}$F. A range of pressure ratios for each test case were chosen in order to find the transition point for each case between the steady and unsteady regimes, typically starting around P_e/P_{02}=1 and dropping incrementally until an unsteady shock was produced.

Nozzle Forebody Diameter	Gas Combination	Mach Number
1/8 inch	CO2He, NiNi	Mach 2, Mach 3
1/4 inch	CO2He, NiNi	Mach 2
3/8 inch	CO2He, NiNi	Mach 2

3.1.3 UW Data Analysis Methods

The video data taken during each shock test was collected by Vision Research software, which was output in a cine format. The raw data was transferred to a matlab file in order to be processed for analysis. The bad frames of each video, including frames at the start and end of the tube burst where the flow was not fully formed and frames where pieces of Mylar from the diaphragms were present were cropped out of the data file. A code for stabilization of the nozzle was then used, as each run contained some amount of nozzle motion due to the strength of the flow. This code detected the front of the nozzle in each frame and centered the frames around the center of the nozzle front. This did, as a result, crop portions of the edges of the video frames, however, these cropped pieces of each frame were negligible. The collected video frames were then normalized by the mean background intensity of the video. For the mean and root mean squared (RMS) images for each case, the gradient magnitude of each frame of data was taken in order to assess how quickly the image is changing in time. RMS images were found by subtracting the mean of each video from each frame and scaling the pixel intensity to values between 0 and 1; these images describe the amount of motion an area of the image sees throughout a full video.

This scaling of the pixel intensities provided a consistent pixel intensity range for each case in the full dataset. For the amplitude calculations, a threshold of desired pixel intensity was created in order to visualize only the regions of high motion of each test case. A consistent threshold value was found and a mask was created around the regions of the image that held pixel intensities below that threshold. Figure 3.7 shows an RMS image before a threshold mask was applied, along with three masked images of varying threshold values. The masked image with a threshold value of 0.65, Figure 3.7c, shows the threshold value used for amplitude calculations for each case in this dataset. This image contains only the white and bright yellow regions after the mask was applied, which indicates areas of high flow motion throughout a test run. The mask at a threshold of 0.6 leaves darker orange regions which do not all represent heavy shock motion, while the threshold of 0.7 masks over

a large portion of important motion. To get a quantitative shock amplitude value from this, the remaining unmasked pixels were added together and divided by the total pixel size of the image to produce a percentage of unmasked pixels representing the shock amplitude of the case. This method provided a consistent basis of shock amplitude that could be compared across each case taken.

To get the shock standoff distance, H, normalized by the forebody diameter, D, in steady shock cases, the mean image of the case was used. The distance in pixels from the front of the nozzle forebody to the front of the shock in the mean image was found, shown in Figure 3.4, along with the diameter of the nozzle in pixels. The shock standoff distance, H, was divided by the forebody diameter size in order to obtain the normalized shock standoff distance of each case. Unsteady shock cases were less straightforward. In these cases, the distance from the front of the nozzle forebody to the front of the shock in the instantaneous video frames where the shock was at its maximum and minimum locations were used. These maximum and minimum shock location values were averaged to obtain H, in pixels, as shown in Figure 3.5. The shock standoff distance was then normalized by the nozzle forebody diameter, D, in pixels. The errorbars for the shock standoff plot, shown in Figure 4.8, represent the maximum and minimum shock locations measured using instantaneous shock images. For the Carbon Dioxide-Helium 3/8 inch nozzle case and the two Carbon Dioxide-Helium 1/8 inch nozzle cases with the jet Mach number of 3, the front of the shock during parts of the shock oscillation were out of the frame of the video. The mean shock location for these cases, therefore, was calculated at the far left side of the image and both the maximum and minimum errorbars represent the distance from the left side of the image frame to the minimum shock location.

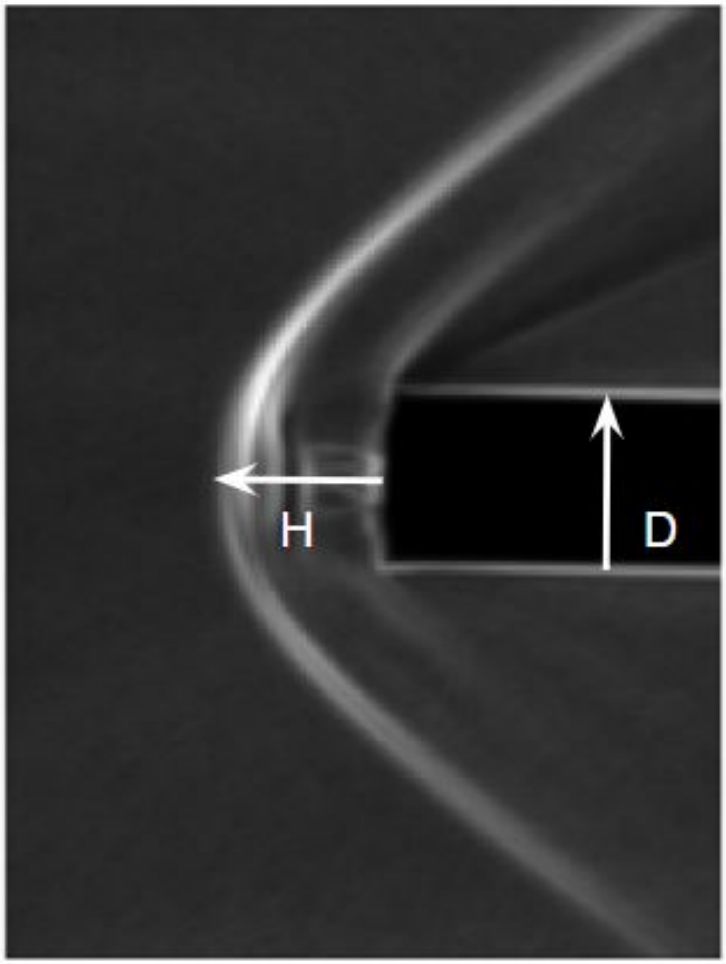

Figure 3.4: Shock standoff distance definition for steady shock cases. This value was normalized by the nozzle forebody diameter to obtain H/D.

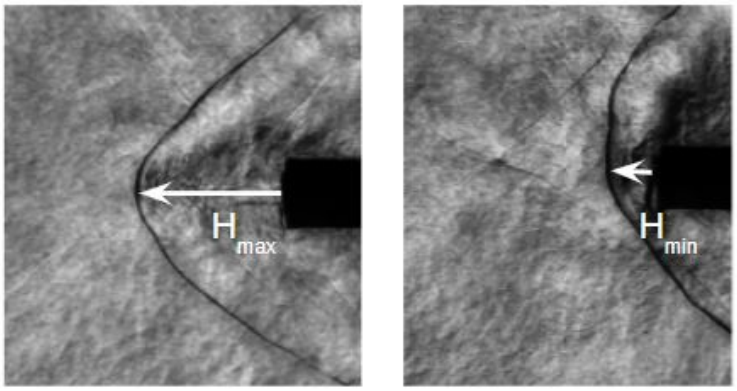

Figure 3.5: Shock standoff distance definition for unsteady shock cases. Left: maximum shock standoff distance location. Right: minimum shock standoff distance location. These values were averaged and normalized by the size of the nozzle diameter to obtain H/D.

3.2 NASA Unitary Tunnel

3.2.1 Facilities

The NASA data used in this study were taken at the NASA LaRC Unitary wind tunnel, a closed-circuit continuous flow tunnel with a 4-ft by 4-ft cross section. The Mach number range this tunnel is capable of is 1.50 to 4.63, between its two test sections. Figure 3.8 shows the flow conditions for each of the three Mach numbers used: 2.4, 3.5, and 4.6. The nozzle used is shown in Figure 2.7, having a D_b/D_e of 20 and a diameter of 5 inches. It is capable of several nozzle configurations by varying the plugs in the nozzle face, as shown in Figure 2.7. The sting holding the nozzle is capable of producing an angle of attack of up to $\pm$20-degrees. Additional equipment and instrumentation information can be found in Berry[10].

3.2.2 Dataset Parameters

The NASA data used in this study consisted of three nozzle geometries: center, tri, and quad. Angles of attack range from +0 to +20 degrees, in increments of four. Coefficient

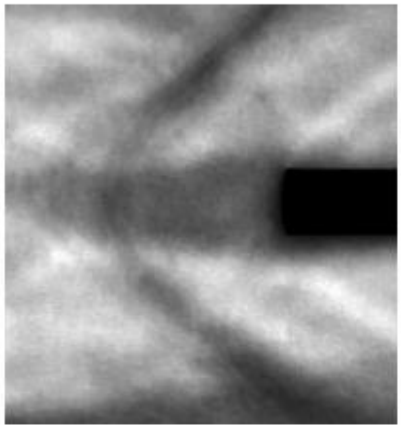

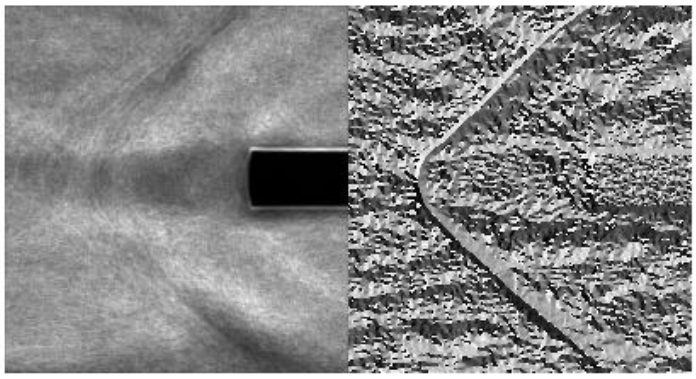

Figure 3.6: (a) Gradient image results, gradient magnitude(left) and gradient direction(right). (b)Raw mean image, CO2-He 1/4 inch nozzle unsteady case.

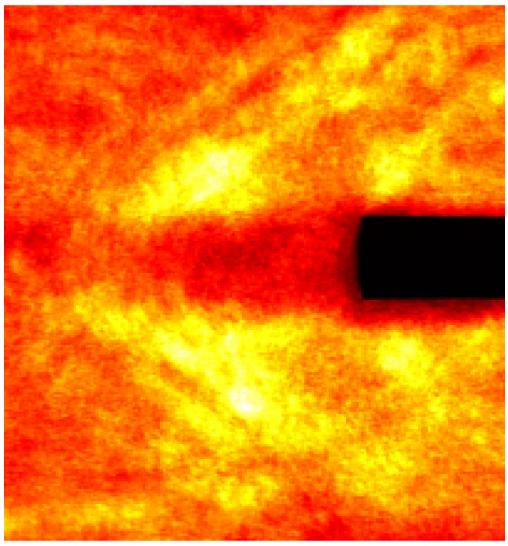

(a) Raw RMS Image

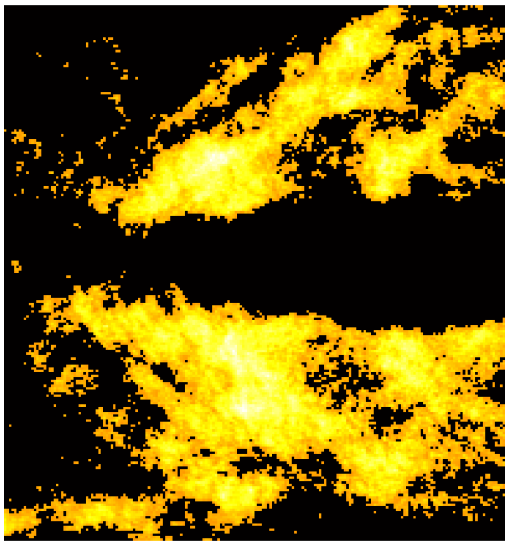

(b) RMS, Threshold=0.6

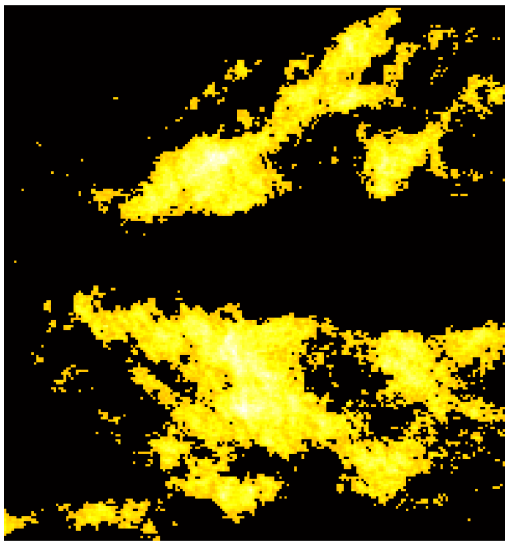

(c) RMS, Threshold=0.65

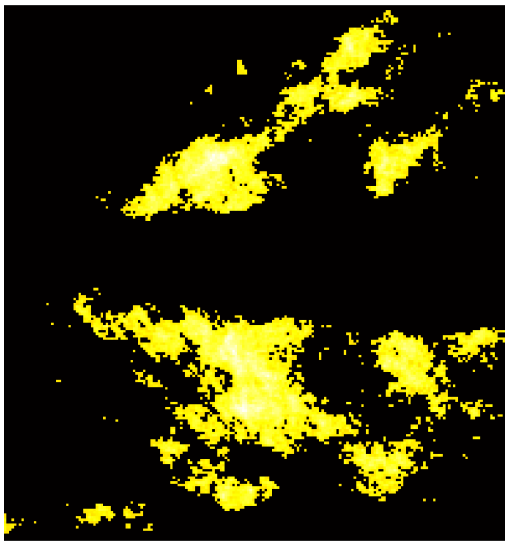

(d) RMS, Threshold=0.7

Figure 3.7: RMS Images with varying threshold masks, CO2He 1/4 inch nozzle, unsteady.

M_∞	Re_∞ (1/ft)	$T_{T\infty}$ (deg-R)	$P_{T\infty}$ (psf)	P_∞ (psf)	q_∞ (psf)
2.4	1.0E+06	610	814.9	55.7	224.7
3.5	1.0E+06	610	1485.8	19.5	167.0
4.6	1.5E+06	610	3922.1	12.0	177.3

Figure 3.8: Nominal Unitary Plan Wind Tunnel test section flow conditions, Berry[10].

of thrust values ranged from lower values around 0.25 and 0.5 up to 6 and includes only matched gasses. All variables used in this dataset are shown in Table 3.2.2.

NASA Dataset Parameters	
Angle of Attack	0,4,8,12,16,20
Thrust Coefficient	0.2,0.5,1,2,3,4,5,6
Freestream Mach	2.4,3.5,4.6
Nozzle Type	Center, Quad, Tri

3.2.3 NASA Data Analysis Methods

A challenge with the interpretation of schlieren data is due to the relative angle of the cutoff optical element and the angle of attack, α, of the test article. As a result, attempts at dimensionality reduction and feature extraction based on raw schlieren images will not provide easily interpret-able results for all cases. In order to create a framework of data that is easily assessed for each angle of attack utilized, the frames of each video case taken were angled such that the nozzle in each frame was aligned with the horizontal center-line of the image. This allowed for a consistent nozzle location in video frames across the entire dataset.

To overcome the challenges of the cutoff angle of the schlieren data taken, the majority of analyses are conducted using the image gradient magnitude. An example of visualization challenges involving raw schlieren data is shown in Figure 3.9, with corresponding improved highlighting of flow features using the image gradient magnitude. The shock is more easily

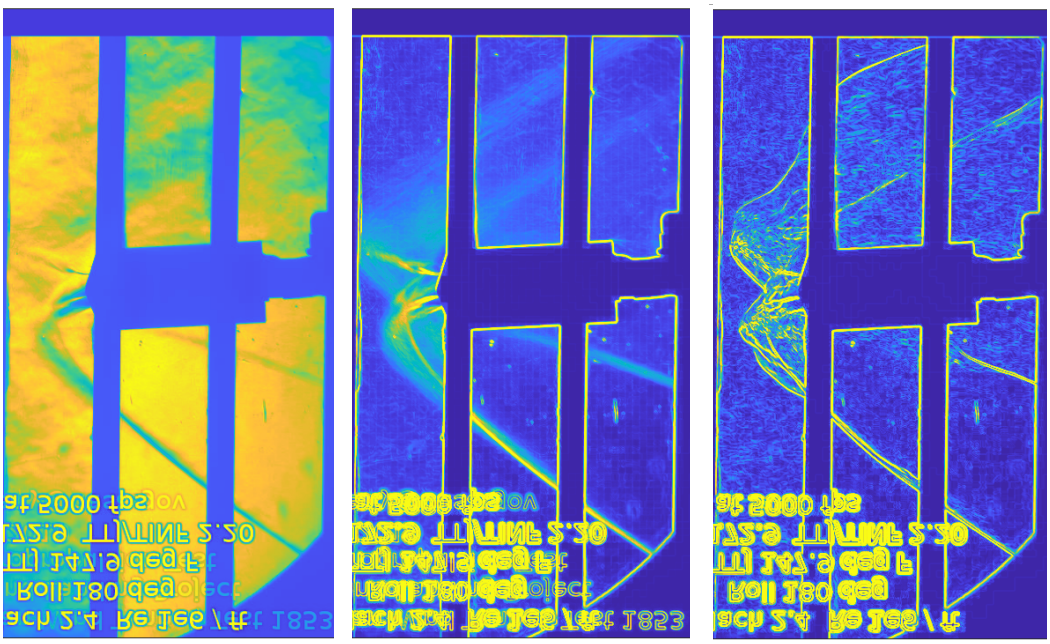

Figure 3.9: Example of feature extraction from SRP data from LaRC at Mach 2, tri-nozzle at 4° angle of attack from Berry[10]. From left to right: mean schlieren field, mean field of gradient magnitude, instantaneous gradient magnitude field.

identifiable throughout the run in the gradient mean image, resulting in a clearer look at shock dynamics throughout each test case.

Shock instability can be categorized by amplitude and frequency of shock oscillations. Focus in this study was on the instability amplitudes primarily, defining a new metric to enable comparisons between the highly varied conditions through the publicly available NASA SRP datasets [10]. Video sequences were extracted and categorized from larger video databases. The amplitude of instability of a given SRP configuration is based on a thresholded standard deviation image for each case. Figure 3.10 (a) shows a standard deviation image for Run 306, an unsteady quad-nozzle run at α = 0 and C_T = 3 showing shock oscillation with penetration. The white and yellow pixels represent the areas of high shock motion, while the darker regions are background of the image or areas of lower variability. The first step

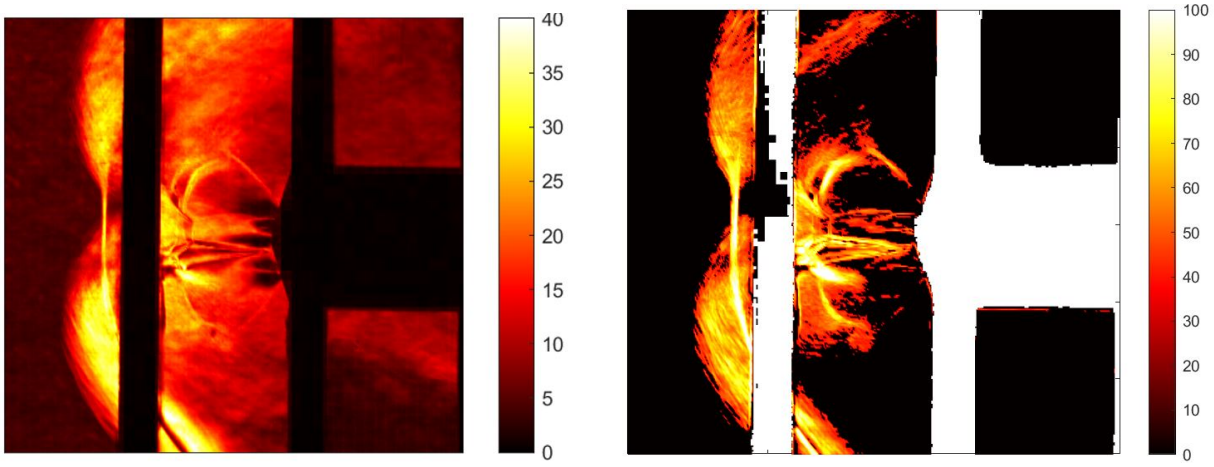

Figure 3.10: (a) Raw standard deviation image of unsteady, tri-nozzle case. (b)Masked standard deviation image of unsteady, tri-nozzle case.

in isolating the high-motion areas of each image was to create a mask for the nozzle and bars in each image. In Figure 3.10 (b), the white sections show the masked bars and nozzle. The background and low-motion sections of the image were then masked, similarly to the method used in the transition dataset described in Section 3.1.3, using a threshold pixel value. These regions are shown in black in Figure 3.10 (b). The instability amplitude is the ratio of remaining colored pixels to the total pixel count of the image. Note that different cases can be compared using this metric only when examining the same field of view in the reference frame of the test article, such that differences in measurement region and angle of attack do not produce biases.

Chapter 4

ONSET OF INSTABILITY FOR VARYING GAS TYPE AND NOZZLE FOREBODY

4.1 Transition to Instability

To investigate the conditions at transition to instability, two gas combinations, three forebody diameters, and two freestream Mach numbers were explored. Past SRP work by various groups typically used matched gas combinations and quite high D_b/D_e. The current study used both a Carbon Dioxide freestream with a Helium jet and a Nitrogen freestream with a Nitrogen jet gas with forebody diameters of 1/8-inch, 1/4-inch, and 3/8-inch. The corresponding jet pressure and coefficient of thrust for each case, along with the symbols used in the following figures, are given in Table 4.1. Transition cases are denoted by closed symbols while their corresponding steady cases are depicted using open symbols. The point at which this transition occurs was targeted by testing each gas combination and forebody size at varying pressures, lowering the jet pressure until the steady pressure threshold was crossed. For this reason, the steady cases shown in Table4.1 represent the closest-pressure steady case to the transition. The conditions which govern the appearance of instability are compared using the following flow parameters: pressure ratios, coefficient of thrust, forebody size, engine scaling parameter (ESP), and mass flux ratio. The transition to unsteadiness was not found for the Carbon Dioxide-Helium, 1/8 inch nozzle configuration. Data points were taken at a P_e/P_{02} of 0.2, 0.3, 0.4, and 0.5 for the Carbon Dioxide-Helium 1/8 inch nozzle case, each of which produced a steady shock.

Symbol	Retro-Freestream	Condition				Instability Type
●	$He - CO_2$	D_b = 0.25	M_j = 2	P_e/P_{02} = 0.8	C_T = 0.84	Shock Oscillation
▶	$He - CO_2$	D_b = 0.375	M_j = 2	P_e/P_{02} = 0.84	C_T = 0.608	Shock Oscillation
♦	$He - CO_2$	D_b = 0.125	M_j = 3	P_e/P_{02} = 0.28	C_T = 3.97	Shock Oscillation
★	$He - CO_2$	D_b = 0.125	M_j = 3	P_e/P_{02} = 0.28	C_T = 4.05	Shock Oscillation
■	$N - N$	D_b = 0.125	M_j = 2	P_e/P_{02} = 0.18	C_T = 1.03	Intermittent Shock Oscillation
●	$N - N$	D_b = 0.25	M_j = 2	P_e/P_{02} = 0.67	C_T = 0.5017	Intermittent Shock Oscillation
▶	$N - N$	D_b = 0.375	M_j = 2	P_e/P_{02} = 0.35	C_T = 0.39	Shock Oscillation
□	$He - CO_2$	D_b = 0.125	M_j = 2	P_e/P_{02} = 0.19	C_T = 1.29	Steady
○	$He - CO_2$	D_b = 0.25	M_j = 2	P_e/P_{02} = 1.03	C_T = 0.779	Steady
▷	$He - CO_2$	D_b = 0.375	M_j = 2	P_e/P_{02} = 0.61	C_T = 1.04	Steady
◇	$He - CO_2$	D_b = 0.125	M_j = 3	P_e/P_{02} = 0.4	C_T = 5.67	Steady
☆	$He - CO_2$	D_b = 0.125	M_j = 3	P_e/P_{02} = 0.28	C_T = 5.94	Steady
□	$N - N$	D_b = 0.125	M_j = 2	P_e/P_{02} = 100	C_T = 1.61	Steady
○	$N - N$	D_b = 0.25	M_j = 2	P_e/P_{02} = 0.81	C_T = 0.517	Steady
▷	$N - N$	D_b = 0.375	M_j = 2	P_e/P_{02} = 0.38	C_T = 0.55	Steady

Table 4.1: Legend of Test Parameters

All unstable cases in this set of data exhibited shock oscillation as their mode of instability. The Carbon Dioxide-Helium Mach 3 cases, Nitrogen-Nitrogen 3/8 inch nozzle case, and Carbon Dioxide-Helium 1/4 inch nozzle case each displayed a constant mode of shock oscillation throughout their runs. Both the Nitrogen-Nitrogen 1/4 inch nozzle and 1/8 inch nozzle cases showed a more intermittent unsteadiness, where a portion of the run was oscillating and a portion of the run was steady. For these cases, only frames that exhibited shock instability were used for the mean and RMS images and the majority of the upcoming figures. For the shock standoff plot, Figure 4.8, the steady and oscillating portions of the runs were split into two separate videos, and were treated as separate modes of each case. These cases are considered bi-modal, with one mode of instability being shock oscillation and the other being a steady shock. The Carbon Dioxide-Helium 3/8 inch nozzle case exhibited shock oscillation throughout the entirety of its run, however, it demonstrated two modes of

(a) Mean Image

(b) RMS Image

Figure 4.1: Ni-Ni 18-inch Nozzle Unstable Case

this oscillation. For the first portion of the run, the shock oscillated around a point on the far left side of the frame. After about 100 frames, this first oscillation mode dropped to a location with a shorter shock standoff distance for the remainder of the run. This case is treated as bi-modal, with each portion of the video being split in order to evaluate their shock standoff distance, and later, its Proper Orthogonal Decomposition analysis.

The mean and RMS images for each transition case are shown in Figures B.1 through 4.7. The RMS images show areas of high motion, depicted by white or light yellow pixels: the motion shown in the RMS images increases with increasing nozzle diameter. The shock standoff distance also increases with increasing forebody diameter. The Carbon Dioxide-Helium unsteady mean images are less clear than that of the Nitrogen-Nitrogen unsteady cases due to the larger amplitude of motion throughout each oscillation. The Nitrogen-Nitrogen 18 case exhibits a period of flapping motion as well as oscillation throughout its run, whereas the rest of the cases exhibit full shock oscillation for the duration of their unsteadiness. Shock standoff distance is far higher for Carbon Dioxide-Helium cases than those of the Nitrogen-Nitrogen cases, showing a gas dependency, as seen in Jennis[12]. The

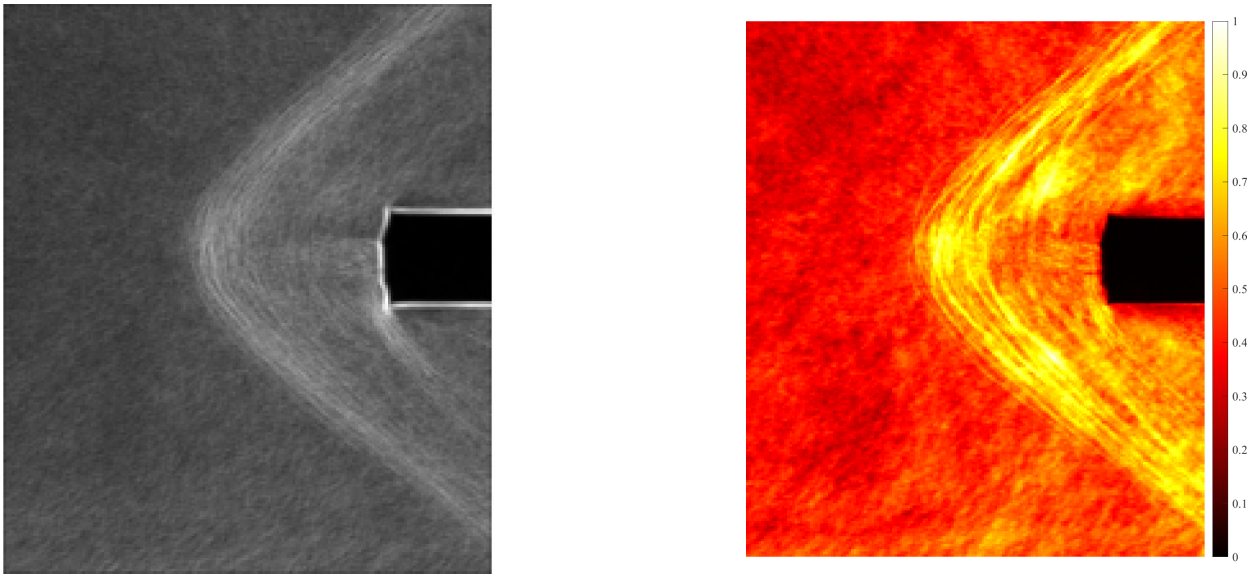

(a) Mean Image

(b) RMS Image

Figure 4.2: Ni-Ni 14-inch Nozzle Unstable Case

mean and RMS images of the nearest steady cases taken with each nozzle type and gas combination are given in Appendix A.

The mean shock standoff distance normalized by the nozzle diameter of both the unsteady case and the lowest C_T steady case of each nozzle type are shown with the general trend line found by Jennis[12] in Figure 4.8. The error bars for this plot represent the maximum and minimum shock location throughout an oscillation. In the y-direction they represent the next-closest C_T-Mach ratio taken in the x-direction. The front of the shock in the Carbon Dioxide-Helium 3/8 inch nozzle case and the Mach 3 cases, depicted in Figures 4.5 through 4.7, are out of the frame of the image. For the shock standoff distance calculations in each of these cases, the far left side of the image was considered to be the front of the shock. These shock standoff distance calculations are, therefore, more conservative than the actual mean shock standoff distance. The distance from the left side of the frame to the minimum shock location was used for both of the errorbars in the y-direction for these three cases. The

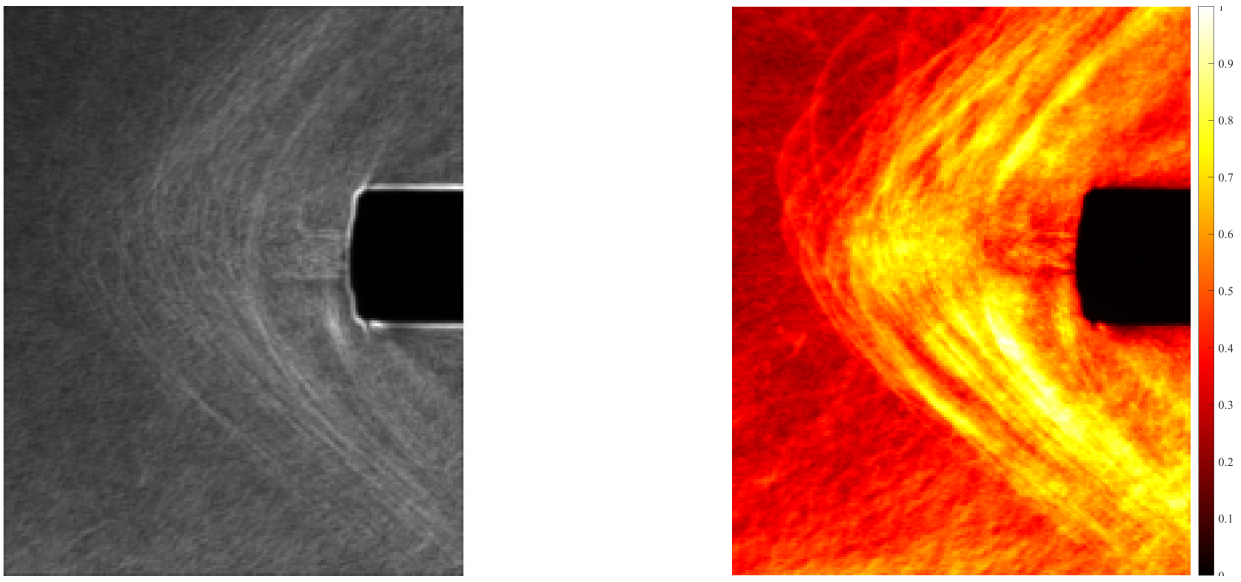

(a) Mean Image (b) RMS Image

Figure 4.3: Ni-Ni 38-inch Nozzle Unstable Case

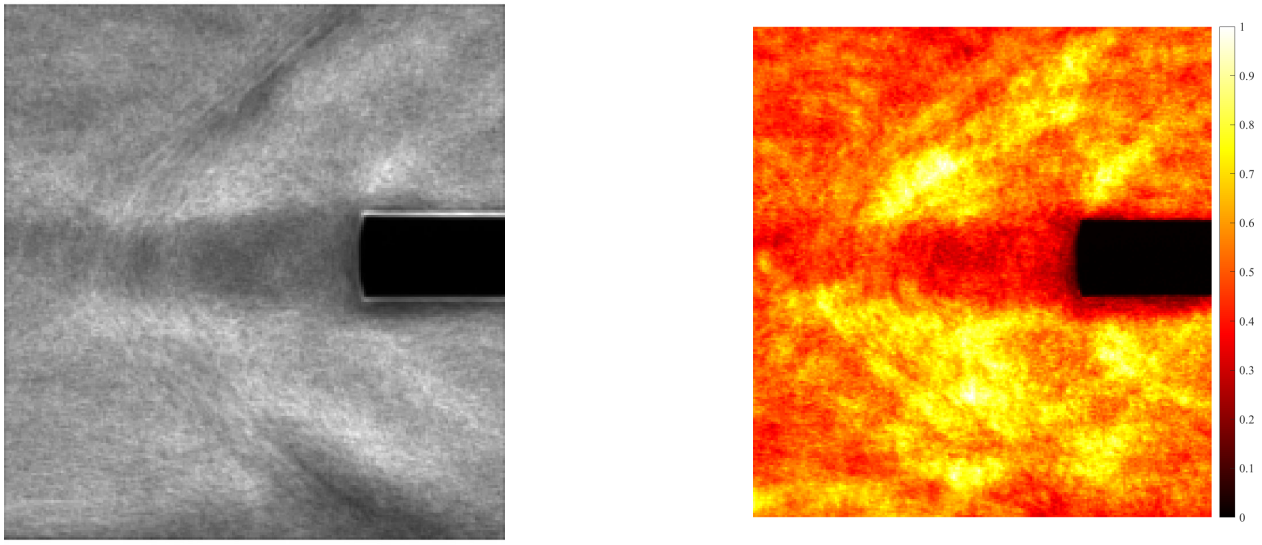

(a) Mean Image (b) RMS Image

Figure 4.4: CO2-He 14-inch Nozzle Unstable Case

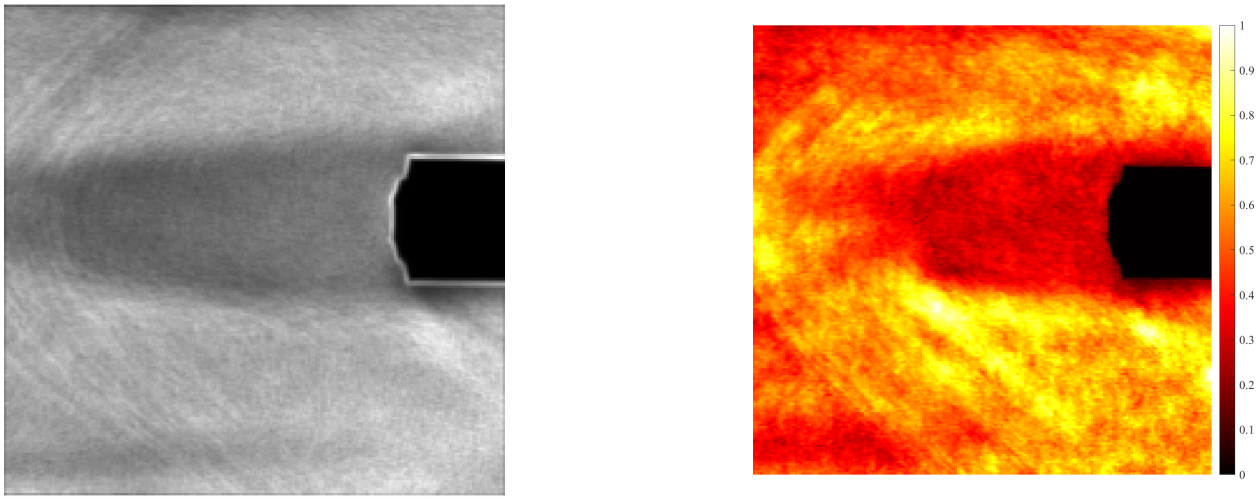

(a) Mean Image (b) RMS Image

Figure 4.5: CO2-He 38-inch Nozzle Unstable Case

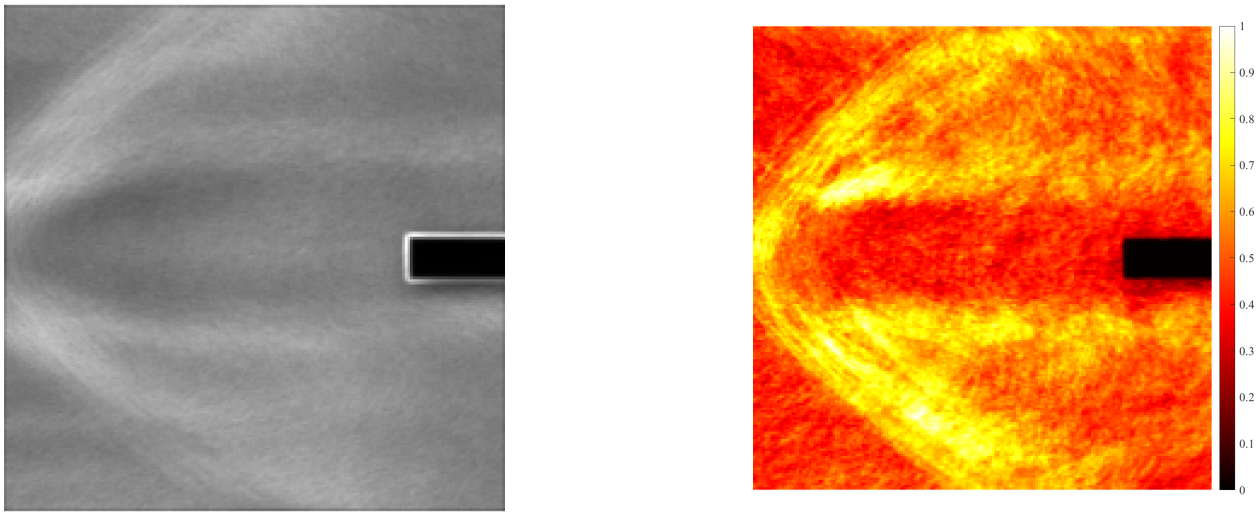

(a) Mean Image (b) RMS Image

Figure 4.6: CO2-He 38-inch Nozzle Unstable Case, Mach 3

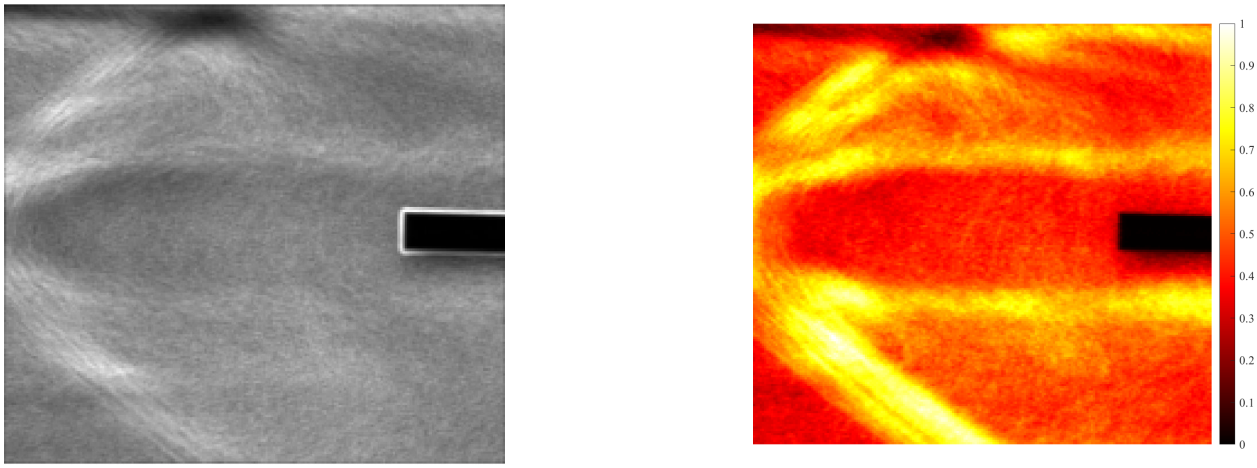

(a) Mean Image (b) RMS Image

Figure 4.7: CO2-He 38-inch Nozzle Unstable Case, Mach 3 Heated

steady cases collapse well to Jennis'[11] trend line, whereas the transition cases have much higher shock standoff distances. The Carbon Dioxide-Helium cases, as seen in the mean images, have shock standoff distances greater than the corresponding Nitrogen-Nitrogen cases, particularly at Mach 3.

The unsteady cases are of the most interest, particularly the point at which the shock transitions from being the high shock steady regime to exhibiting unsteady characteristics. The pressure ratio was plotted against coefficient of thrust in Figure 4.9. The error bars for Figure 4.9 represent the distance to the pressure ratio or C_T of the next-closest steady case that was taken. The Carbon Dioxide-Helium cases where the transition point was found follow a similar trend to the Nitrogen-Nitrogen cases taken, with a slightly higher pressure ratio and C_T, at the onset of instability. The transition point of the 1/8 inch nozzle, Mach 3 cases occurred at significantly higher coefficient of thrust values, although the pressure ratio at which transition occurred was fairly similar to that of the Nitrogen-Nitrogen 1/8 inch

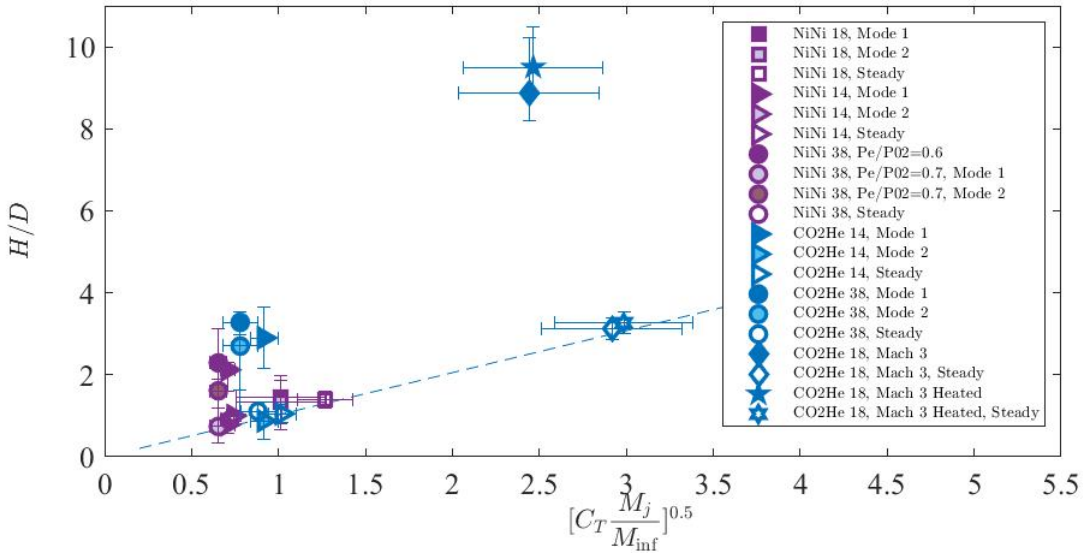

Figure 4.8: Shock standoff distance normalized by nozzle diameter for instability onset data (closed symbols) and steady data (open symbols). Trend line from Jennis[11].

nozzle case; again, no transition point was found for the Carbon Dioxide-Helium 1/8 inch nozzle case. As forebody area decreased, the transition pressure ratio also decreased, with the transition for the 1/8 inch Nitrogen-Nitrogen case occurring at a pressure ratio of less than 0.2.

Korzun & Cassel [6] concluded that the transition to an unsteady shock appeared to occur when P_e/P_{02} and where C_T exceeded unity. Their study included data from Jarvinen & Adams [4] and Berry [10], whose D_b/D_e ratios were 30 and 20, respectively. The A_b/A_e ratios in the data taken in the discussed dataset are all below 1. As seen in Figure 4.9, the transition point occurred at pressure ratio values lower than unity, at a ratio as low as 0.2. The conclusion that the transition to steadiness occurs at unity may only hold true for larger D_b/D_e values, as it seems to fall apart as forebody area decreases. This may be due to the use of the post-shock stagnation pressure as a proxy for the forebody base pressure. Deviations between the base pressure and this stagnation pressure would therefore lead to a different expansion condition than suggested from the P_e/P_{02} parameter alone. In contrast

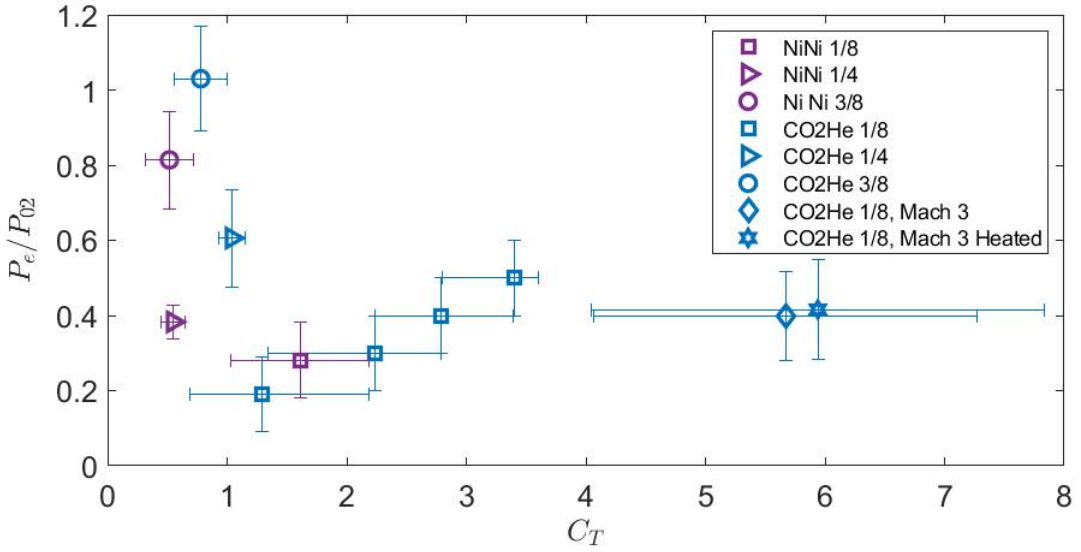

Figure 4.9: Pressure C_T plot for instability onset data and steady cases taken for the Carbon Dioxide-Helium 18-inch nozzle.

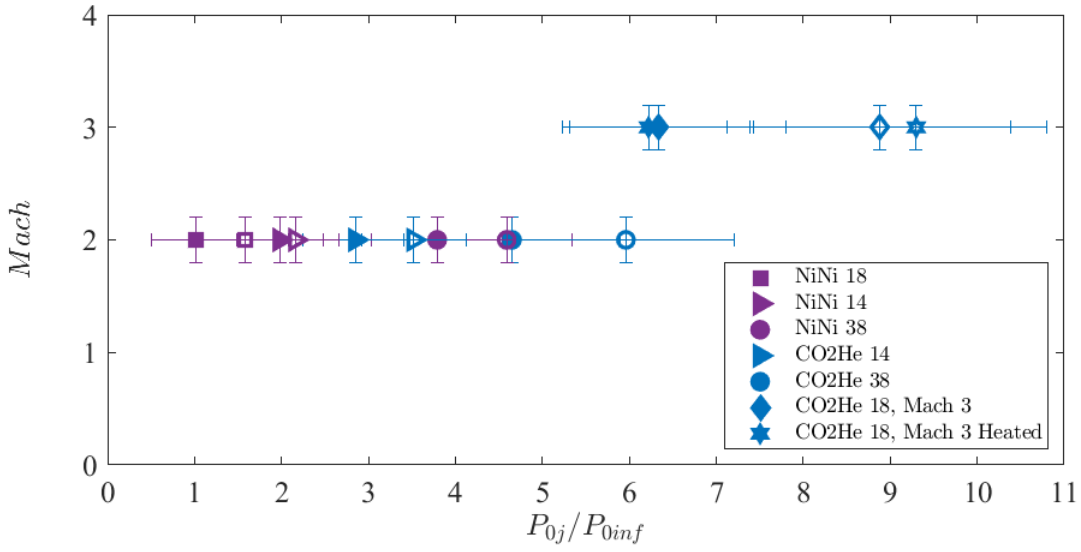

Figure 4.10: Total pressure ratio for each jet Mach number tested with unsteady cases (closed symbols) and steady data (open symbols).

to what Korzun & Cassel [6] concluded, Figure 4.9 shows that instability can be present for both C_T and P_e/P_{02} less than 1.

Romeo & Sterrett[15] found a clear transitional line between steady and unsteady shocks when looking at total pressure ratio against the freestream Mach number, as described in Figure 2.2. This plot was replicated with the transition dataset, shown in Figure 4.10. No clear transitional line can be seen for this dataset, therefore the finding in Romeo & Sterrett may not hold true for all conditions.

The ratio of jet and freestream total pressures was plotted against the ESP, as explored by Jarvinen & Adams[4]. The transition points shown in the Jarvinen & Adams plot in Figure 2.3 fall around the pressure ratio of about 7 for both of the Mach numbers and each of the three forebody sizes tested. Each of their cases' transition to unsteadiness occurred at roughly the same pressure ratio, independent of the ESP and affecting only C_T. The new UW dataset shows the transition for Mach 3 cases occurring just below a pressure ratio of 7, while all other transition data lies at varying lower pressure ratios. They saw that transition occurred at lower C_T for smaller nozzle forebody and higher C_T for larger forebody, of which the UW dataset is not in agreement.

Tan[21], Ho[5], and Yang[14] concluded that the transition to shock instability occurs at a total pressure ratio of 1. However, since Ho and Yang only took readings at total pressure ratios of 0.5, 1, and 5, what their data really showed was that the transition is somewhere between 0.5 and 5. The findings in Figure 4.11 support that conclusion. While the Nitrogen-Nitrogen 1/8 inch nozzle transition does in fact occur close to a total pressure ratio of 1, the other transition points, with the exception of the Mach 3 cases, occur between 1 and 4.65. The errorbars for Figure 4.11 represent the difference to each cases' corresponding steady case.

Mass flux ratio has been a common parameter to study in the field of supersonic retro-propulsion as of late. The transition points were plotted using P_e/P_{02} against mass flux ratio, as shown in Figure 4.12. While course, the data might be considered to collapse roughly onto a single curve under these coordinates. This is promising, however, further study is

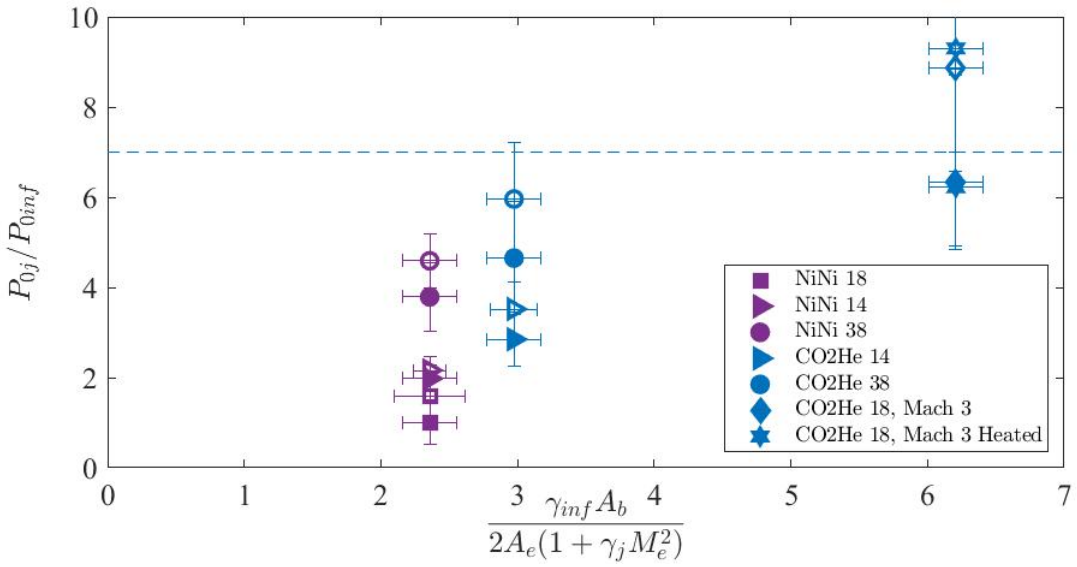

Figure 4.11: Engine scaling parameter for instability onset data with unsteady cases (closed symbols) and steady data (open symbols).

needed to determine if this generalizes to a broader set of conditions.

The amplitude of oscillation was found for both the steady and unsteady cases discussed previously and is shown in Figure 4.13. The errorbars for the amplitue values in this figure represent 5% of the total amount of pixels in the image frame. The amplitude is expressed as a percent of pixels in the RMS image for a case, as described in Section 3.1.3. As expected, the larger forebody unsteady cases have a much higher amplitude of oscillation than their corresponding steady cases. The two unsteady 3/8 inch nozzle cases each contain over 30% higher amplitude than their corresponding steady cases. The oscillation amplitude seems to increase by about 10% as the gas is heated. There is also a gas dependency on oscillation amplitude, with Carbon Dioxide-Helium cases experiencing a higher amplitude than their corresponding Nitrogen-Nitrogen cases, where comparable data is available.

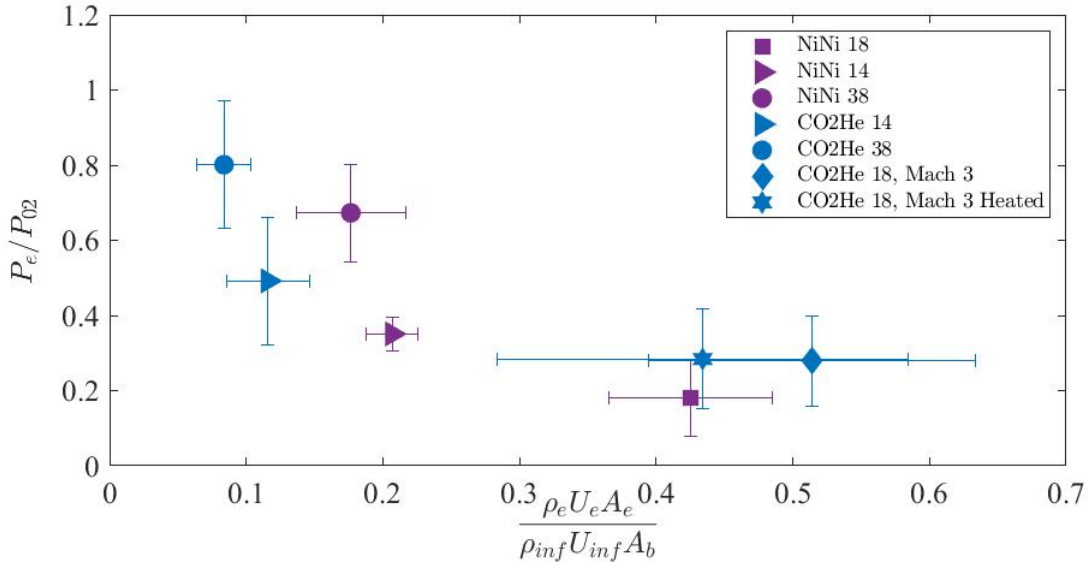

Figure 4.12: Plot of mass flux ratio for instability onset data.

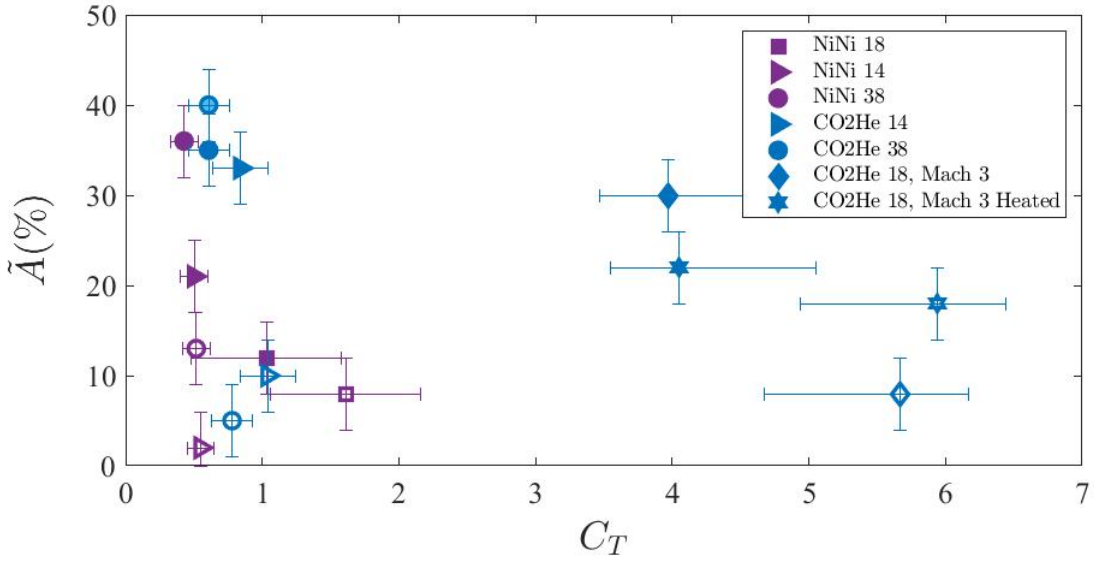

Figure 4.13: Shock amplitude comparison of cases with varying forebody with unsteady cases (closed symbols) and steady data (open symbols).

4.2 Discussion

For both gas combinations tested, the shock instability seen is almost exclusively the oscillation mode for small forebody, single nozzle, zero angle of attack cases. Many of these unsteady cases exhibited a bimodality of shock unsteadiness, whether in the form of partialy oscillating and partially steady or displaying shock oscillation at differing shock standoff distances. Instability for the small forebodies tested can be intermittent, as seen in the smaller forebody Nitrogen-Nitrogen cases, and the amplitude of shock oscillation is gas dependent. Mean shock standoff distance is also gas dependent, as well as Mach dependent, and is larger for unstable cases. In contradiction to previous conclusions by Korzun & Cassel, Jarvinen & Adams, and Ho and Yang, instability can be present for $C_T < 1$ and $P_e/P_{02} < 1$, but transition varies depending on Mach number, gas type, and nozzle forebody size. As engine scaling parameter was increased, the total pressure ratio at which transition occurred increased as well. Scaling data by the mass flux ratio caused data to roughly collapse onto a single curve.

Chapter 5

INFLUENCE OF ANGLE OF ATTACK ON INSTABILITY

The NASA dataset was classified in three categories of instability: steady, oscillating, and oscillating with penetration. While past work done with this dataset has classified the unsteadiness as primarily oscillating with some mention of penetration occurring intermittently, there seem to be valuable trends that can be observed by categorizing cases as purely oscillating or oscillating with shock penetration present. Cases classified as steady are defined as cases in which the shock does not exhibit movement throughout the run; changes in primary bow shock placement are not discernible between video frames. These cases are still considered stable despite some motion of the triple point and shear layers being apparent behind the bow shock. Several frames of the stable center nozzle case at Mach 2, C_T=2, α = 0 are shown in Figure 5.1.

Oscillating cases are those which exhibit either a small-scale rippling of the shock (flapping) or large-scale shock oscillation throughout the run. These typically coincide. Figure 5.2 shows frames from the oscillating quad nozzle case at Mach 2, α=0, C_T= 1, where the shock motion follows the historical oscillation definition. In contrast, a case exhibiting shock penetration throughout its run is shown in Figure 5.3; this is a quad nozzle case at Mach 2, α = 0, C_T=3. The jet flow is penetrating the shock to some extent in both of the two nozzle locations that can be seen throughout the entirety of the video frames shown. Due to the complicated flow patterns caused in multi-nozzle jets, we feel that many cases cannot be as clearly classified and do not fall completely into the traditional category of "long penetration mode." There are also cases that show varying amounts of shock penetration with some intermittency. Frames from two such cases are shown in Figures 5.4 and 5.5. Since these cases exhibit flow patterns of both oscillation and penetration, we find it challenging to define

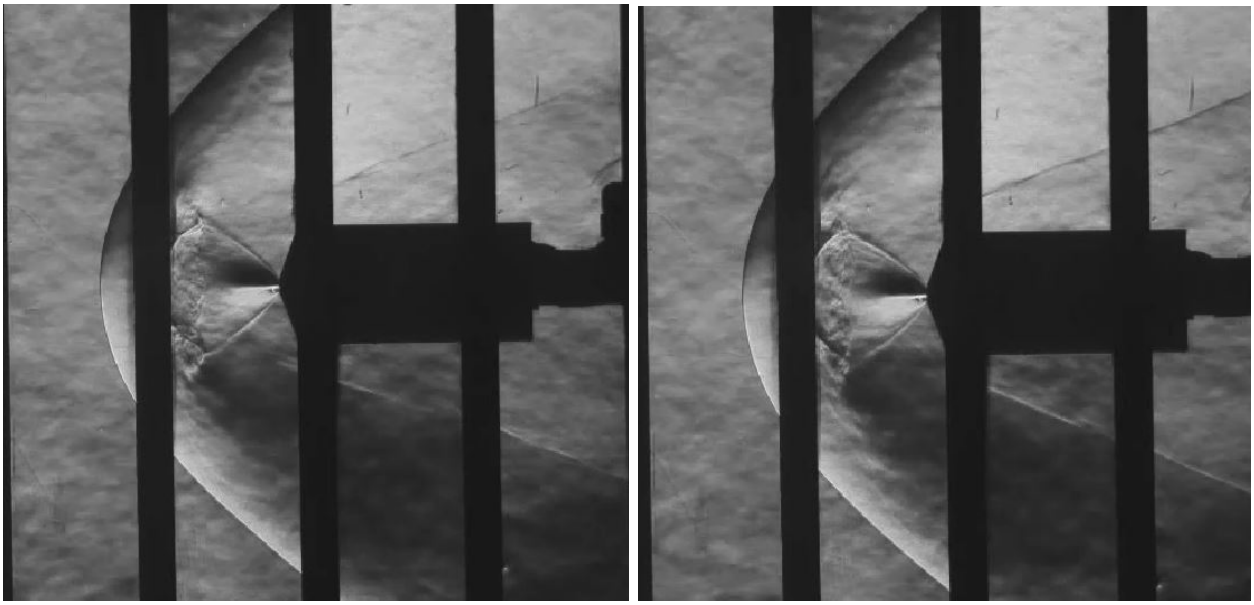

Figure 5.1: Frames from a Stable Run, Center nozzle, Mach 2, C_t=1, α=0°.

them as either of these types. As a result in this thesis they are classified as "oscillation exhibiting penetration" for our purposes.

A legend for the NASA dataset figures is given in Table 5.1. Cases are colored by their instability type and the symbols represent the freestream Mach number used.

5.1 NASA Center Nozzle

Within each nozzle type, the Mach number, angle of attack, and coefficient of thrust were varied. These parameters were plotted to get a better idea of whether consistent thresholds can be identified which describe when the onset of instability will occur. Each nozzle configuration is plotted separately in order to understand the difference in dynamics between them, with the center nozzle configuration providing the clearest instability trends across the dataset. Varying jet pressure to freestream pressure ratio at 0° angle of attack was plotted against both coefficient of thrust and mass flow ratio, shown in Figure 5.6. Figure 5.6a shows a linear trend for each center nozzle Mach number, with Mach 4 having the sharpest slope

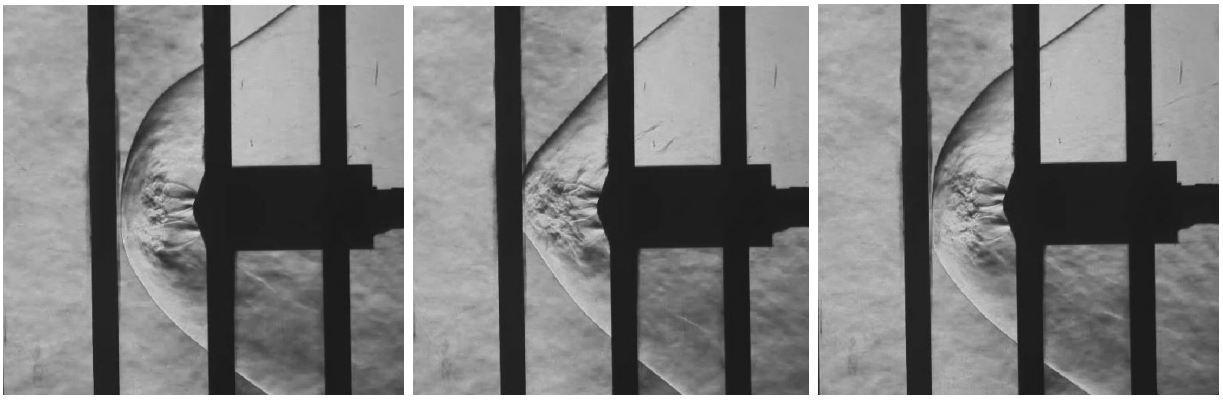

Figure 5.2: Frames from an Oscillating Run, Quad Nozzle, Mach 2, C_t=1, α=0°.

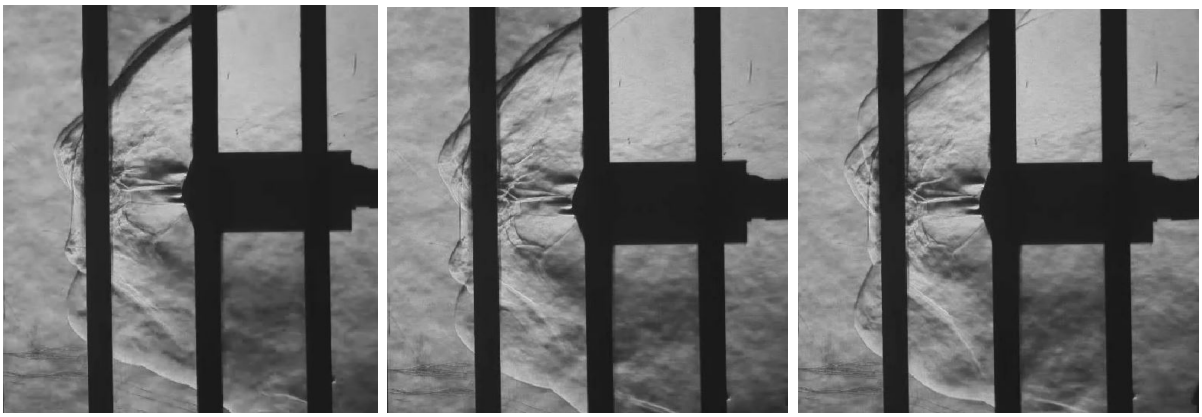

Figure 5.3: Frames from a Penetrating Case, Quad Nozzle, Mach 2, C_t=3, α=0°.

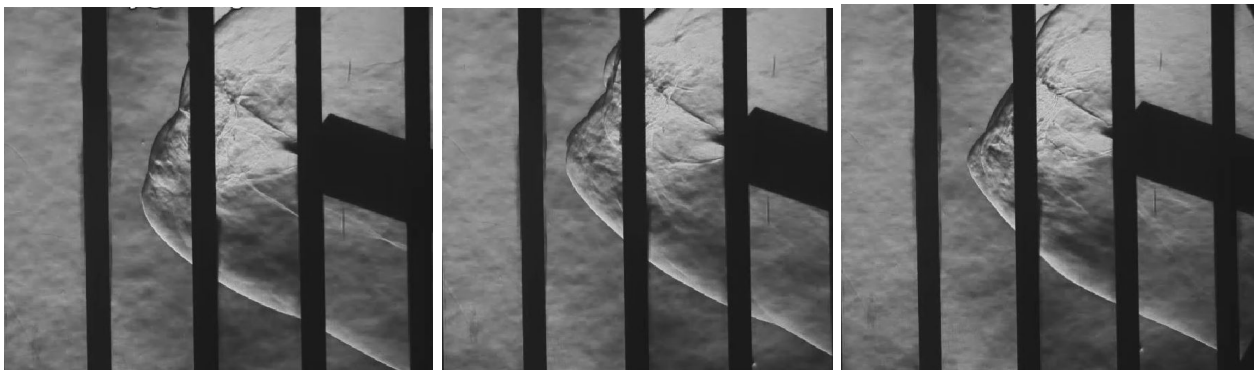

Figure 5.4: Frames from an Oscillating Case with Penetration: Tri Nozzle, Mach 3, C_T=3, α=20°.

Figure 5.5: Frames from an Oscillating Case with Penetration: Quad Nozzle, Mach 3, C_T=1, α=0°.

Symbol	Mach Number	Stability Type
●	M_∞ = 2	Steady
■	M_∞ = 3	Steady
★	M_∞ = 4	Steady
●	M_∞ = 2	Oscillating
■	M_∞ = 3	Oscillating
★	M_∞ = 4	Oscillating
●	M_∞ = 2	Oscillation exhibiting penetration
■	M_∞ = 3	Oscillation exhibiting penetration
★	M_∞ = 4	Oscillation exhibiting penetration

Table 5.1: NASA Plot Legend

and Mach 2 having the most gradual, whereas Figure 5.6b shows Mach 2 having the highest slope and Mach 4 having the most gradual. The lowest pressure ratio case, at Mach 4 and C_T 0.2, exhibits shock oscillation, while all other center nozzle cases at 0° angle of attack remain steady.

Figure 5.7 shows all of the center nozzle cases as a function of thrust coefficient and angle of attack. Steadiness is observed for higher values of C_T and lower angle of attack while oscillation is found at higher angle of attack, lower C_T. The center nozzle configuration did not display any cases exhibiting shock penetration within the test parameter space. The two cases at a coefficient of thrust of 2 with an angle of attack of 8 have differing stability. The Mach 2 case is oscillating, while the Mach 3 case is steady, showing that there is some Mach dependence along with the angle of attack dependence, with the higher freestream Mach case exhibiting a less stable shock. Figure 5.11 shows the coefficient of thrust plotted against Mach number for the center nozzle cases at 0-degrees angle of attack and 4-degrees angle of attack. Both plots show that at Mach 4, oscillating cases begin to form. Based on

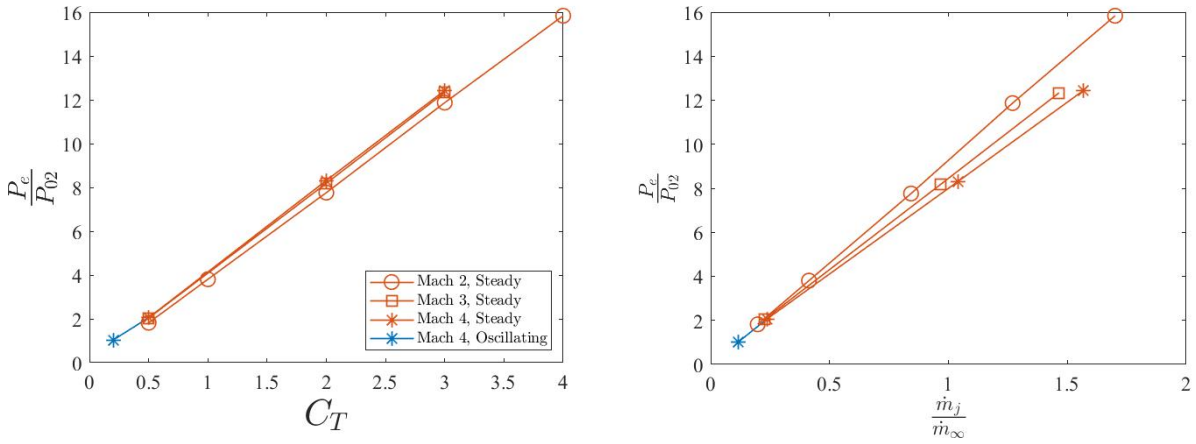

Figure 5.6: Pressure plots for center nozzle cases in the NASA dataset.

the 0-degree angle of attack case, it seems oscillation occurs at lower coefficients of thrust. The Mach 4, coefficient of thrust 0.5 cases are comparable between the two plots, showing that higher angle of attack seems to cause unsteadiness. In Figure 5.8, the pressure ratio was plotted against angle of attack to explore the influence of jet expansion conditions on SRP instabilities. There is less delineation in this plot between the steady and oscillating cases across the center nozzle dataset, suggesting that pressure ratio correlates less clearly with the onset of instability than thrust coefficient. The $P_{te}/P_{t\infty}$ is plotted against the engine scaling parameter for the center nozzle in Figure 5.13. The transition pressure between steady and oscillating cases here occurs between a pressure ratio of 0.19 and 0.37, with the Mach 4 lowest total pressure case exhibiting unsteadiness. This transition total pressure ratio is close to the transition total pressure of the Nitrogen-Nitrogen transition point in Figure 4.11.

For the center nozzle configuration dataset, low coefficient of thrust, higher angle of attack, and higher freestream Mach number cases tend to exhibit shock oscillation. There were no cases where shock penetration could be observed with a center nozzle. Pressure ratio and engine scaling parameter provide less observable trends. Due to the range of freestream Mach numbers used in this dataset, pressure and coefficient of thrust are closely linked

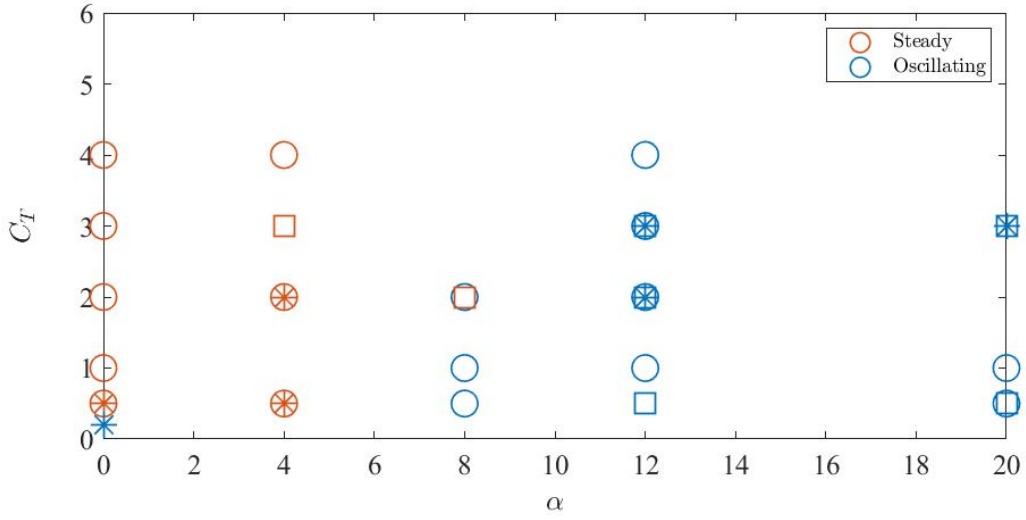

Figure 5.7: Center nozzle coefficient of thrust plot indicating the transition between steady and oscillating shocks.

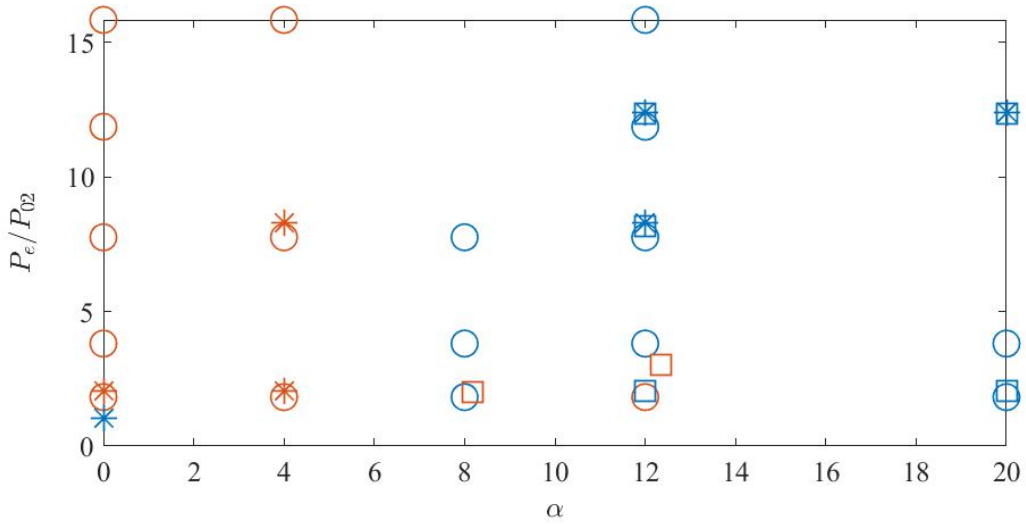

Figure 5.8: Center nozzle pressure ratio plot indicating the transition between steady and oscillating shocks.

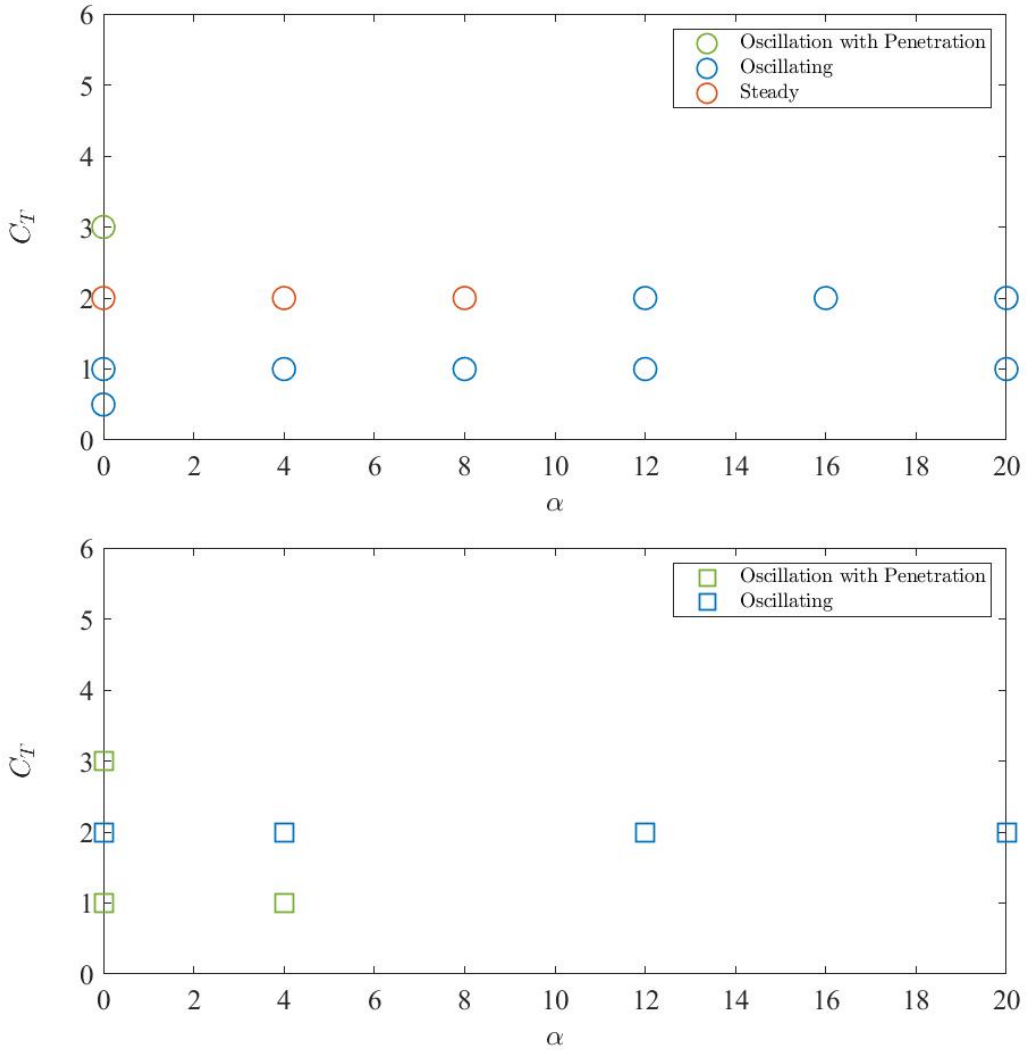

Figure 5.9: Quad nozzle coefficient of thrust and angle of attack at freestream (a)Mach 2. (b)Mach 3.

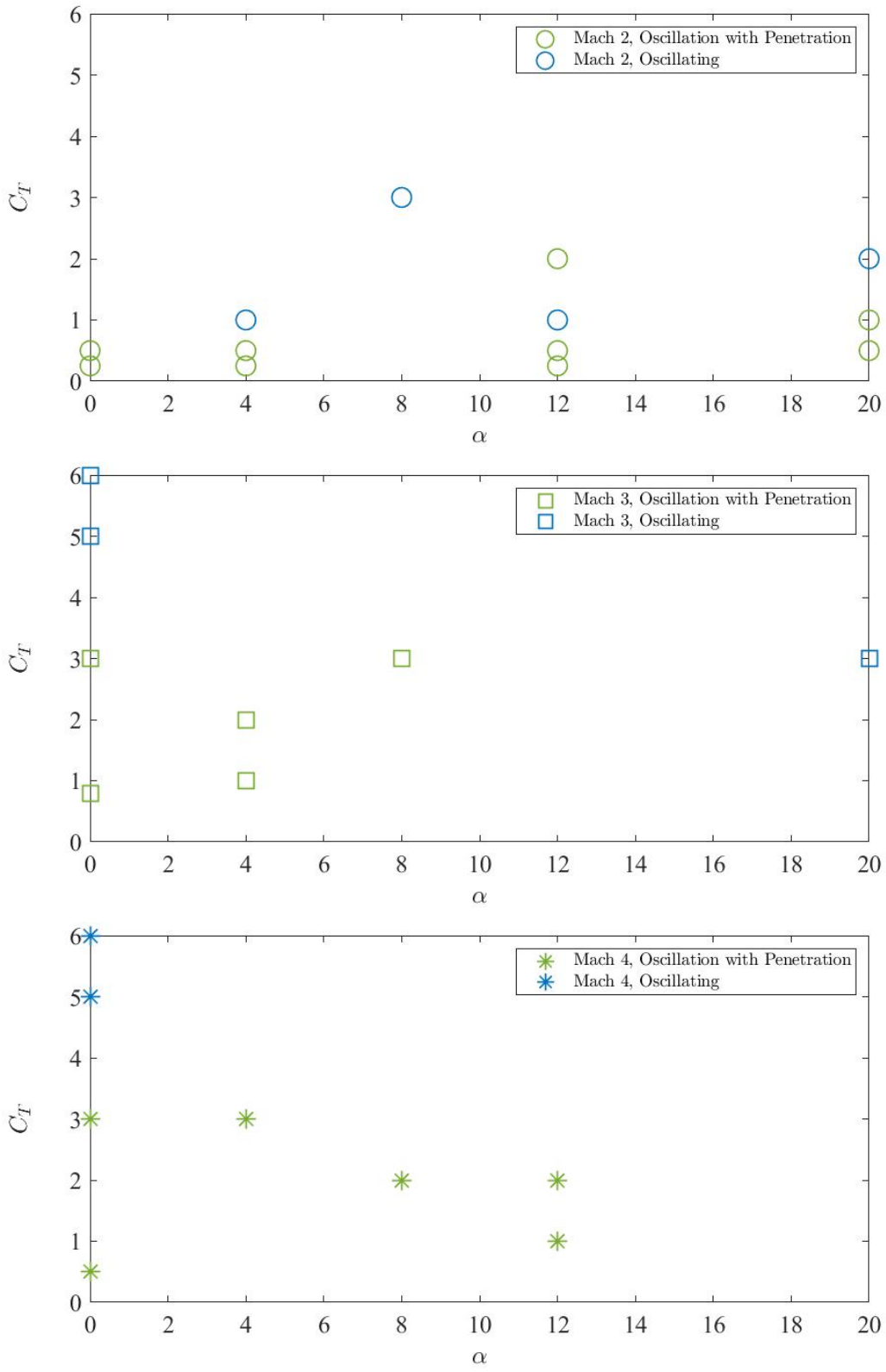

Figure 5.10: Tri nozzle cases at freestream Mach values of (a)Mach 2. (b)Mach 3. (c) Mach 4.

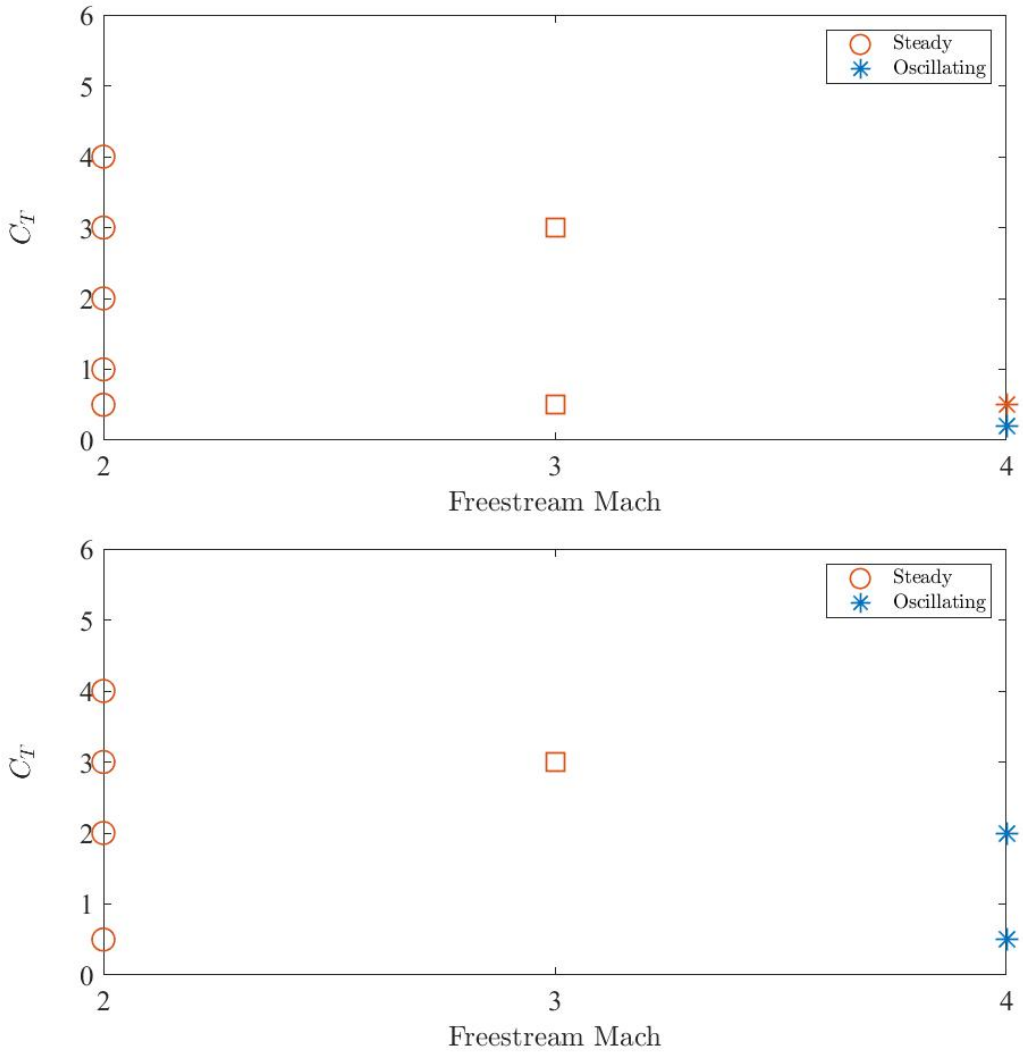

Figure 5.11: Center nozzle coefficient of thrust and freestream Mach at (a)α=0°. (b)α=4°.

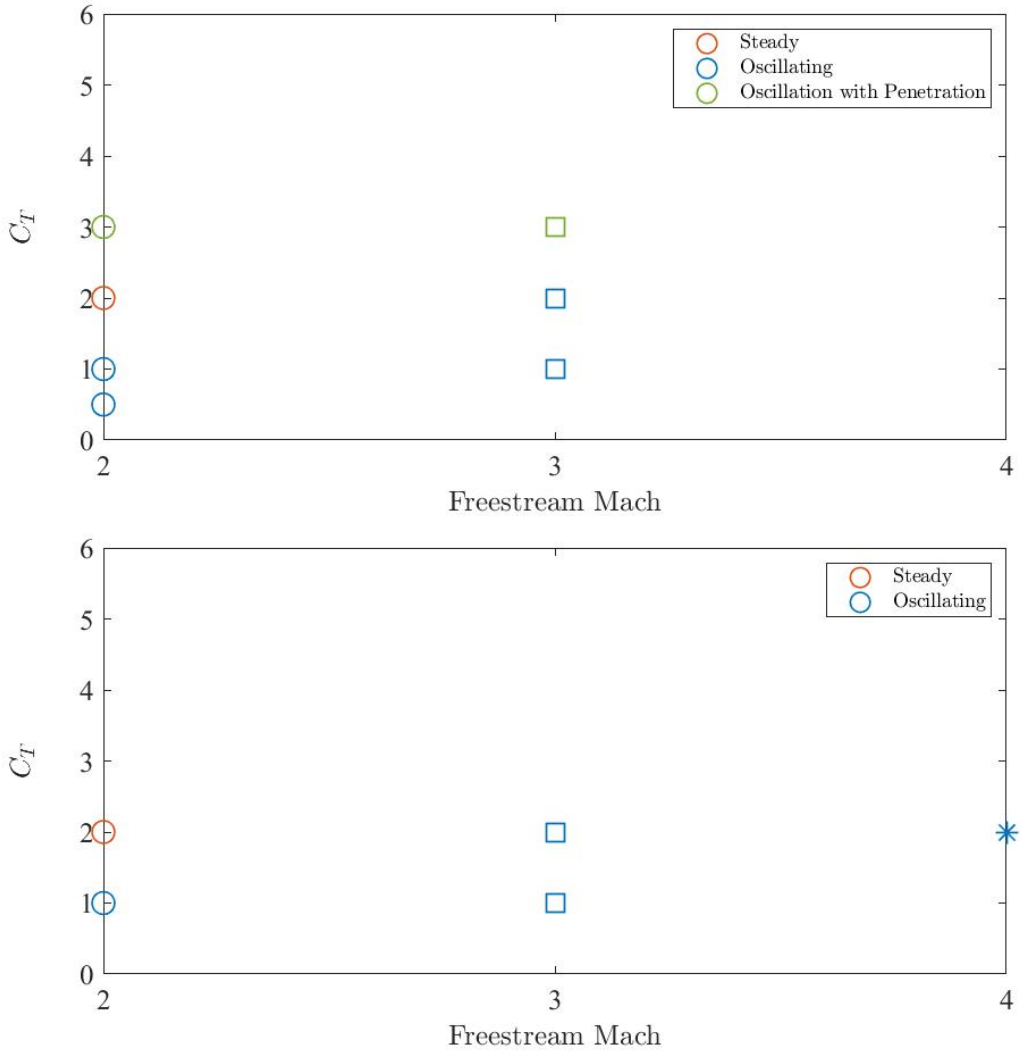

Figure 5.12: Quad nozzle coefficient of thrust and freestream Mach number at (a)α=0° (b)α=4°.

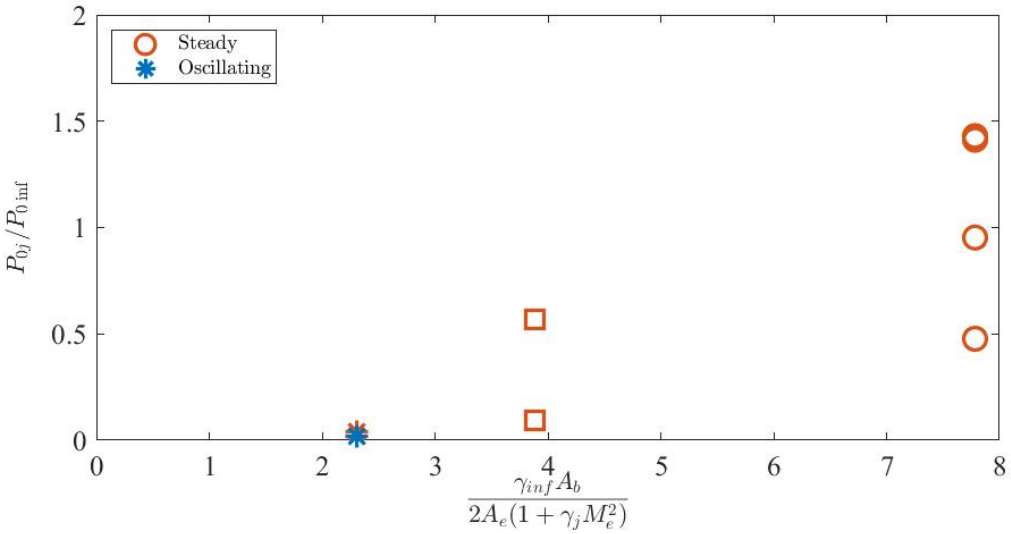

Figure 5.13: Center, Mach 2 nozzle engine scaling parameter.

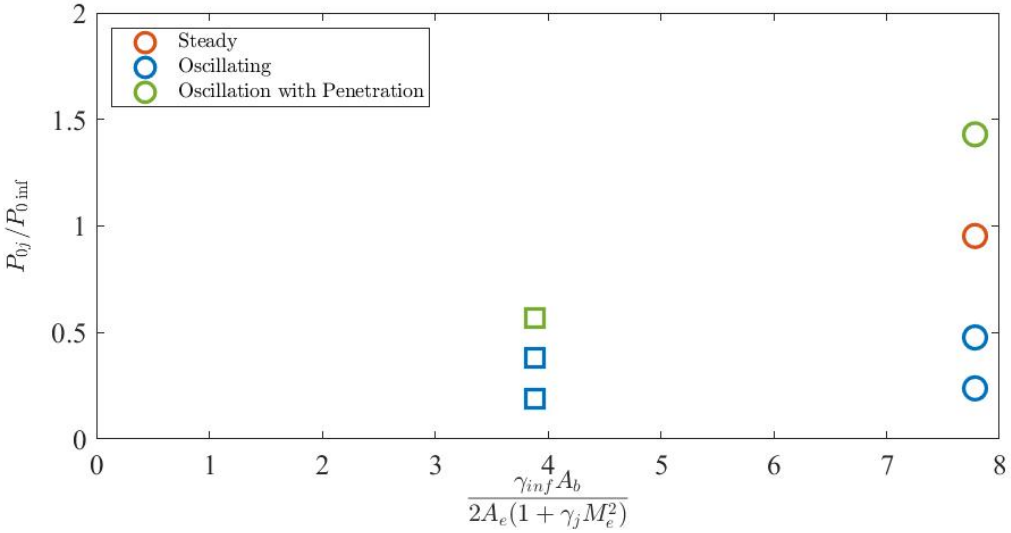

Figure 5.14: Quad nozzle engine scaling parameter.

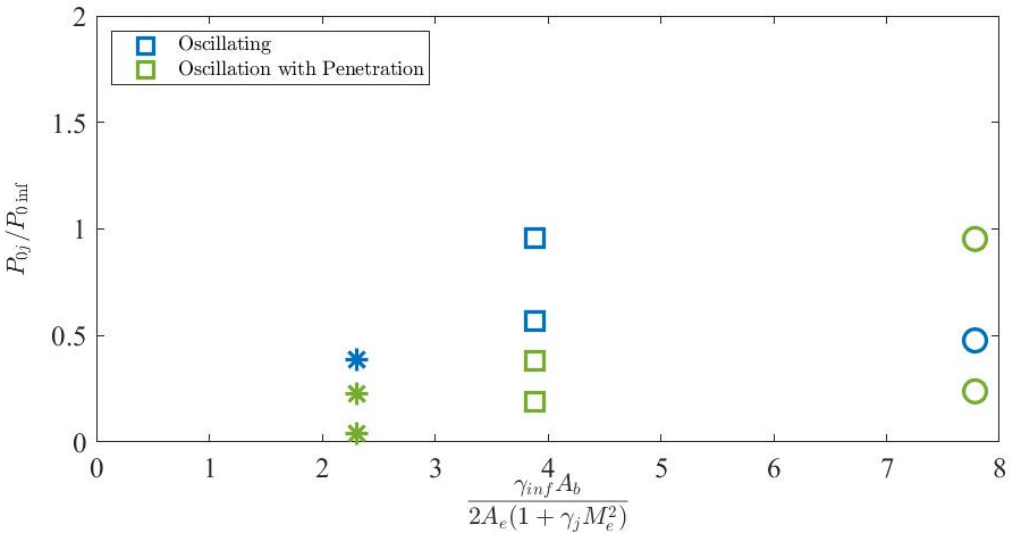

Figure 5.15: Tri nozzle engine scaling parameter.

parameters.

5.2 NASA multi-nozzle configurations

The multi-nozzle configurations do not provide as clear unsteadiness trends due to the more complex interactions between the jets. The multi-nozzle cases did, however, contain cases exhibiting shock oscillation with penetration and therefore provided observable trends between the two types of unsteadiness classified in this study. There were no steady cases for the tri-nozzle dataset and therefore the quad nozzle is the only configuration which exhibited all three categories of unsteadiness. Figure 5.9 shows the coefficient of thrust plotted against angle of attack for the quad nozzle cases at freestream Mach 2 and Mach 3; not enough data were available to observe trends for Mach 4. Figure 5.9a contains all three instability types, showing that at the highest C_T and 0 angle of attack, some shock penetration occurs. When angle of attack is high and C_T is low, the shock tends to purely oscillate. The cases between the penetrating and oscillating cases are steady. Overall, the Mach 3 plot shows the same trend at coefficients of thrust 2 and 3. However, the runs at a coefficient of thrust of 1 exhibit

penetration, which suggests more C_T dependence than angle of attack dependence here.

The coefficient of thrust is plotted against Mach number in Figure 5.12 for angles of attack 0° and 4°. Figure 5.12a shows penetrating cases at the highest coefficient of thrust value of 3, with oscillation at all other C_T values. There is one steady case in between the clusters of penetrating and oscillating cases. This reinforces the trend seen in Figure 5.9a where the steady cases occur between the two unsteady types. Figure 5.12b exhibits this same general trend for $\alpha = 4^\circ$, although there are no penetrating cases at this angle of attack to fully verify that shock penetration will always occur at high C_T values.

Quad nozzle engine scaling parameter is shown against the jet exit pressure to freestream pressure ratio in Figure 5.14, where oscillation occurs up to a $P_{te}/P_{t\infty} = 0.48$. Above this, there are two penetrating cases occurring at the highest pressure ratios of each Mach subset. There seems to be a region in between shock oscillation and shock oscillation exhibiting penetration where the shock becomes steady, as described in several previous quad nozzle figures. The trend between steady and oscillating shock cases corresponds to the center nozzle ESP plot in Figure 5.13 with a steady shock occurring at higher $P_{te}/P_{t\infty}$ with oscillation forming as the pressure ratio is lowered.

Each Mach number is plotted separately for the tri-nozzle case coefficient of thrust against angle of attack plots for ease of visualization. In Figure 5.10a, all cases are penetrating at C_T=0.5 and below. However, at C_T=1 and C_T=2, there are both penetrating and oscillating cases. There seems to be an increase in the occurrence of shock penetration as coefficient of thrust decreases. The freestream Mach 3 and 4 charts do show a grouping between cases with penetration and purely oscillating cases, again with shock penetration occurring as C_T decreases. The higher Mach numbers seem to show a more clear grouping, but this could be due to less availability of data at lower C_T and higher angle of attack for Mach 3 and 4. In Figure 5.10b, oscillating cases occur at high C_T, low α and there is a transition to penetrating cases as C_T lowers and angle of attack increases. There is one case, however, where oscillation occurs at a high angle of attack, C_T= 3. This case does not show clear penetration of the shock, but there may be a little, blocked by the tunnel window reinforcement bar. At Mach

4, oscillating cases occur at low angle of attack, C_T 5 and 6, while higher angle of attack and lower C_T cases exhibit oscillation with penetration. This is in agreement with the other tri nozzle trends.

When engine scaling parameter was plotted against $P_{te}/P_{t\infty}$ for the tri-nozzle configuration, an opposite trend to what is shown in the corresponding quad nozzle plot, Figures 5.13 and 5.14. For the quad nozzle, as pressure ratio increased, cases tended towards shock oscillation with penetration from a purely oscillating shock. For the tri-nozzle, oscillating cases exhibiting shock penetration occur at lower pressure ratio, higher ESP. At higher pressure ratios within each Mach grouping, the shock purely oscillates.

The normalized shock standoff distance for the 0° angle of attack dataset is shown in Figure 5.16 for all three of the nozzle configurations. These values were found utilizing the same method as was used for the transition data discussed previously. The mean image was used to calculate the shock standoff distance, with error bars corresponding to the maximum and minimum shock location in the run. The steady shock cases had higher shock standoff distances than the penetrating cases that matched C_T. Oscillating cases had relatively low shock standoff distances, remaining around 1. As expected, as C_T increased, so did normalized shock standoff. The trend line found by Jennis[12] is depicted by the blue line, of which the cases mainly fall below. Cases from each of the three nozzle configurations are shown in Figure 5.16, although shock standoff for each of the three nozzle configurations are shown separately in Appendix A. The tri-nozzle cases tended to have the lowest shock standoff distance as compared to quad- and center-nozzle cases.

5.3 Shock Amplitude

Trends were seen visually in the NASA dataset videos as shock amplitude and frequency changed with varying parameters: amplitude and frequency of the shock motion varied inversely with one another consistently. Amplitude was quantified using the method described in section 3.2.3. Figure 5.17, which utilizes a different marker color and symbol notation than the previous plots, shows the variability of this new instability amplitude metric across

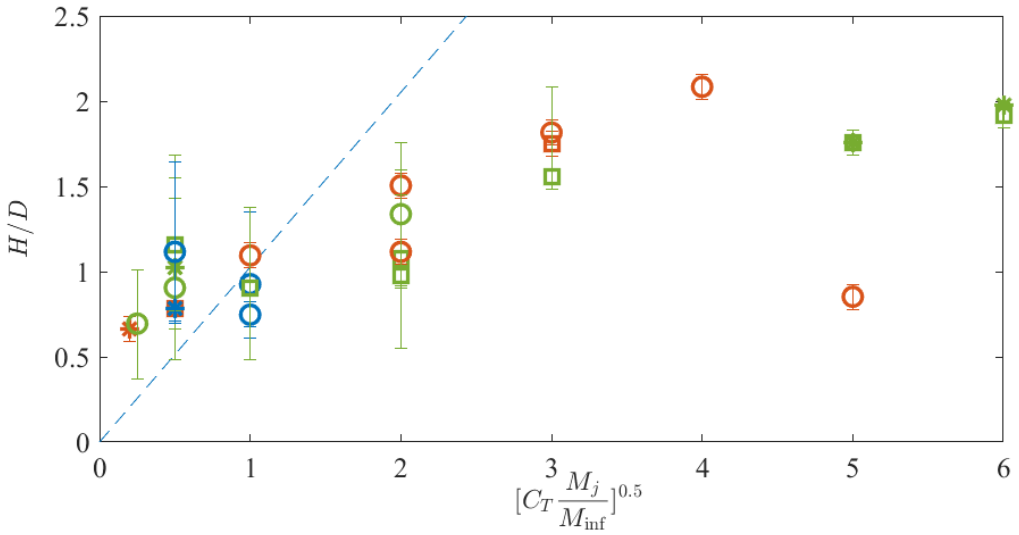

Figure 5.16: Shock standoff distance of NASA dataset, all three nozzle configurations, trend line from Jennis[12].

the entire 0° angle of attack portion of the NASA dataset. Error bars are used to represent uncertainties resulting from variable placement of the reinforcement bars relative to regions of instability. This error was conservatively estimated to be 5% of the total pixels in a frame. While this figure depicts instability amplitude as a function of coefficient of thrust, it should be noted that angle of attack, Mach number and geometry are also varying. This dataset suggests that the single center nozzle configuration has the lowest instability amplitude, on average. Conversely, the tri-nozzle configuration has the largest instability magnitudes in most cases, with the quad nozzle configuration somewhere in between. A few outlier quad-nozzle cases, however, have the largest overall instability magnitudes.

Figure 5.21 breaks down these amplitude trends further as a function of angle of attack, thrust coefficient, and geometry. For the central nozzle case, as angle of attack increases, instability amplitude typically increases as well. Most interestingly, for a number of thrust coefficients, a maximum amplitude is observed around 12° before decrease for further increases in angle of attack. The highest angle of attack condition was not sampled for all

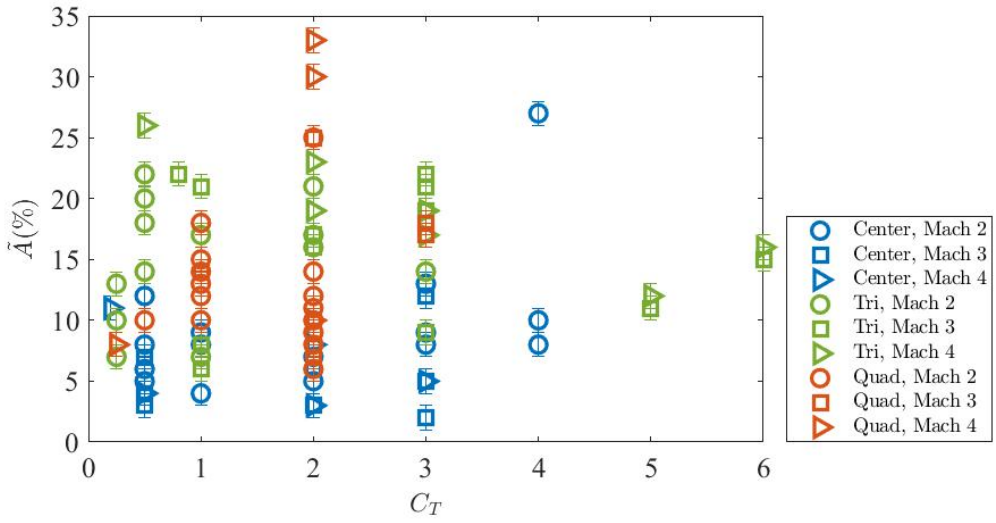

Figure 5.17: Shock amplitude comparison by nozzle type for all $0^{\circ}\alpha$ cases.

thrust conditions and so it is not possible determine if this is a general result at this time, however it is suggestive of interesting underlying dynamics. In the more complex nozzle configurations, as seen in Figure 5.21 (b) and (c), this trend is not apparent. The instability amplitude for these configurations is more constant for a given thrust condition with the exception of the C_T = 2, quad-nozzle cases, which increased in amplitude with increasing angle of attack.

5.4 Discussion

These plots show clear groupings between the types of unsteadiness, and, where data is available, a trend from oscillating cases exhibiting penetration to steady and on to pure oscillation when looking at coefficient of thrust against angle of attack and freestream Mach number. The C_T vs Mach plots show that as freestream mach increases, cases tend to exhibit unsteadiness. As C_T increases, cases become more steady. And, finally, there are angle of attack and nozzle configuration dependencies as well. With higher angle of attack and lower C_T, generally oscillation occurs, while as C_T increases and Mach number decreases, generally

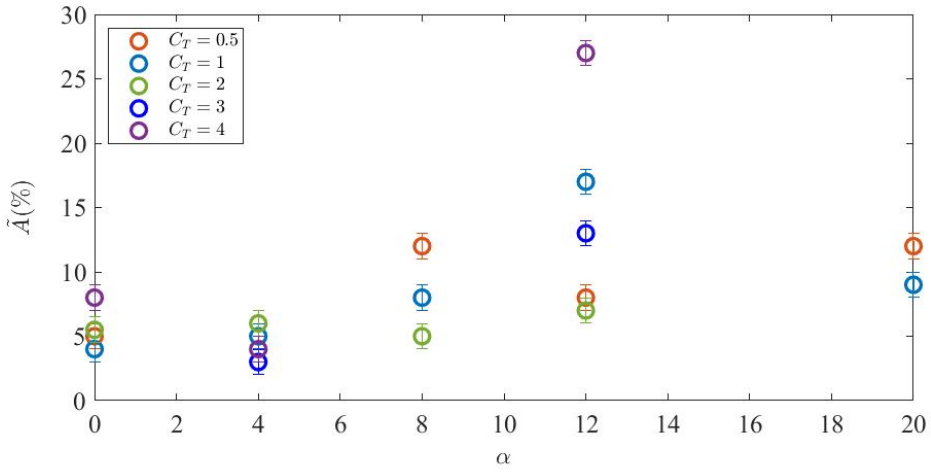

Figure 5.18: Mach 2 Center Nozzle

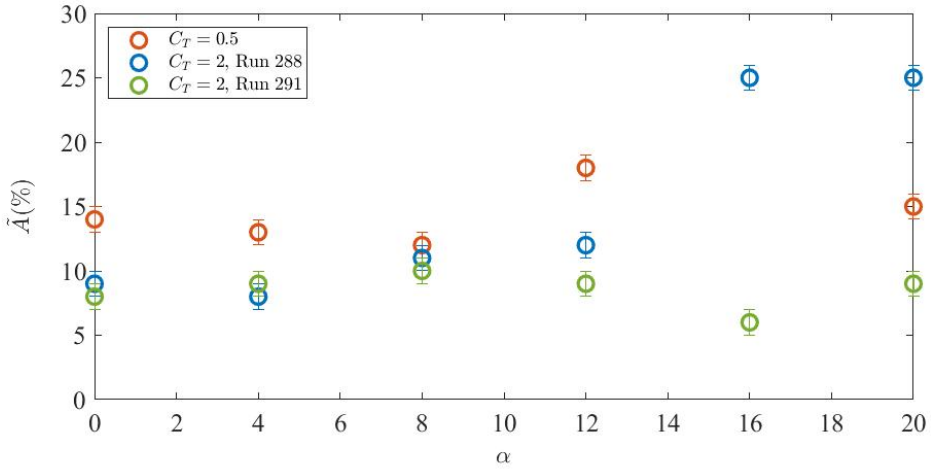

Figure 5.19: Mach 2 Tri Nozzle

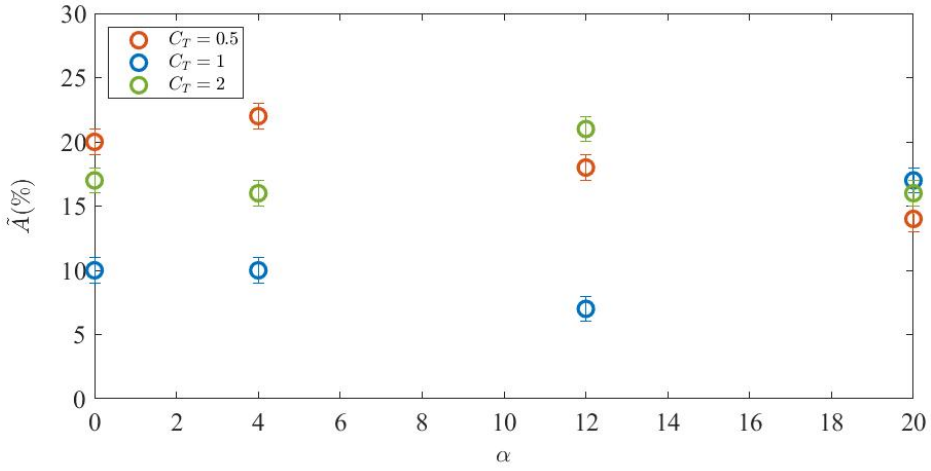

Figure 5.20: Mach 2 Quad Nozzle

shock penetration can be seen along with the shock oscillation.

The center and quad nozzle cases, at lower pressure ratio, typically exhibit shock oscillation, while at higher pressure ratios, they display shock oscillation with penetration. For the tri-nozzle cases, the opposite tends to occur, with shock penetration occurring at lower pressure ratios than the purely oscillating. For center and quad nozzle cases, with higher Mach and lower C_T, cases tend towards steadiness. However, the tri nozzle cases, as Mach increases and C_T lowers, tend to shift from being steady to exhibiting oscillation with shock penetration. Generally, center nozzle cases at all C_T values exhibit lower amplitude of shock motion than either set of multi-nozzle cases, while tri-nozzle cases tend to have the highest amplitude of shock motion, coinciding with the fact that tri-nozzle cases tend to show more shock penetration than the other nozzle configurations as oscillating cases that exhibit shock penetration tend to have the highest quantitative amplitude of motion.

Chapter 6

INSTABILITY CHARACTERIZATION UTILIZING PROPER ORTHOGONAL DECOMPOSITION

6.1 Instability Topologies from POD

Partial Orthogonal Decomposition (POD) creates an optimal basis for reconstructing the flow, with modes weighted by their contribution to changes in image intensity. This approach provides valuable insights for reduced order modelling and low-order representations of high-dimensional dynamical systems such as SRP flowfields.

The method of snapshots [22] decomposes a series of image variations (deviation from the mean image) as,

$$I(x) = \sum_{n=1}^{N} = a_n \Phi(x)$$

where N is the number of images in the dataset. The spatial modes are calculated as through the eigenvalue problem,

$$\int_{\mathcal{D}} R\left(x, x'\right) \Phi\left(x'\right) dx' = \lambda \Phi(x)$$

where R is the two-point spatial correlation matrix. Modes are ordered by their eigenvalues, λ, which indicates their importance to overall dynamics. The activation coefficients, a_n, indicate the contribution of a mode to an individual image and are calculated by projecting the modal basis onto the original images. POD has a number of very interesting properties that increase its utility for the analysis of dynamical systems. It extracts modes that are optimal from an energetic point of view. The modes must also respect the boundary conditions of the entire dataset.

A series of POD modes for a Mach 2, Tri nozzle SRP configuration at an angle of attack of 4° is shown in Fig. 6.1. In this case, POD has been applied to the image gradient

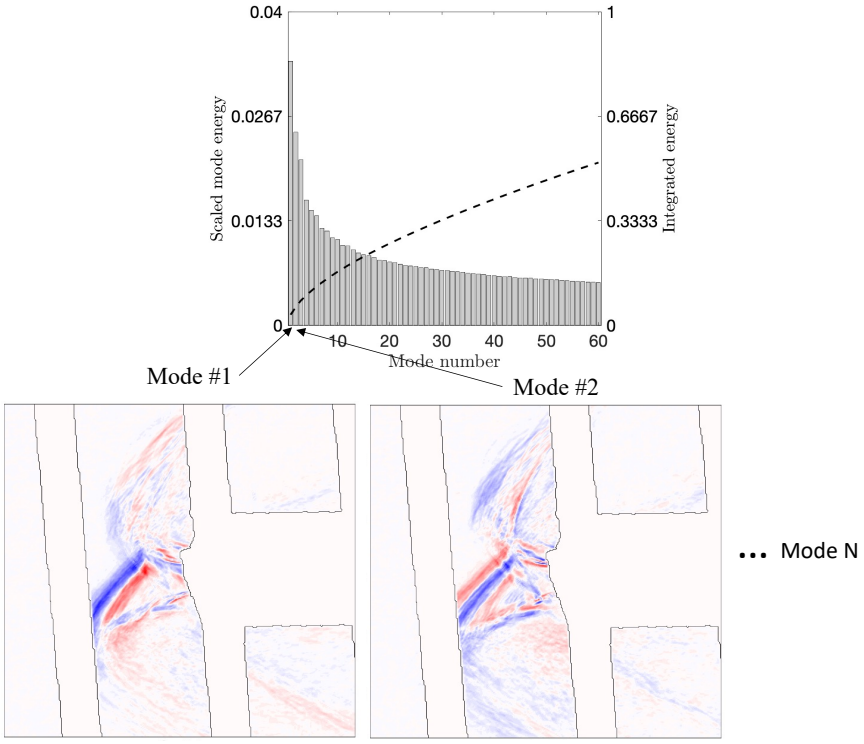

Figure 6.1: POD analysis tri-nozzle, Mach 2, 4° angle of attack case from Fig. 3.9. Top: Distribution of modal energy. Bottom: First and second POD modes with similar structures and half wavelength phase shift. Data from Berry[10].

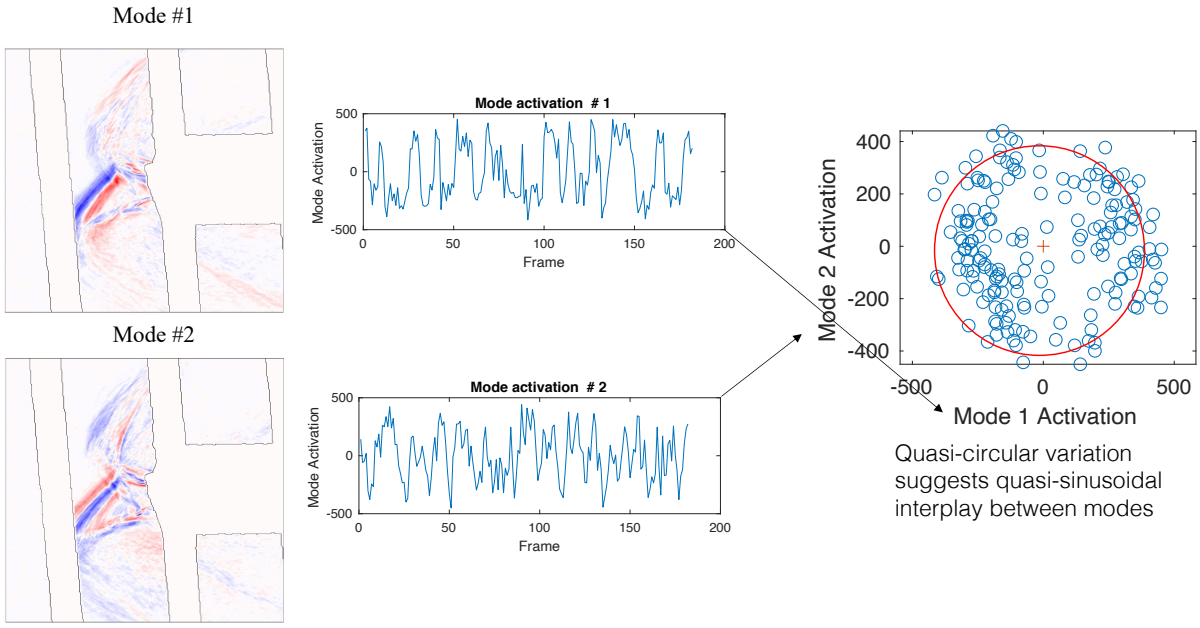

Figure 6.2: POD analysis tri-nozzle configuration from Fig. 3.9. Right: Covariance of first and second modal activation, with red circle indicating quasi-sinusoidal covariance with 90° phase offset. Data from Berry[10].

magnitude fields, allowing coherent shock motions to be identified without interpretation challenges introduced by the angle of the schlieren cutoff relative to the test article, as discussed in Section 3.2.3. As shown in the energy diagram in Figure 6.1, modal energy decreases quickly from the first few modes, suggesting that much of large scale structure can be described by the variation of only the first several high-energy modes. To examine this further, we focus on the first two modes, which exhibit significant intensity on one side of the interaction associated with a large bow-shock oscillation. Note that, while these modes look very similar, the colored bands of high intensity are shifted relative to each other by half of their wavelength. This suggests that these are a modal pair that describe a back and forth motion. The activity of each of these modes can be correlated with one another to further explore their pairing. Figure 6.2 examines the co-variation of the activation coefficients for this pair of modes. Interestingly, these modal activations approximately lie in a donut-like pattern, suggesting a quasi-sinusoidal relation between them.

6.2 POD of NASA Data

Proper Orthogonal Decomposition was implemented on the NASA dataset in order to evaluate the different forms of dynamic instability and their sensitivities. The two forms of instability seen throughout the cases are shock oscillation and oscillation exhibiting shock penetration. Figure 6.3 shows a video frame of an oscillating case, along with the first three POD modes of the case and its modal energy distribution. Each of the first three modes describe the oscillation of the shock throughout the video by describing the motion of the shock bands. The red and blue bands represent patterns of the shock oscillation, which occur throughout the entire run. The oscillation of this case is relatively low amplitude, with shock bands being generally thin. This case is a Mach 4 center nozzle case with an oscillation amplitude of 11%. Figure 6.4 shows a video frame of a Mach 4 tri-nozzle oscillating case that exhibits shock penetration with an oscillation amplitude of 26%, along with the first three modes and the modal energy distribution. From these modes, the two "peaks" of the shock penetration are easily visible. Where the red and blue energy bands are thicker, as on

the bottom halves of the two shock sections, there is more unstable motion throughout the run. Each mode can be thought of as indicating regions of correlated and anti-correlated changes in image intensity. They will often also operate in pairs (with a half wavelength spatial offset) to describe shock motions. The following POD analysis on the NASA dataset will give a look at how the POD modes of cases describe shock instability as different parameters, such as angle of attack, coefficient of thrust, and Mach number, are changed. The remaining cases in this section will show the first mode and modal energy distribution of the case, however, the first few modes of each case are given in Appendix C. The mean and RMS images of each case described in this section are also shown in Appendix C.

The three nozzle configurations in this dataset are tri-, quad-, and center-nozzle configurations. Figures 6.5, 6.6, 6.7 show each nozzle configuration at Mach 2, C_T =2, and α =12. Each case is unsteady, with the center- and quad-nozzle cases exhibiting less unsteadiness. The shock bands of both of these cases are thin, with a small distance between each one. The tri-nozzle case, Figure 6.6, however, shows a high level of motion, with large, messy shock bands in portions of each mode. The first mode shows the best depiction of the shock penetration that occurs in this run, where the large blue shock band punches through where the shock typically occurs in this run. The difference in energy from the first mode to the following modes is far higher than the other cases discussed. Therefore, this first mode describes most of the shock motion throughout the rest run. As is generally seen in cases where the three nozzle configurations can be compared, the tri-nozzle configuration exhibits the highest amount of shock unsteadiness, with the center- and quad-nozzles exhibiting similar presentations of unsteadiness. Quad nozzle cases typically exhibit more unsteadiness than corresponding center nozzle cases.

As was seen in Section 5.3, as angle of attack increases, so does amplitude of shock unsteadiness up to 12° angle of attack for center nozzle cases. Higher than 12°, at 20°, the amplitude of unsteadiness decreases again. This can be seen through the POD analysis of Run 139, a center nozzle, Mach 2, C_T 1 case. The first three POD modes and the modal energy distribution for each angle of attack for this case are shown in Figures 6.8 to 6.12. The

(a) Video Frame

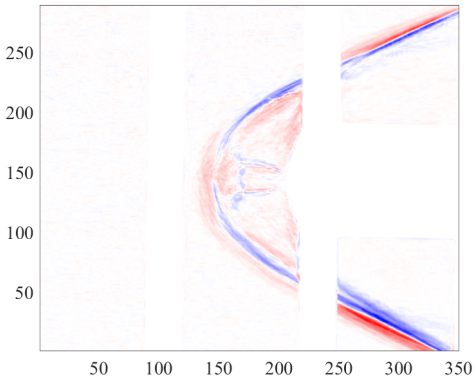

(b) Mode 1

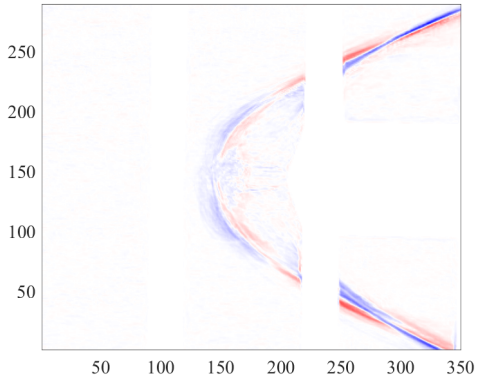

(c) Mode 2

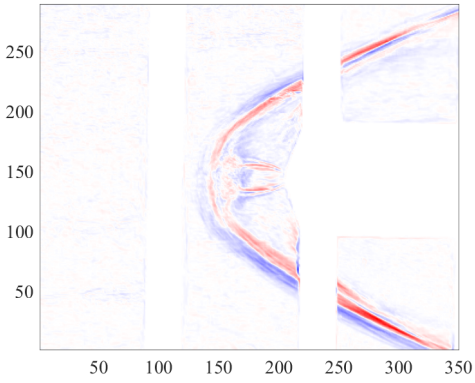

(d) Mode 3

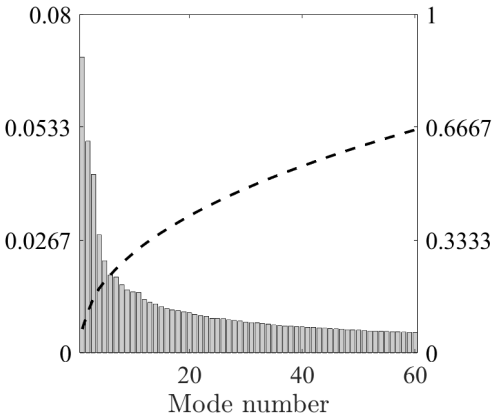

(e) Modal Energy Distribution

Figure 6.3: Typical example of oscillation with a Mach 4 center nozzle at C_T = 0.2 and $\alpha = 0^\circ$.

(a) Video Frame

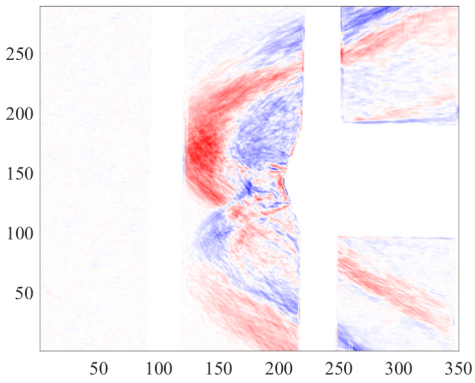

(b) Mode 1

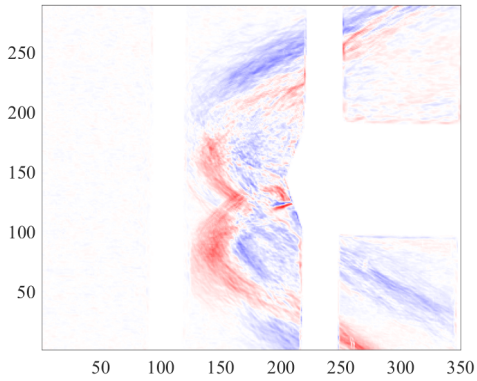

(c) Mode 2

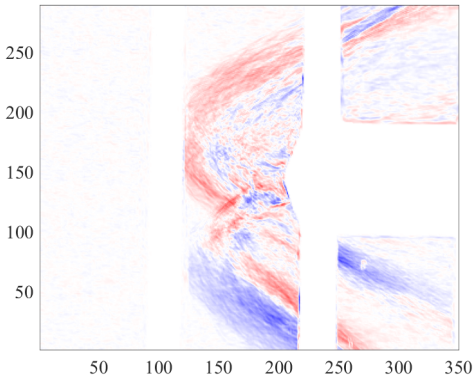

(d) Mode 3

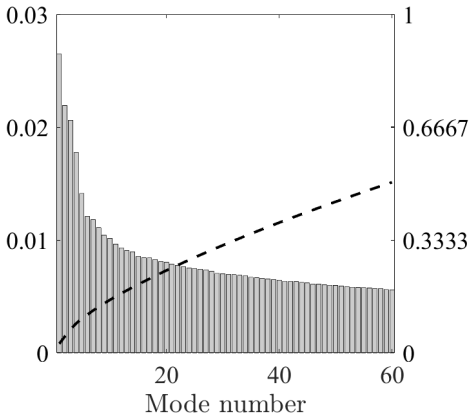

(e) Modal Energy Distribution

Figure 6.4: Typical example of an oscillating case exhibiting shock penetration with a Mach 4 tri nozzle at C_T = 0.5 and $\alpha = 0^{\circ}$.

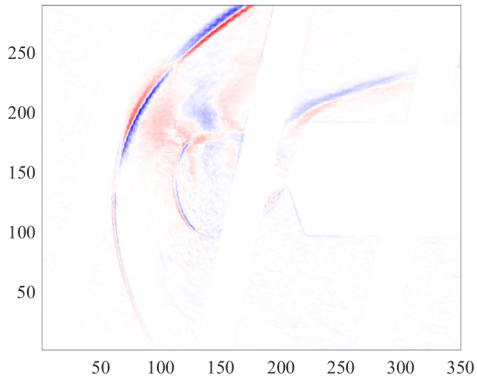

(a) Mode 1

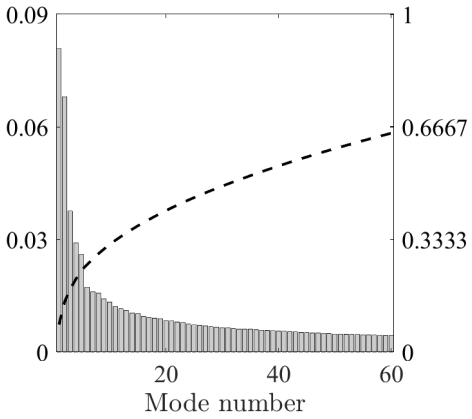

(b) Modal Energy Distribution

Figure 6.5: Case 318: Center nozzle Mach 2, C_T=2, α=12°.

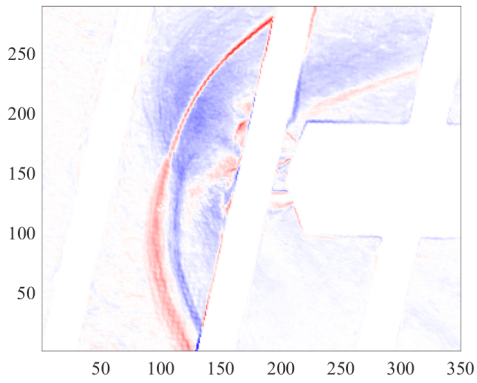

(a) Mode 1

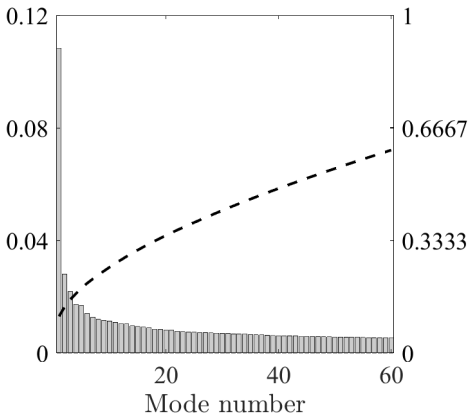

(b) Modal Energy Distribution

Figure 6.6: Case 194: Tri-nozzle, Mach 2, C_T 2, α=12°.

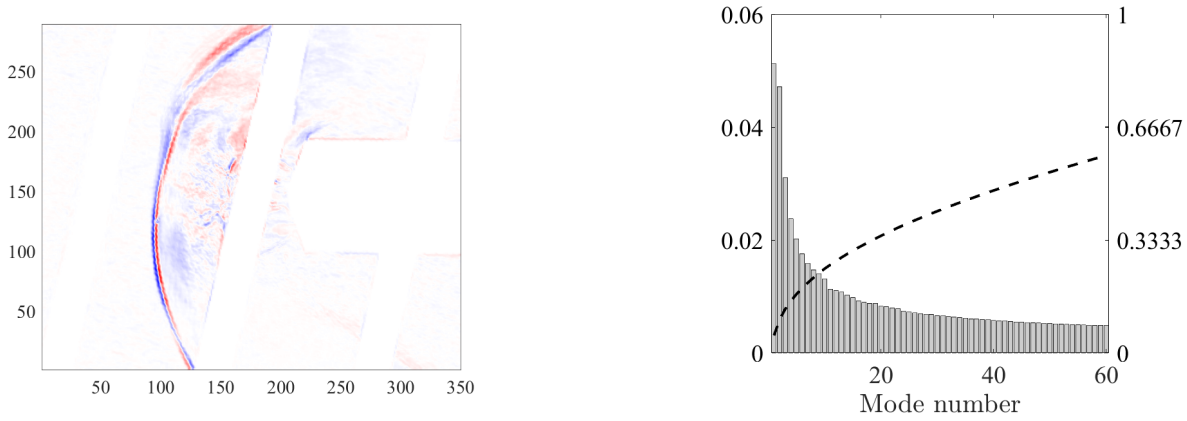

(a) Mode 1

(b) Modal Energy Distribution

Figure 6.7: Case 288: Quad nozzle, Mach 2, C_T 2, α=12°.

0° case is steady, with each mode showing little to no motion. The 4° case is relatively steady, with a bit more motion shown in the shock bands of the POD modes. At 8°, unsteadiness can be seen; the shock bands of both the top and bottom of each shock can be seen, with some separation between the red and blue shock bands in each portion of the shock. At 12 °, the case is quite unsteady, with oscillation occurring, particularly in the bottom half of the shock. The shock band for the lower half of the shock is thick and not well defined, suggesting a high level of motion throughout the run. At 20°, the oscillation has clearly lessened from that seen in the 12° case, however, the shock does appear to exhibit more motion than at 8°. While it cannot be concluded that 12° is the angle of attack with the highest amplitude of unsteadiness due to the lack of other comparable cases between 8° and 20°, the data suggests that the case with the highest amplitude of oscillation lies in this angle of attack range. This is a common finding in many cases. While some cases' oscillation amplitude increases with angle of attack all the way up to the 20 degree run, other cases seem to peak around 12 degrees and become more steady by 20 degrees.

As coefficient of thrust is increased, instability typically decreases, as seen in Section 5.1.

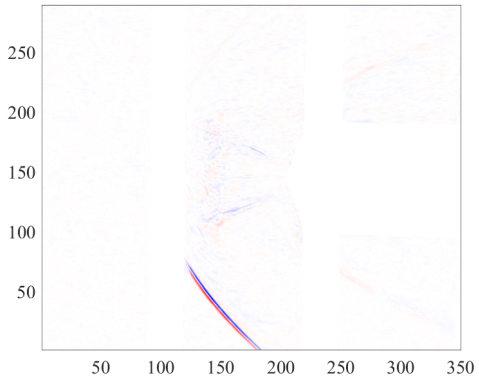

(a) Mode 1

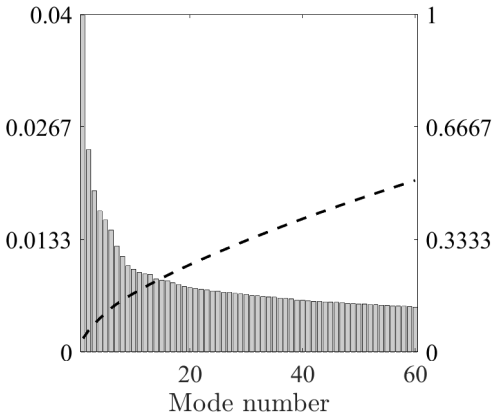

(b) Modal Energy Distribution

Figure 6.8: Case 139: Center nozzle, Mach 2, C_T=1, α=0°

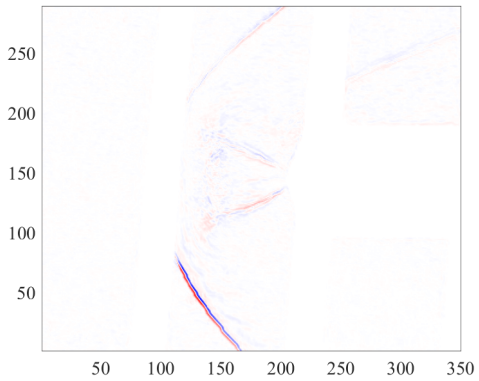

(a) Mode 1

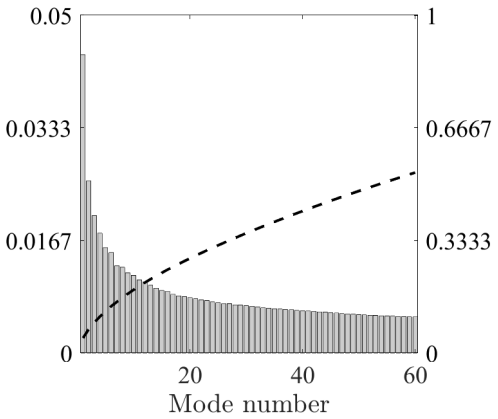

(b) Modal Energy Distribution

Figure 6.9: Case 139: Center nozzle, Mach 2, C_T=1, α=4°.

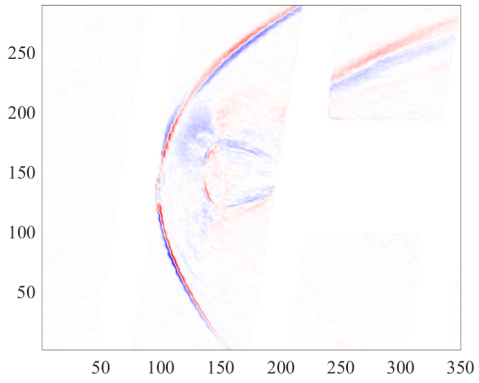

(a) Mode 1

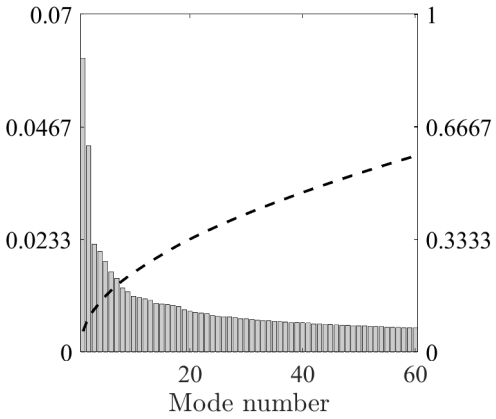

(b) Modal Energy Distribution

Figure 6.10: Case 139: Center nozzle, Mach 2, C_T=1, α=8°.

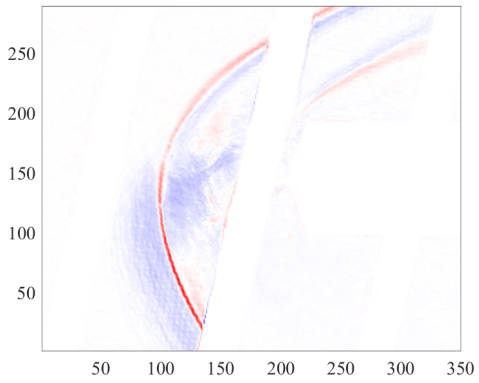

(a) Mode 1

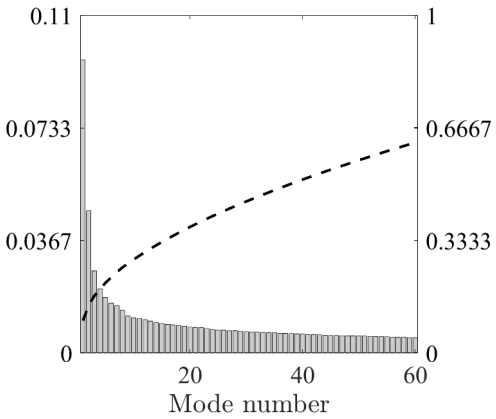

(b) Modal Energy Distribution

Figure 6.11: Case 139: Center nozzle, Mach 2, C_T=1, α=12°.

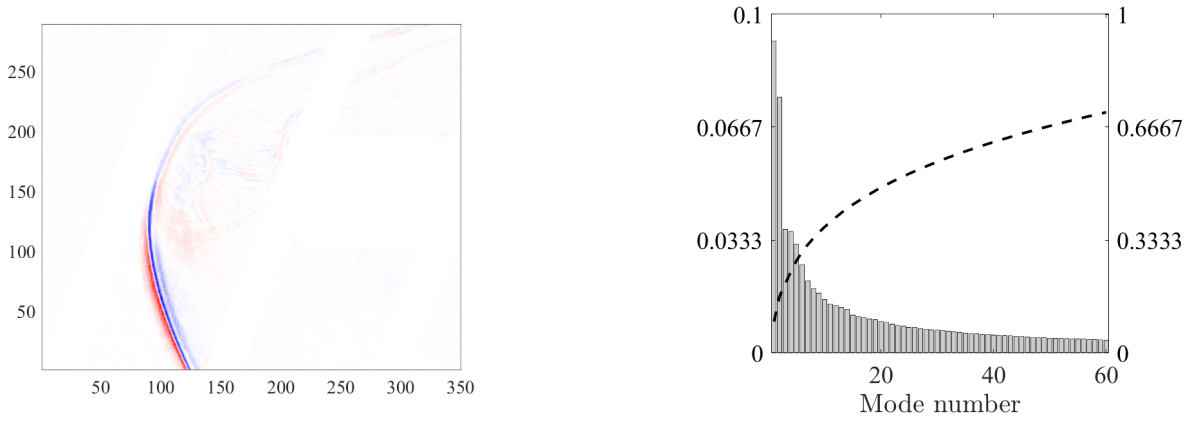

(a) Mode 1

(b) Modal Energy Distribution

Figure 6.12: Case 139: Center nozzle, Mach 2, C_T=1, α=20°.

At the lower coefficients of thrust in the NASA dataset for center nozzle cases (between 0.25 and 2), there is typically a high amount of shock oscillation. As thrust coefficient gets into the higher regime taken in this study (from 2 to 6), the cases become quite a bit more stable. The C_T which the flow becomes fully stable is dependent on the nozzle configuration, with center nozzle cases becoming steady at lower C_T values than multi-nozzle cases. A quad-nozzle, Mach 2, angle of attack 0° case is shown at three C_T values, 0.5, 1, and 2. The C_T =0.5 case, Figure 6.13, is quite unsteady, with thick, undefined shock bands that have a relatively large distance between them. While mode 2 of this case shows quite a bit of background motion, the three highest energy modes shown here all describe the high amplitude shock oscillation of this case. Comparing the C_T =0.5 case with the C_T =1 case shown in Figure 6.14, it is clear that as the coefficient of thrust was increased, there was a significant decrease in the amplitude of shock motion. Shock bands are thinner, with slightly smaller distances in between the bands. As C_T is increased to 2, shown in Figure 6.15, the shock becomes completely steady. Modes 1 and 2 of this case represent motion of the background flow, meaning that this is the majority of flow pattern existing for the

video taken in this case. Mode 3 shows only the top portion of the shock, with quite thin shock bands, having no separation between them. These characteristics are typical of a steady case containing no shock motion. The trend towards steadiness seen in these figures as C_T increases is a common trend across the dataset, with many cases above C_T =2 being steady and all cases in the higher C_T regime, such as at C_T =5 and 6, being completely steady. When shock penetration occurs, however, unsteadiness amplitude can trend in the opposite direction. With a quad-nozzle at Mach 3, angle of attack 0°, there is a steady case, taken at C_T =2 and a case exhibiting shock penetration at C_T =3. These two cases are shown in Figures 6.16 and 6.17. The C_T =2 case is relatively steady, with a very small amplitude of shock oscillation, as seen in modes 2 and 3. Mode 1 of this case describes a steady shock and contains a much higher amount of energy than the following modes. The case at C_T =3, however, exhibits a high amplitude of shock oscillation and penetration, with the shock penetrating the flow at the two nozzle locations visible in the frame. The top and bottom of the flow in each of the three modes contains shock bands that are thick and undefined, which penetrate through the shock. The modal energy corresponding to each of the first few modes in this case are relatively close in energy when compared to the modal energy distribution in Figure 6.16. Because of the more complex flow dynamics associated with the unsteadiness in the C_T = 3 case, more modes are necessary to capture the dominant flow dynamics. The different shock unsteadiness results as coefficient of thrust is increased seen in these two examples may point to a different result by each type of unsteadiness as coefficient of thrust changes.

Figure 6.18 shows a tri-nozzle, Mach 2, C_T 0.5 angle of attack 0 case. This case shows oscillation in two locations, due to the nature of the tri-nozzle. The modes of each oscillating portion of the shock display a small amplitude of motion and not well defined shock bands. The modes in Figure 6.19, a tri-nozzle case with the same parameters at a freestream Mach number of 3, describe oscillation with a higher amplitude of motion, shown by thicker shock bands than those of the corresponding Mach 2 case. At freestream Mach 3, depicted by Figure 6.20, The shock bands are farther out from the nozzle front and are thicker and

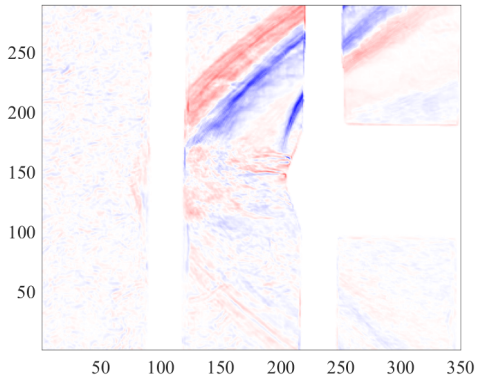

(a) Mode 1

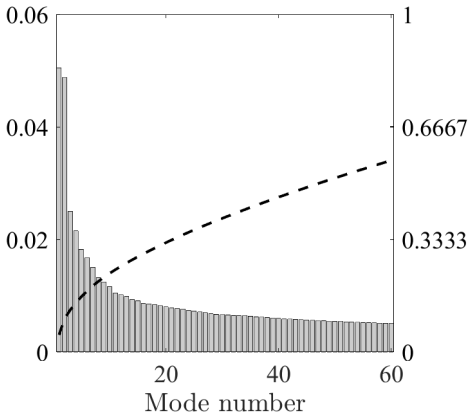

(b) Modal Energy Distribution

Figure 6.13: Case 286: Quad nozzle, Mach 2, C_T=0.5, α=0°

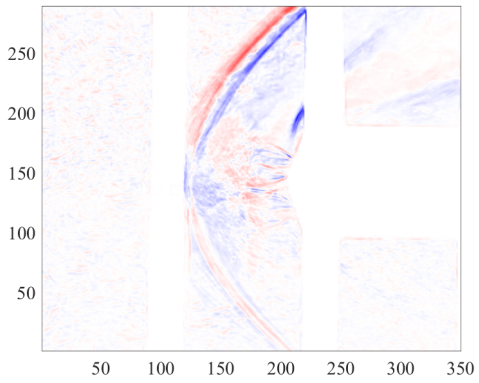

(a) Mode 1

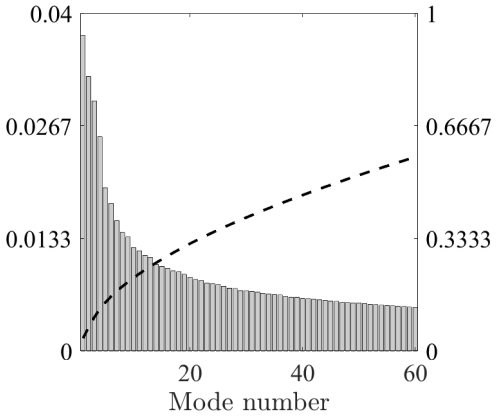

(b) Modal Energy Distribution

Figure 6.14: Case 286: Quad nozzle, Mach 2, C_T=1, α=0°.

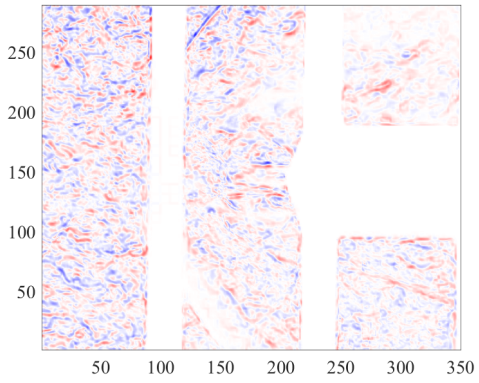

(a) Mode 1

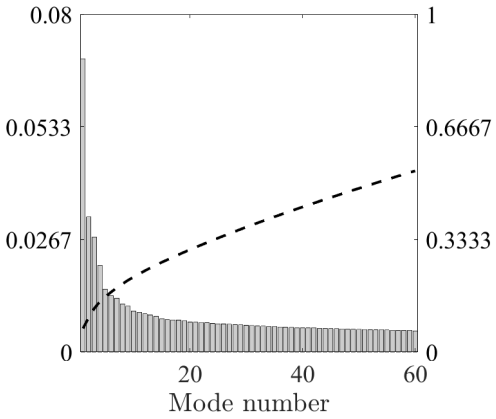

(b) Modal Energy Distribution

Figure 6.15: Case 286: Quad nozzle, Mach 2, C_T=2, α=0°.

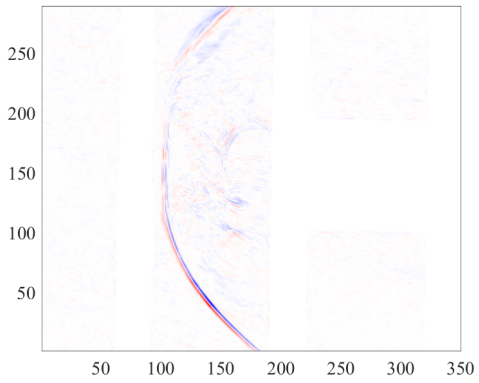

(a) Mode 1

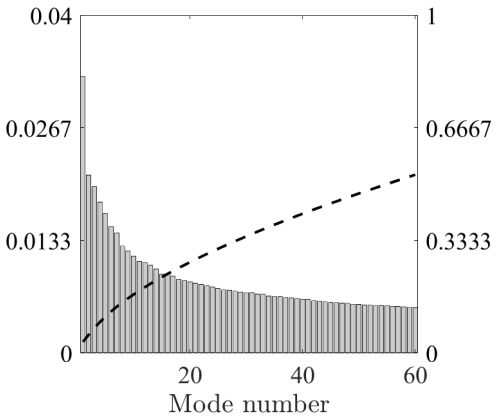

(b) Modal Energy Distribution

Figure 6.16: Case 306: Quad nozzle, Mach 3, C_T=2, α=0°.

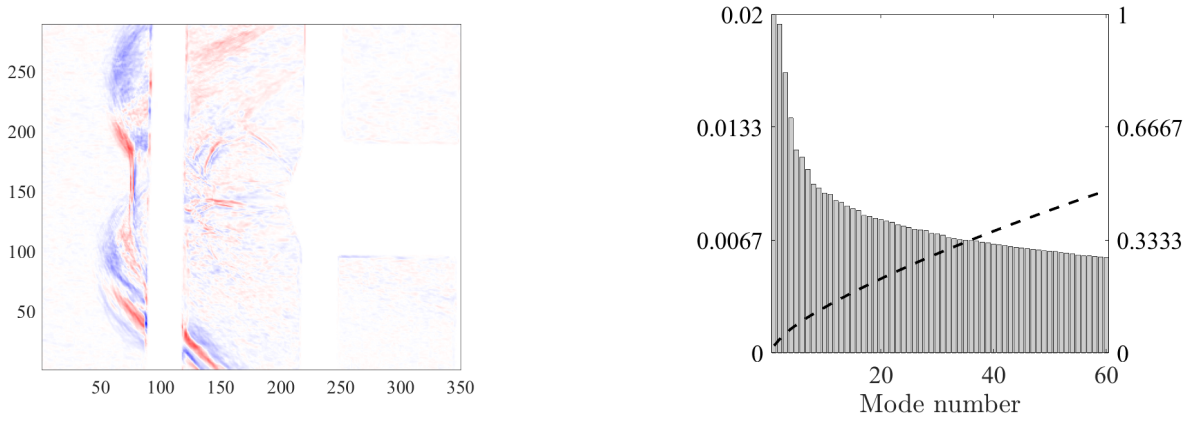

(a) Mode 1

(b) Modal Energy Distribution

Figure 6.17: Case 306: Quad nozzle, Mach 3, C_T=3, α=0°.

darker than the two earlier cases. The bars of the wind tunnel apparatus that are visible in each of these three cases are helpful in visualizing how far the furthest points of the shock in each case occur. In the Mach 2 case, Figure 6.18, the front-most points of the shock are visible, occurring in between the two apparatus bars. In the Mach 3 and 4 cases, however, the front points of the shocks are covered by the right-most bar, showing how far in front of the nozzle the shock is reaching with this higher shock oscillation amplitude.

6.3 POD of Transition Data

The Nitrogen-Nitrogen 1/8 inch nozzle case is bi-modal in that the run is steady for about half of the video taken and exhibits shock oscillation for the remainder of the video. The first four POD modes of the unsteady portion of the run are given in Figure 6.21, along with the modal energy distribution in Figure B.8f. The first four modes contain a majority of the energy, with modes 5 and higher decreasing in energy dramatically. Looking at mode 5 in Figure B.8e, more of the flow patterns shown are due to background motion and therefore mode 5 does not describe the shock oscillation well. The shock exhibits a small amplitude

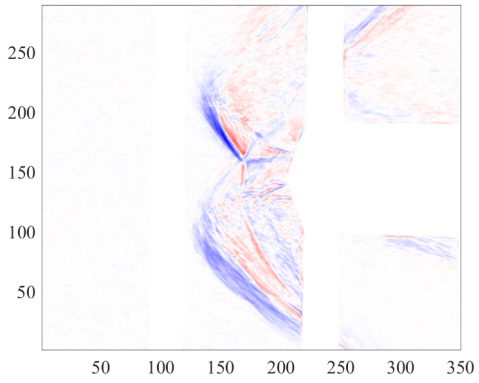

(a) Mode 1

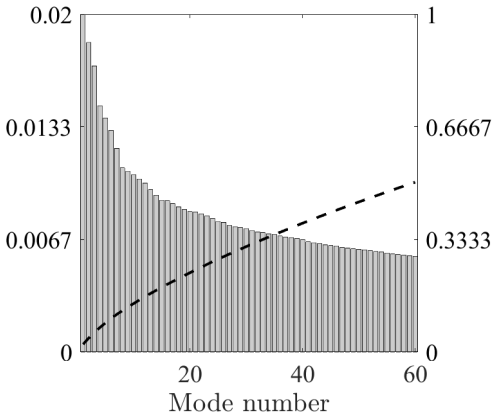

(b) Modal Energy Distribution

Figure 6.18: Case 202: Tri nozzle, Mach 2, C_T=0.5, α=0°.

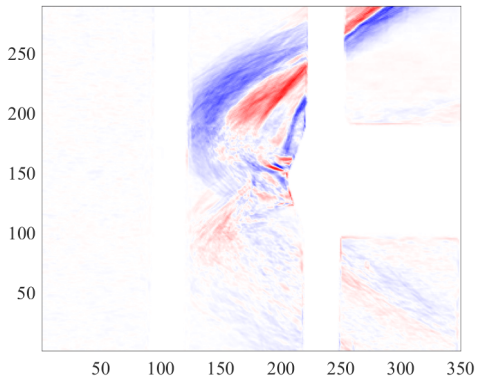

(a) Mode 1

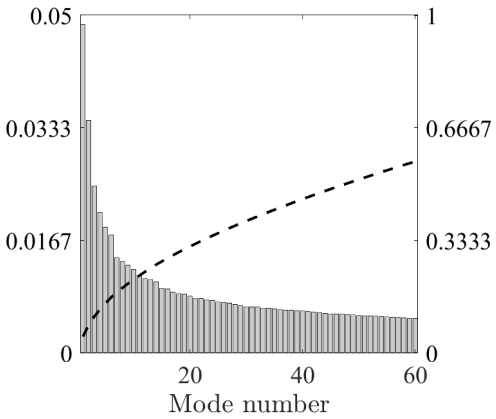

(b) Modal Energy Distribution

Figure 6.19: Case 266: Tri nozzle, Mach 3, C_T=0.5, α=0°.

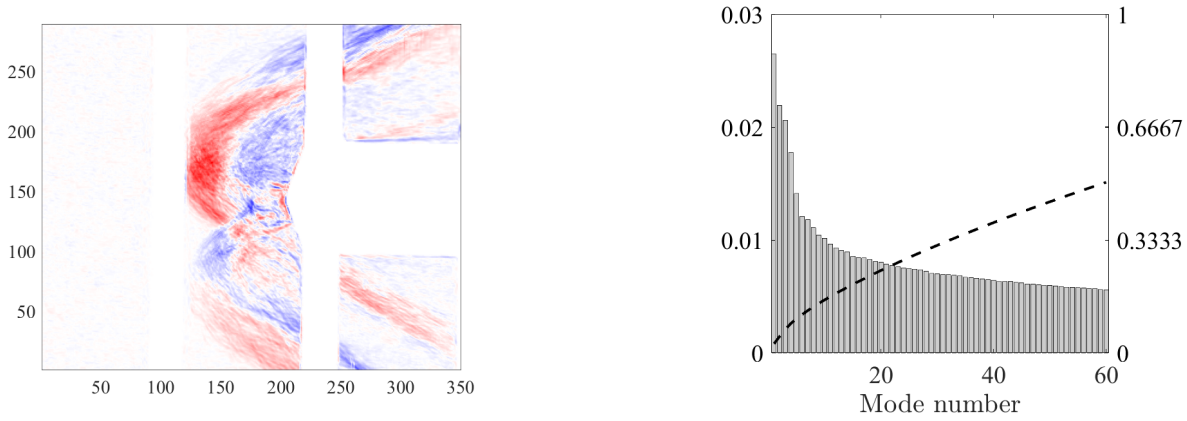

(a) Mode 1

(b) Modal Energy Distribution

Figure 6.20: Case 253: Tri nozzle, Mach 4, C_T=0.5, α=0°.

of oscillation, shown by the shock bands in the POD modes. The colored shock bands on modes 2 and 4, as well as on modes 1 and 4, are offset by half a wavelength each. These modes describe the back and forth motion of the shock when paired together. This case exhibits mainly a back and forth oscillation motion and not as much of the flapping motion that can be seen in several other cases. Both the modal activation distributions for modes 1 and 4, shown in Figure B.9a, and modes 2 and 4, Figure B.9b, show a circular distribution, although there is a heavier distribution on the bottom half of the circle.

The Nitrogen-Nitrogen 1/4 inch nozzle case is another bimodal case in which the shock oscillates forward and backward and also flaps for approximately the first third of the run and is steady for the remainder of the run. The first five POD modes for the unsteady portion of the video are given in Figure 6.23, as well as the energy distribution. Modes 1 and 3, as well as modes 3 and 4 are each a modal pair, showing shock locations a half a wavelength from each other. Modes 1 and 4 show similar motion, with shock locations in the same positions. Since the shock in this case showed a flapping motion along with the shock oscillation, the shock bands are much larger than those in the Nitrogen-Nitrogen 1/8 inch nozzle case, where the

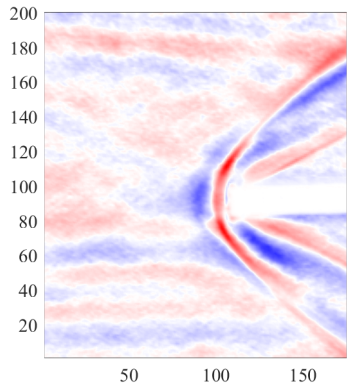

(a) Mode 1

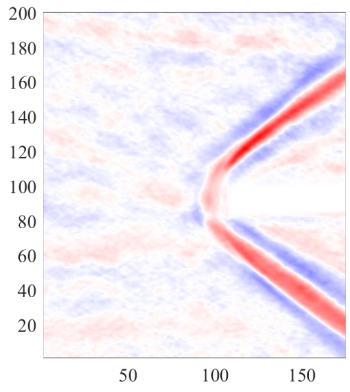

(b) Mode 2

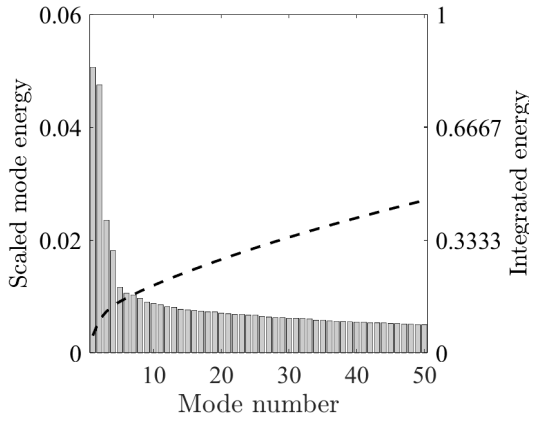

(c) Modal Energies

Figure 6.21: Nitrogen-Nitrogen 1/8 inch nozzle POD modes and energy distribution.

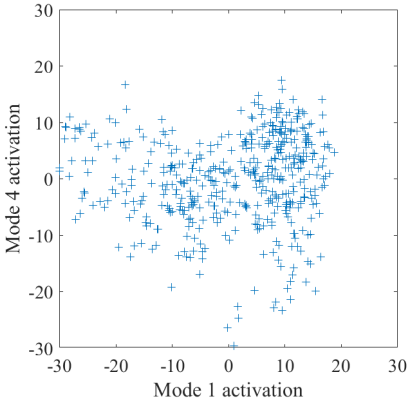

(a) Mode activations of modes 1 and 4

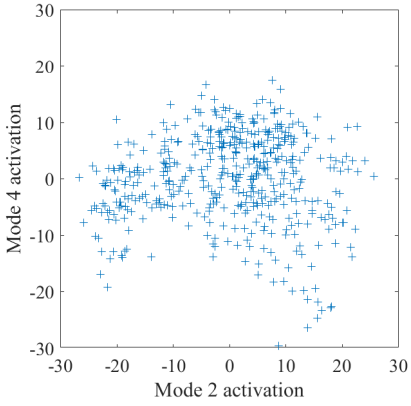

(b) Mode activations of modes 2 and 4

Figure 6.22: Nitrogen-Nitrogen 1/8 inch nozzle POD modes.

shock simply oscillates back and forth. The modal activation energies for these two pairs of modes were plotted against each other and are shown in Figure 6.24. While the activations of modes 1 and 3 do show a doughnut-like pattern, suggesting sinusoidal interaction, the activations of modes 3 and 4 show a more dispersed circular pattern.

Both a transitional and a fully unsteady case were found for the Nitrogen-Nitrogen 3/8 inch nozzle case. The transitional case, at a P_e/P_{02} = 0.7, exhibited bi-modal unsteadiness, with the shock oscillating and flapping for the first half of the video taken and remaining steady for the second half. The first mode and its activation energy throughout time are shown in Figure 6.25, along with the energy of each mode. Mode 1, an oscillatory mode, carries most of the energy of the flow motion throughout the run. The remaining modes decrease quite quickly in energy and are more indicative of background flow motion when the shock is steady. The modal activation throughout time, shown in Figure B.12b, gives further insight into the cause of this, showing the bimodal nature of the shock at this pressure ratio. The motion indicated by the first POD mode is apparent for the first 50 frames of the video, with the remaining 100 frames not exhibiting this flow pattern. From video results,

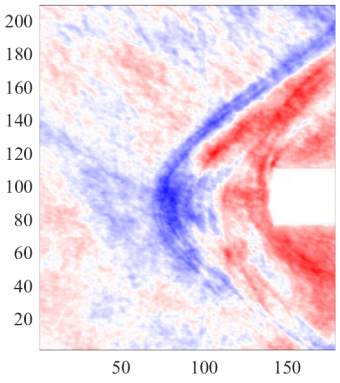

(a) Mode 1

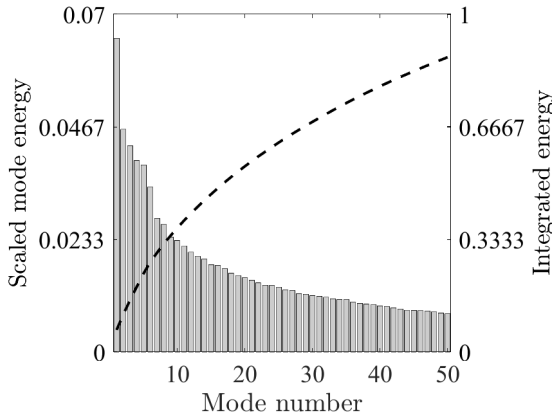

(b) Modal Energies

Figure 6.23: Nitrogen-Nitrogen 1/4 inch nozzle POD modes.

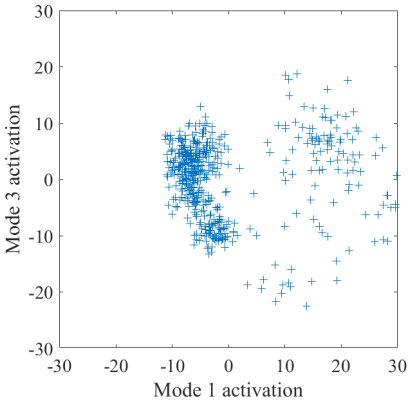

(a) Mode activations of modes 1 and 3

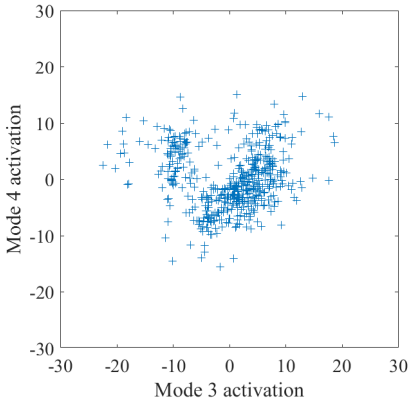

(b) Mode activations of modes 3 and 4

Figure 6.24: Nitrogen-Nitrogen 1/4 inch nozzle POD modes.

the shock clearly becomes steady for the rest of the video. Therefore, the unsteady portion of the video was pulled out of the full video for this case and POD was conducted using just the 50 unsteady frames. The results of this are shown in Figure 6.26. The shock bands of the unsteady frames shown in modes 1 and 2 of this case are offset by a half a wavelength, with their activation coefficients, when plotted against one another, creating the bottom of a half circle, a common distribution among paired modes in this dataset. For the Nitrogen-Nitrogen 3/8 inch nozzle, another case at P_e/P_{02} = 0.6 was also taken, which exhibited shock unsteadiness throughout the entirety of the run. The shock was both oscillating and flapping, as shown in the POD modes for this case in Figure 6.28. This motion was well captured by the first five modes, although since there is both oscillation and flapping of the shock, flow patterns are complex. Modes 1 and 4 represent the same oscillatory flow pattern, as do modes 3 and 5 for the top of the shock. For the bottom half of the shock, however, modes 3 and 5 show the back and forth motion. Modes 1 and 3 are the best representation of the shock motion, with each shock band being offset by a half a wavelength for both the top and bottom of the shock.

The Carbon Dioxide-Helium unsteady cases all have a much greater shock standoff distance than their corresponding Nitrogen-Nitrogen unsteady cases. The Carbon Dioxide-Helium 1/4 inch nozzle unsteady case is shown in X(show some stuff from full video). The video for this case was therefore cropped to the X unsteady frames and a POD analysis was conducted on that portion of the run. The results of this analysis are shown in Figure 6.29. Due to the activity of the gas in the background, the Carbon Dioxide-Helium cases displayed a larger amount of background motion in each mode, however, shock patterns can still be seen. Modes 1, 2, and 3 show horizontal lines above and below the nozzle, showing the high amount of forward and backward motion of this case. Modes 1 and 2 represent similar shock motion, while mode 4 pairs with each of these to show shock motion at a half a wavelength's distance away, suggesting that together they show the back and forth oscillation of the shock.

The Carbon Dioxide-Helium 3/8 inch nozzle case displays a bimodality of a different nature than the previously discussed cases. While some earlier cases exhibited an unsteady

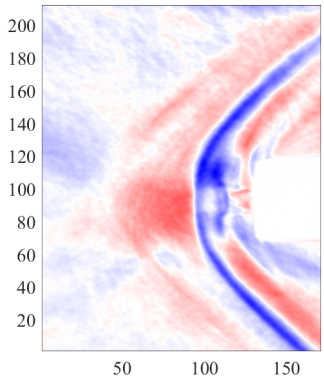

(a) Mode activations of modes 1 and 3

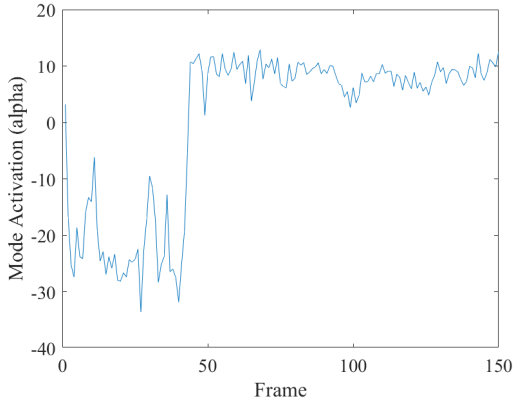

(b) Mode activations of modes 3 and 4

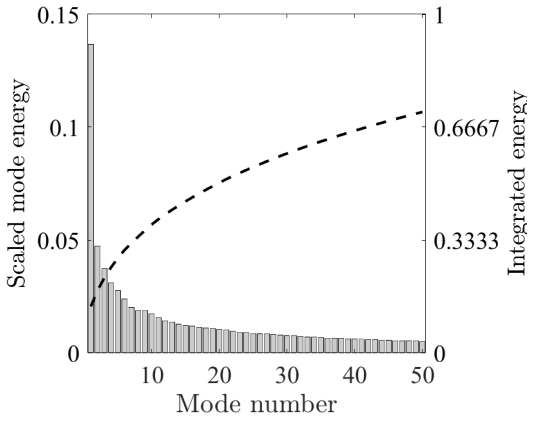

(c) Mode activations of modes 3 and 4

Figure 6.25: Nitrogen-Nitrogen 1/4 inch nozzle POD modes.

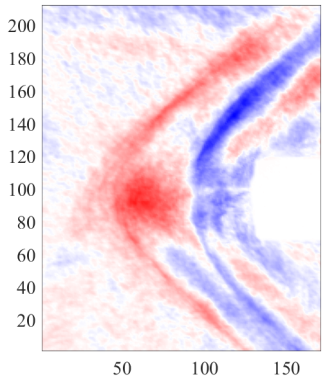

(a) Mode 1

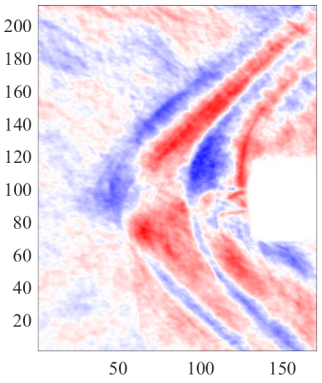

(b) Mode 2

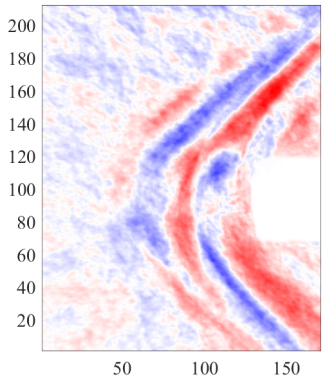

(c) Mode 3

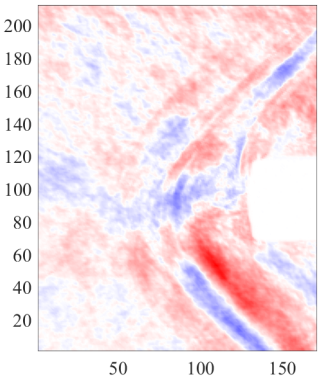

(d) Mode 4

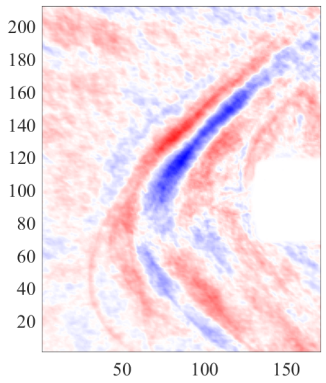

(e) Mode 5

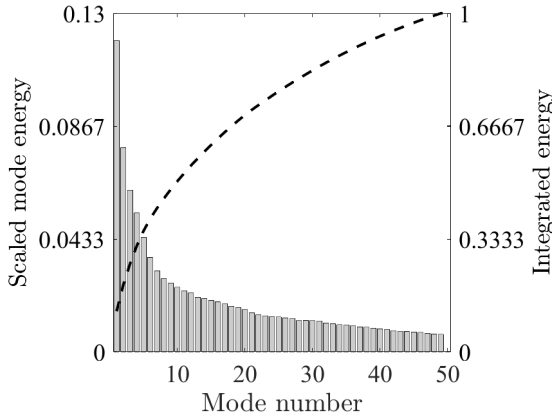

(f) Modal Energies

Figure 6.26: Nitrogen-Nitrogen 3/8 inch nozzle POD modes, P_e/P_{02} =0.7.

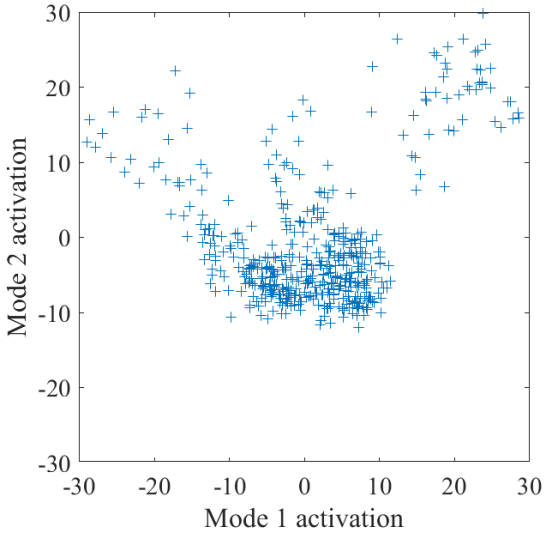

Figure 6.27: Modal activation coefficients for modes 1 and 2, Ni-Ni 3/8 inch nozzle, P_e/P_{02} =0.7.

portion of the video and a steady portion of the video, this case contained two different modes of unsteadiness. Both types of unsteadiness consisted of shock oscillation and shock flapping, however, the shock had a longer standoff distance for the first 100 video frames than in the last 150 video frames. The first mode and its corresponding activation in time are shown in Figure 6.30. There is a clear split between the two ways unsteadiness is presenting itself in this activation plot, with the activation dropping drastically around frame 100: the point at which the shock moves closer to the nozzle front. For this reason, the run was split into two pieces for the POD analysis, one for the unsteadiness at the longer standoff distance and one for the shorter standoff distance. The unsteadiness type at the shorter standoff distance is shown in Figure 6.31. As with the 1/4 inch Carbon Dioxide-Helium case, there are horizontal lines present above and below the nozzle for modes 1-3, representing the heavy forward and backward motion of the shock. The shock bands in modes 1 and 2 correspond to the main shock extremes during an oscillation cycle, while mode 5 seems to show a wider range of shock locations. The modes of shock oscillation occurring at the longer shock

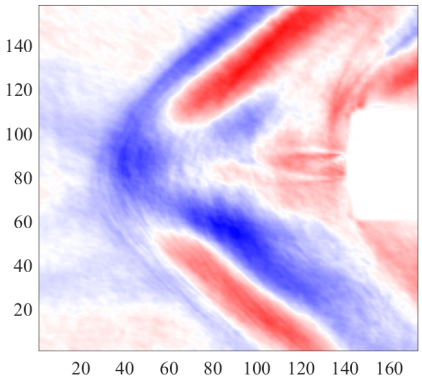

(a) Mode 1

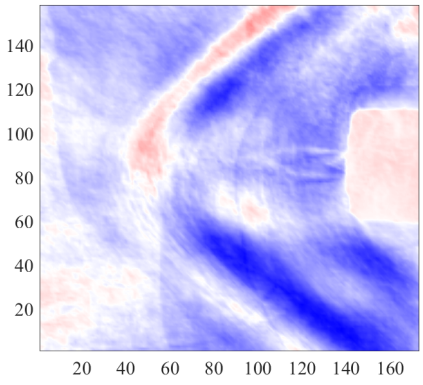

(b) Mode 2

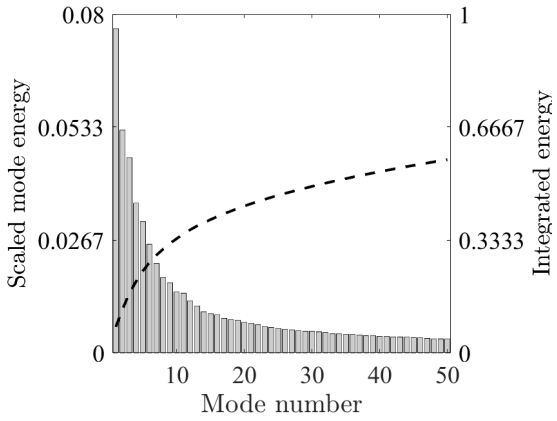

(c) Modal Energies

Figure 6.28: Nitrogen-Nitrogen 3/8 inch nozzle POD modes, P_e/P_{02} =0.6.

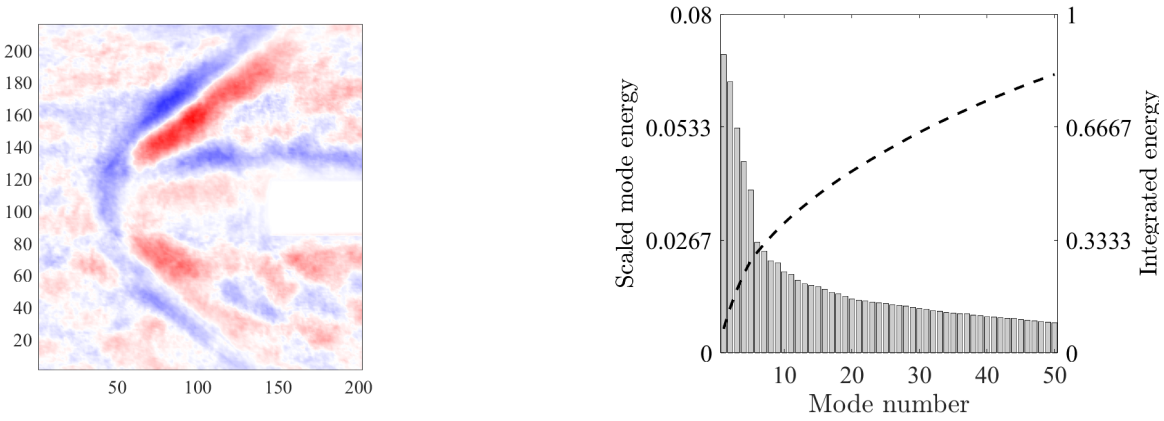

(a) Mode 1

(b) Modal Energies

Figure 6.29: Carbon Dioxide-Helium 1/4 inch nozzle POD modes.

standoff distance distance are shown in Figure 6.32. The modes here exhibit a much stronger set of horizontal lines above and below the nozzle, describing a much more energetic forward and backward motion for this type of unsteadiness.

6.4 Discussion

The Proper Orthogonal Decomposition analysis of each dataset reinforces trends seen with earlier analyses of the data: shock instability depends, at least in part, on each parameter. With a different nozzle configuration, coefficient of thrust, angle of attack, forebody size, and gas combination, the flow topology of the shock unsteadiness can change drastically. POD is a promising method for creating a low dimensional representation of the oscillatory motion of the shock in certain conditions. While some unstable shock flowfields are quite complex and will require a larger number of modes in order to capture the dominant flow patterns, cases that exhibit a simple harmonic motion of shock oscillation can often be captured in up to five modes. Plotting the modal activation coefficients against each other can give an insight into the pairing of the two modes, revealing when the oscillation motion can be described as

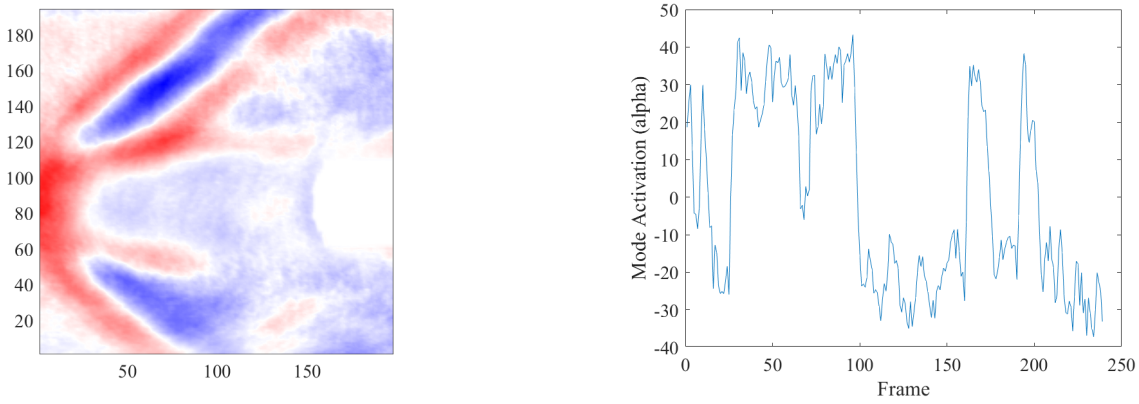

(a) Mode

(b) Mode activations

Figure 6.30: Nitrogen-Nitrogen 1/4 inch nozzle POD modes.

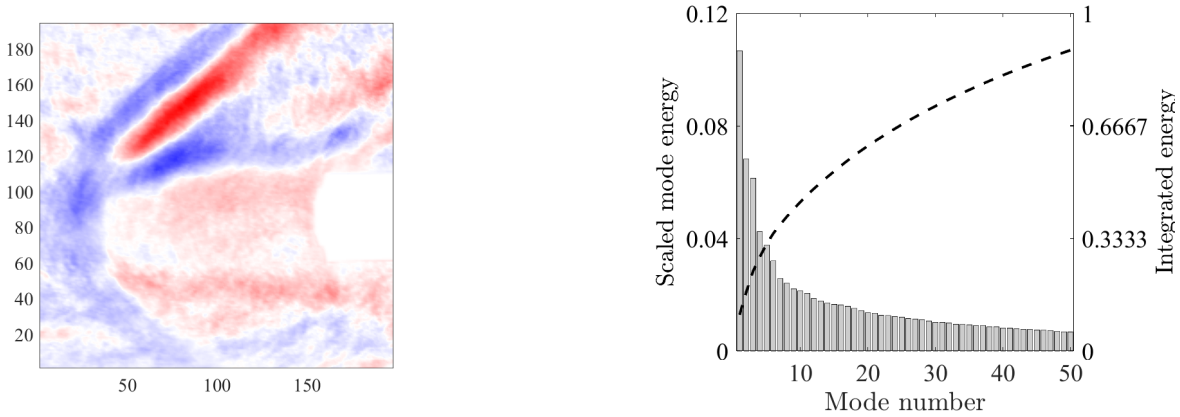

(a) Mode 1

(b) Modal Energies

Figure 6.31: Carbon Dioxide-Helium 3/8 inch nozzle POD modes, unsteady type 1.

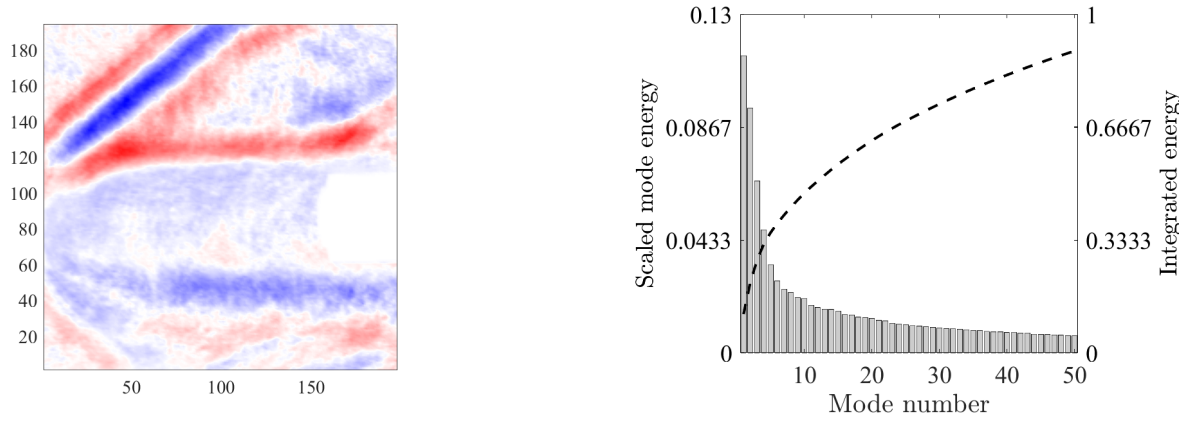

(a) Mode 1

(b) Modal Energies

Figure 6.32: Carbon Dioxide-Helium 3/8 inch nozzle POD modes, unsteady type 2.

simply a harmonic motion. POD results can be used in the future for frequency analyses. The frequency of the dominant shock motion can be found and utilized in conjunction with the shock amplitude calculations in order to quantify how shock oscillation frequency and amplitude change with each varying parameter. Generalization between different cases is difficult due to different features of each case being extracted by POD depending on the structure of the flow, however, POD gives some insight into the dominant features of shock oscillation and creates a good lower-order representation of the flowfield dynamics.

Chapter 7

CONCLUSION

Past SRP instability studies have suggested that shocks were steady at very low and very high coefficients of thrust. There is a region in between these steady regimes where SRP shocks were found to be unsteady: either exhibiting shock oscillation, flapping, or penetration. Korzun and Cassel[6], Ho[5], and Yang[14] concluded that the transition from steady flow may occur at a total pressure around 1, or in the case of Shang[9], between 0.8 and 1.05. Jarvinen and Adams[4] found that their dataset transitioned from steady to unsteady flow around a pressure ratio of 7. However, a definite transition to this unsteady regime was unknown. This thesis has endeavored to characterize the effect that changing flow parameters has on shock instability, as well as to better understand how flow parameters change the onset of instability.

With an increase in forebody area, amplitude of unsteadiness as well as shock standoff distance were found to increase. The Nitrogen-Nitrogen gas combination cases tended to have a lower shock standoff distance and oscillation amplitude than the corresponding Carbon Dioxide-Helium cases. Contrary to what was previously thought, transition to unsteadiness did not consistently occur around a P_e/P_{02} of 1, nor did it occur around a $P_{0t}/P_{0\infty}$ of 7. Instead, as forebody was decreased, the transition pressure, P_{crit} and C_T were also lowered. The Mach 3 cases tested transitioned to unsteadiness at far higher C_T values than the corresponding Mach 2 cases. The unsteady cases taken near transition taken tended to show intermittent unsteadiness, suggesting that the shock is quite sensitive near transition.

Shocks from the two datasets presented in this study were classified as steady, oscillating, and oscillating with shock penetration. The oscillating cases included shocks exhibiting both flapping motion and back and forth large-scale oscillation of the shock. The multi-nozzle

cases were difficult to generalize, as shock dynamics were more complex and often exhibited more shock penetration than single-nozzle cases. From the SRP data taken by NASA in the Unitary wind tunnel at various freestream Mach numbers, trends in some characteristics of flow unsteadiness were observed. In the center nozzle configuration, there was a transition from a steady shock to an oscillating shock as C_T decreased and nozzle angle of attack increased. This relation seemed to be more dependent on C_T than on pressure ratio. When looking at C_T and Mach number for center nozzles, shock oscillation began to occur at Mach 4, with a lower coefficient of thrust producing heavier oscillation.

The Proper Orthogonal Decomposition analysis provided a lower-order representation of each unstable shock case taken. Using the modal energies suggested that the flow could be described within the first 5 modes in many cases. Modal activation coefficients pointed to the pairing of several modes in each case, with modes that described shock oscillation creating circular plots that suggested a simple harmonic motion of oscillation. Continued work with the POD analyses could provide a frequency associated with each shock oscillation, which, when paired with the amplitude of shock oscillation will give a deeper quantitative look at how the shock dynamics change with each changing parameter. Taking further unsteady data at the University of Washington with the existing nozzle forebody sizes and gas combinations at varying angles of attack will provide a better understanding of how angle of attack affects the transition to unsteadiness.

BIBLIOGRAPHY

[1] Berry, S. A., Rhode, M. N., Edquist, K. T., and Player, C. J., "Supersonic retropropulsion experimental results from the NASA Langley unitary plan wind tunnel," *42nd AIAA Thermophysics Conference*, 2011.

[2] Daso, E., Pritchett, V., Wang, T.-S., Ota, D., Blankson, I., and Auslender, A., "The dynamics of shock dispersion and interactions in supersonic freestreams with counterflowing jets," *AIAA Journal*, Vol. 47, No. 6, 2007.

[3] Romeo, D. J. and Sterrett, J. R., "Exploratory investigation of the effect of a forward-facing jet on the bow shock of a blunt body in a Mach number 6 free stream," Tech. rep., Technical Note D-1605, National Aeronatuics and Space Administration, 1963.

[4] Jarvinen, P. O. and Adams, R. H., "The aerodynamic characteristics of large angled cones with retrorockets," Tech. rep., Contract No. NAS: 7-576, National Aeronautics and Space Administration, 1970.

[5] Ho, B., *Characterizing unsteadiness in supersonic retropropulsion flows*, Master's thesis, University of Washington, 2019.

[6] Korzun, A. M. and Cassel, L. A., "Scaling and Similitude in single nozzle supersonic retropropulsion aerodynamics interference," *AIAA 2020-0039*, 2020.

[7] Qin, Q., Xu, J., and Wang, B., "Flow instability and asymmetry over spiked cylinder," *Acta Astronautica*, 2021.

[8] Sahoo, D., Kathick, S. K., and Das, S., "Shock-related unsteadiness of axisymmetric spiked bodies in supersonic flow," *Experiments in Fluids*, 2020.

[9] Shang, J. S., Hayes, J., Wurtzler, K., and Strang, W., "Jet-spike bifurcation in high-speed flows," *AIAA Journal*, Vol. 39, No. 6, 2001.

[10] Berry, S., Rhode, M., and Edquist, K., "Supersonic retropropulsion validation experiment in the NASA Langley unitary plan wind tunnel," *Journal of Spacecraft and Rockets*, Vol. 51, No. 3, 2014.

[11] Jennis, E., *Thermodynamic Scaling of Supersonic Retropropulsion Flowfields*, Master's thesis, University of Washington, 2020.

[12] Jennis, E., Jones, L., and Williams, O., "Thermodynamic Scaling of Supersonic Retropropulsion," 2022.

[13] McGhee, R. J., "Effects of a retronozzle located at the apex of a 140° blunt cone at Mach numbers of 3.00, 4.50 and 6.00," Tech. rep., Technical Note D-6002, National Aeronatuics and Space Administration, 1971.

[14] Yang, X., *Influence of jet pressure on multi-nozzle supersonic retropropulsion flowfields*, Master's thesis, University of Washington, 2019.

[15] Romeo, D. J. and Sterrett, J. R., "Flow field for a sonic jet exahusting counter to a hypersonic mainstream," *AIAA Journal*, Vol. 3, No. 3, 1965, pp. 544–546.

[16] Berry, S. A., Rhode, M. N., and Edquist, K. T., "Supersonic Retropropulsion Experimental Results from the NASA Ames 9- x 7-Foot Supersonic Wind Tunnel," *42nd AIAA Thermophysics Conference*, 2012.

[17] Codoni, J. and Berry, S. A., "Analysis of Dynamic Data from Supersonic Retropropulsion Experiments in NASA Langley's Unitary Plan Wind Tunnel," *AIAA Fluid Dynamics Conference and Exhibit*, 2012.

[18] Codoni, J. and Berry, S. A., "Supersonic Reropropulsion Dynamic Data Analysis from NASA Langley Unitary Plan Wind Tunnel," *Journal of Spacecraft and Rockets*, 2014.

[19] Bathel, B., Litzner, C. R., and Jones, S., "High-Speed Schlieren Analysis of Retropropulsion Jet in Mach 10 Flow," *Journal of Spacecraft and Rockets*, 2019.

[20] Feszty, D., Badcock, K., and Richards, B., "Driving mechanisms of high-speed unsteady spiked body flows, Part 1: Pulsation mode." *AIAA J. 42*, 2004.

[21] Tan, Y. M., Yang, X., Ho, B., and Williams, O., "Flow instabiltiies in supersonic retropropulsion flowfields with minimal forebody," *AIAA Journal*, In prep.

[22] Kutz, J. N., *Data-driven modeling & scientific computation: methods for complex systems & big data*, Oxford University Press, 2013.

[23] Korzun, A. M., Cordell, C. E. C. E., and Braun, R. D., "Comparison of inviscid and viscous aerodynamics predictions of supersonic retropropulsion flowfields," *10th AIAA/ASME Joint Thermophysics and Heat Transfer Conference*, 2010.

[24] Finley, P. J., "The flow of a jet from a body opposing a supersonic free stream," *Journal of Fluid Mechanics*, Vol. 26, No. 2, 1966, pp. 337–368.

[25] Korzun, A. and Braun, R., "Performance Characterization of Supersonic Retropropulsion for high-mass Mars Entry systems," *Journal of Spacecraft and Rockets*, Vol. 47, No. 5, 2010.

[26] Korzun, A. M. and Braun, R. D., "Performance Characterization of Supersonic Retropropulsion for Application to high-mass Mars Entry, decent and landing," *AIAA 2009-5613*, 2009.

[27] Cordell, C. E., *Computational fluid dynamcis and analytical modelling of supersonic retropropulsive flowfield strucutres accross a wide range of potential vehicle configurations*, Ph.D. thesis, Georgia Institute of Technology, 2013.

[28] Chang, C.-L., Venkatachari, B. S., and Cheng, G., "Effect of Counterflow Jet on a supersonic reentry capsule," *AIAA 2006-4776*, 2006.

[29] Korzun, A. M., Braun, R. D., and Cruz, J. R., "Survey of supersonic retropropulsion technology for Mars entry, decent and landing," *Journal of Spacecraft and Rockets*, Vol. 46, No. 5, 2009, pp. 929–937.

[30] Schreyer, A.-M., Sahoo, D., Williams, O., and Smits, A., "Experimental Investigation of a Hypersonic Shock Turbulent Boundary Layer Interaction," *AIAA Journal*, Accepted.

[31] Tan, Y. M., *Influence of pressure on supersonic retropropulsion flow field at Mach 2*, Master's thesis, University of Washington, 2018.

Appendix A

ADDITIONAL SHOCK STANDOFF FIGURES

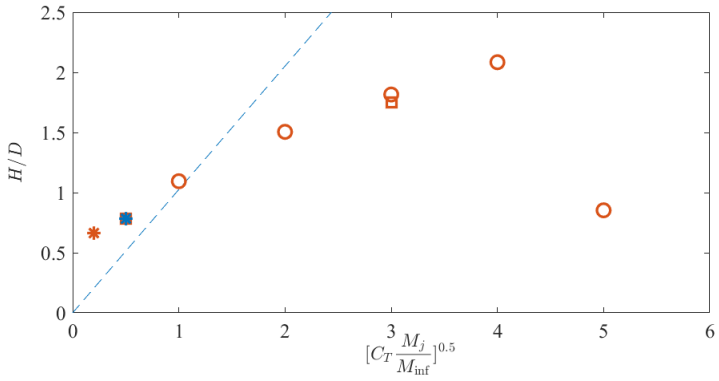

(a) Center nozzle shock standoff.

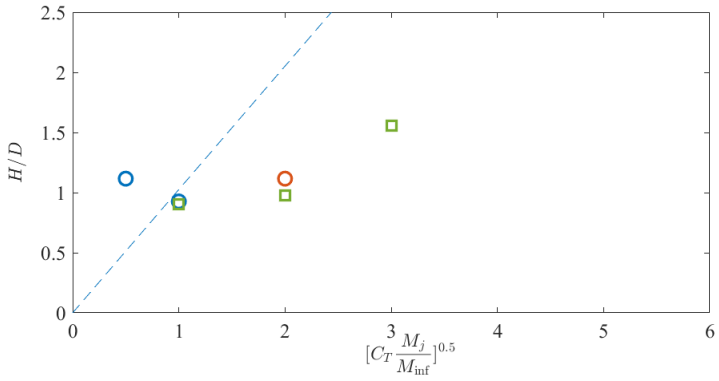

(b) Quad nozzle shock standoff.

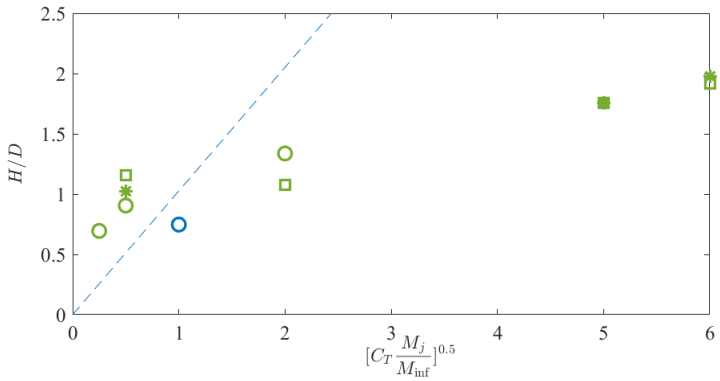

(c) Tri nozzle shock standoff.

Figure A.1: Normalized shock standoff distances of each nozzle configuration.

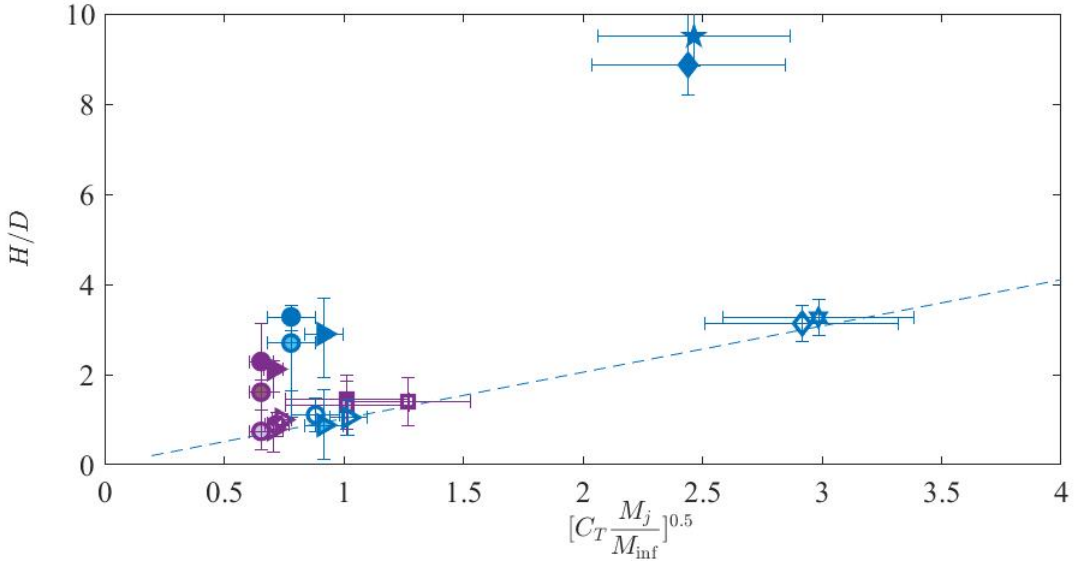

Figure A.2: Shock standoff distance, no legend.

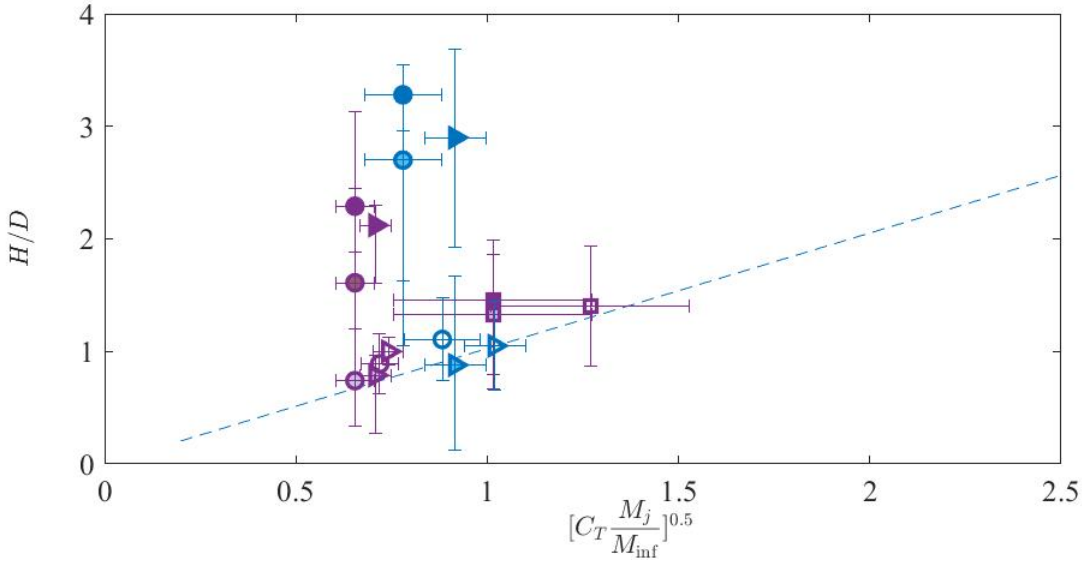

Figure A.3: Shock standoff distance, Mach 2 only.

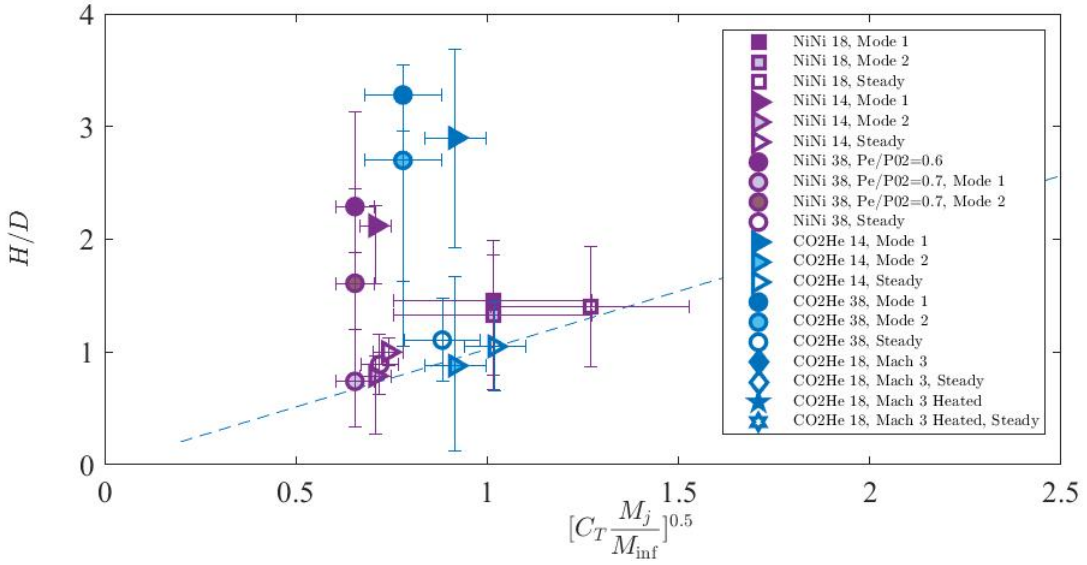

Figure A.4: Shock standoff distance, Mach 2 only.

Appendix B

ADDITIONAL FIGURES, UW DATASET

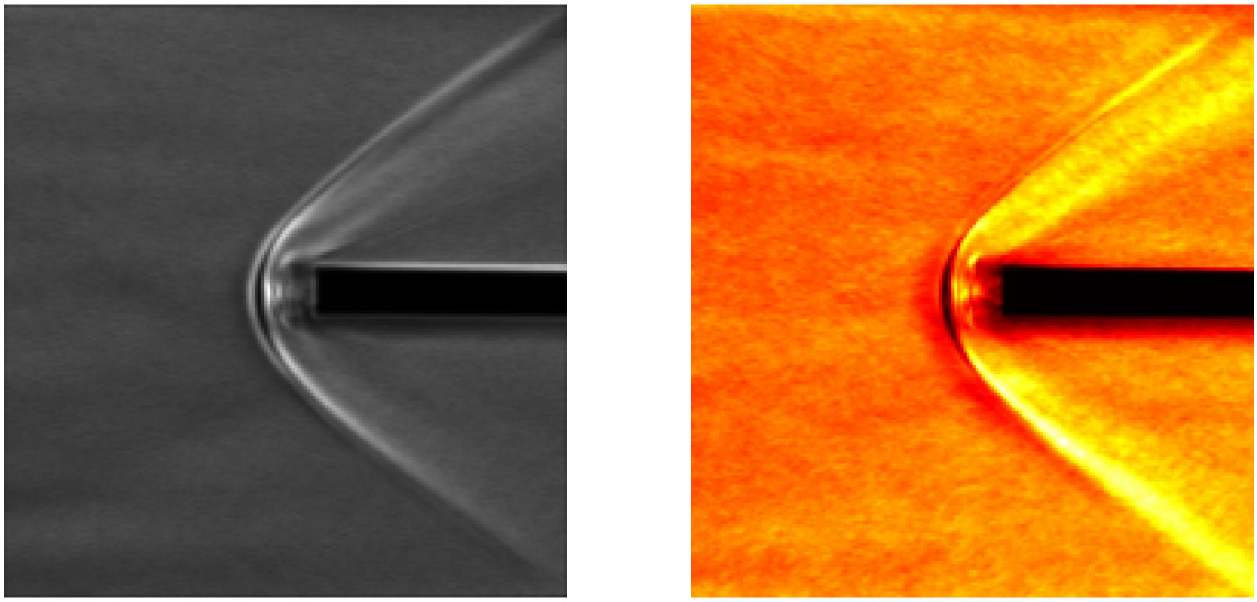

(a) Mean Image

(b) RMS Image

Figure B.1: Ni-Ni 1/8-inch Nozzle, Steady

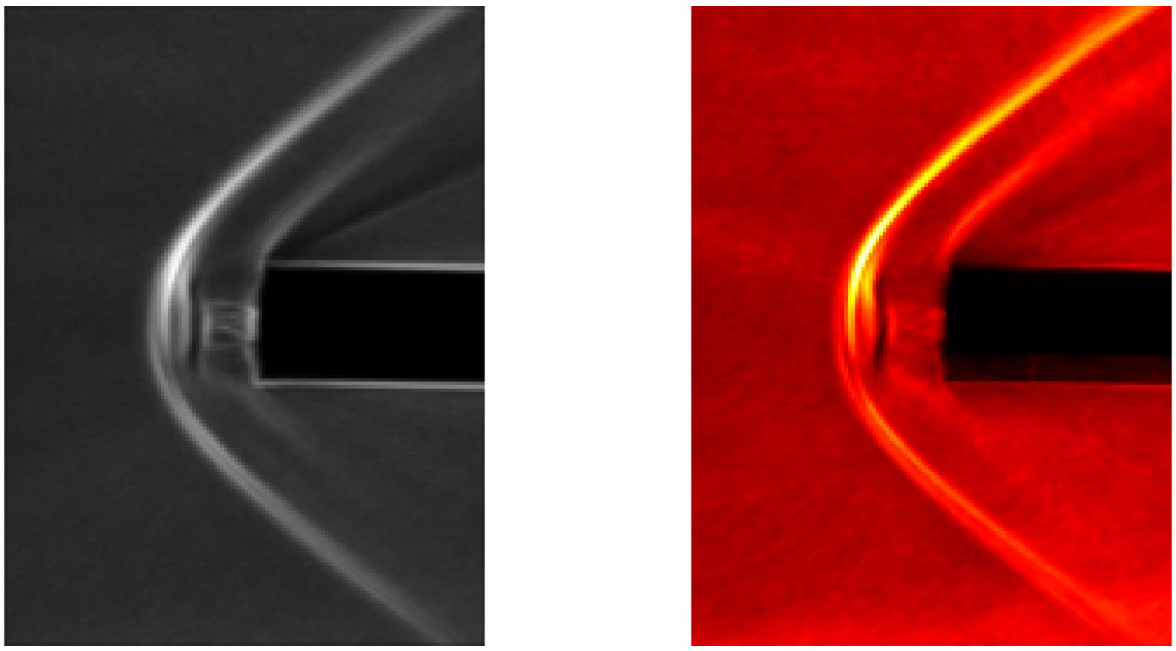

(a) Mean Image

(b) RMS Image

Figure B.2: Ni-Ni 1/4-inch Nozzle, Steady

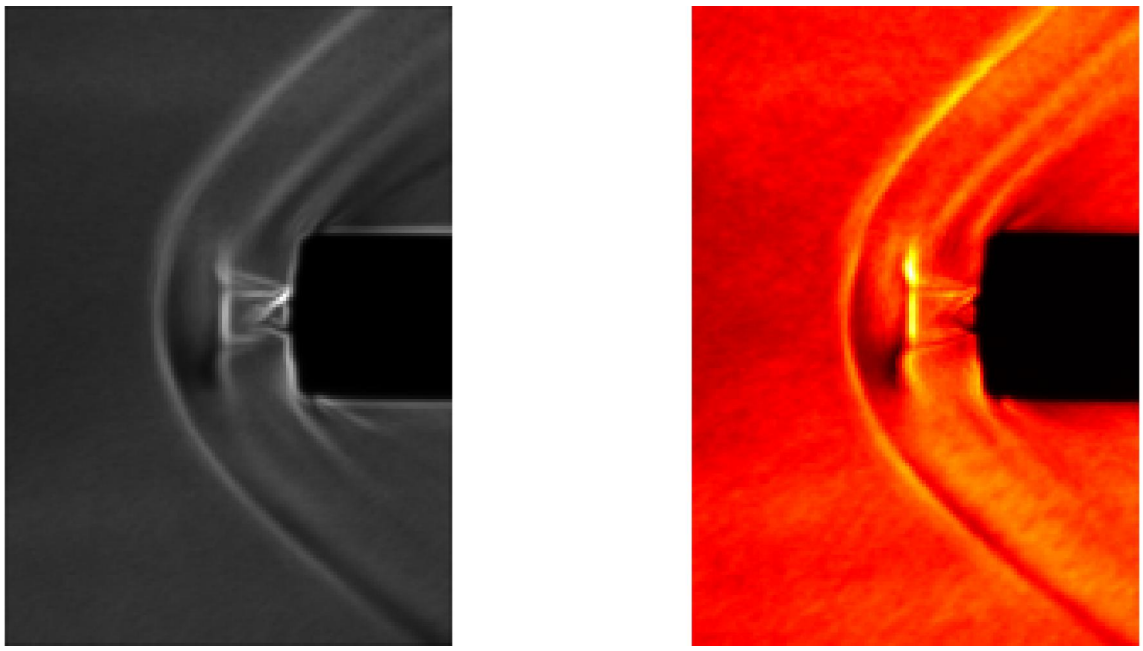

(a) Mean Image

(b) RMS Image

Figure B.3: Ni-Ni 3/8-inch Nozzle, Steady

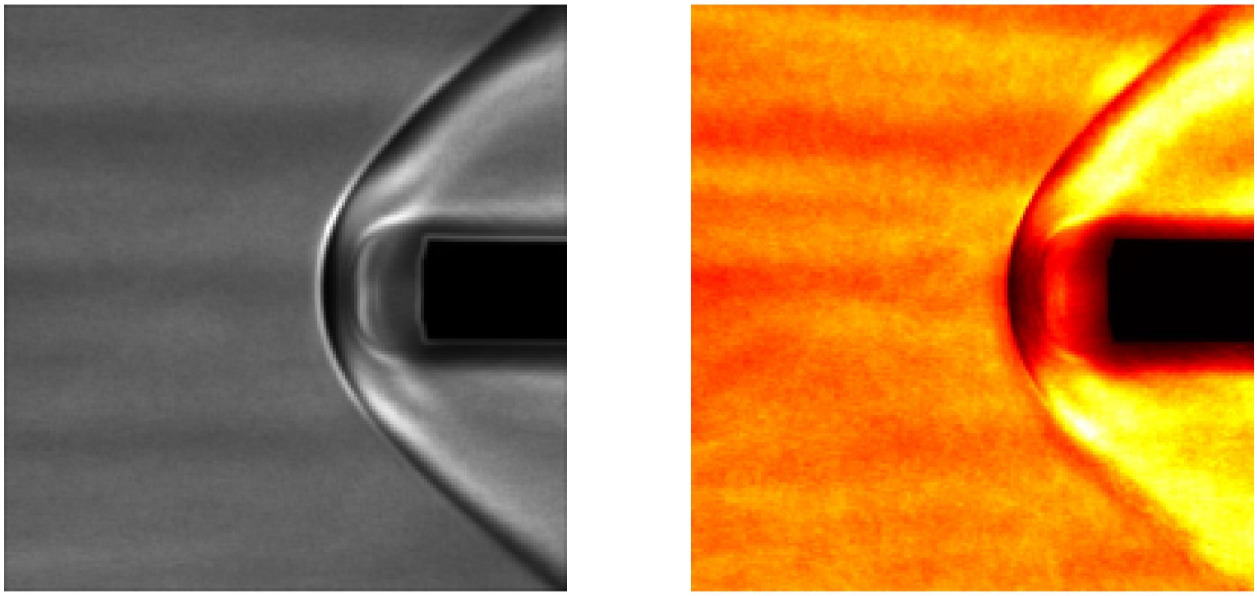

(a) Mean Image

(b) RMS Image

Figure B.4: CO2-He 1/4-inch Nozzle, Steady

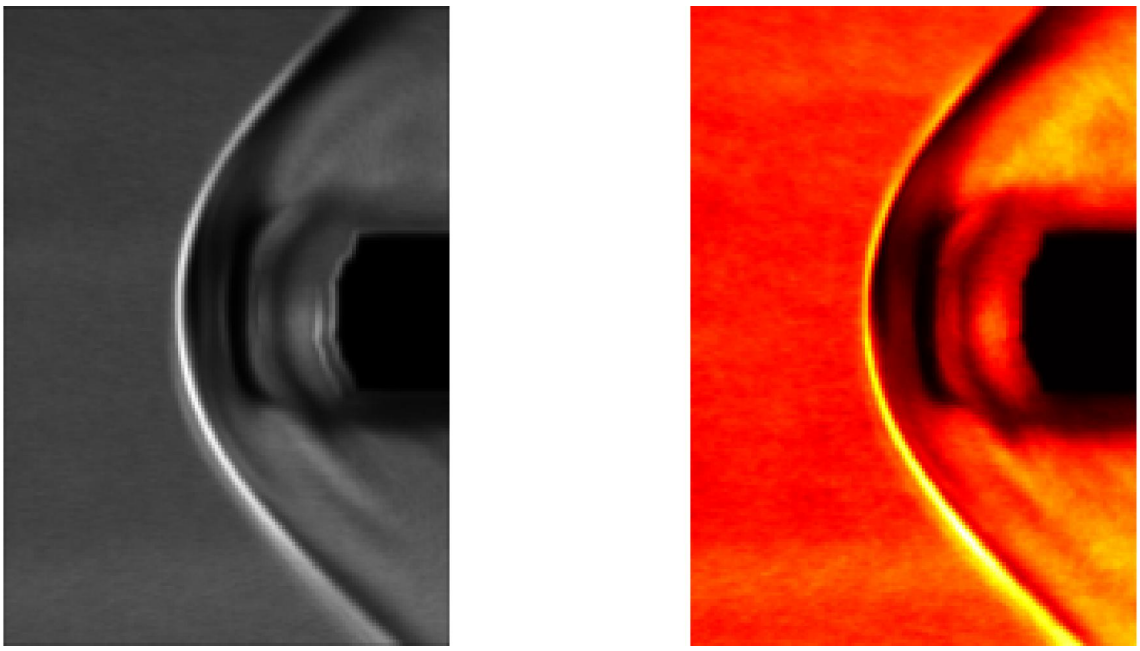

(a) Mean Image

(b) RMS Image

Figure B.5: CO2-He 3/8-inch Nozzle, Steady

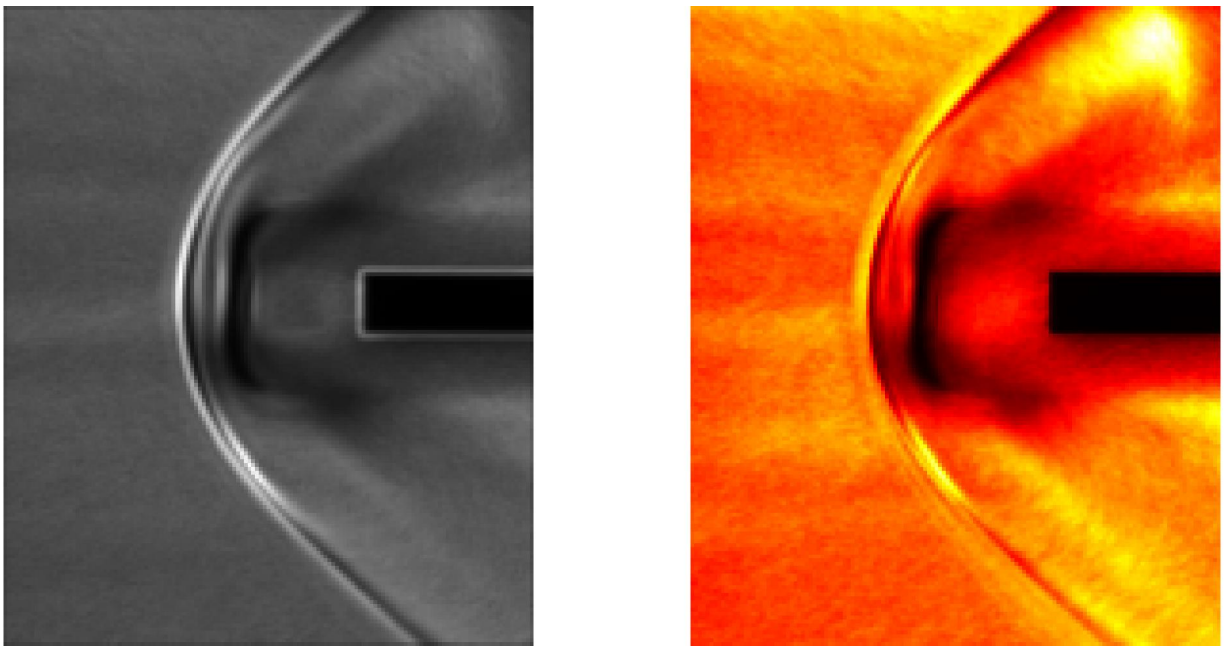

(a) Mean Image

(b) RMS Image

Figure B.6: CO2-He 3/8-inch Nozzle, Steady, Mach 3

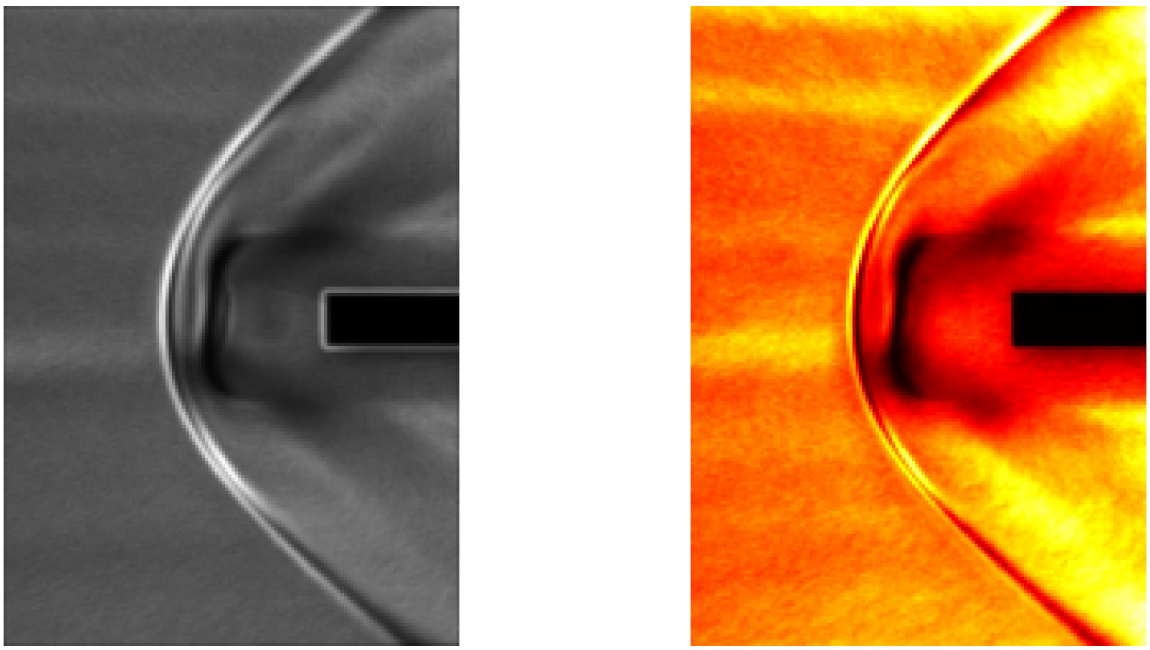

(a) Mean Image

(b) RMS Image

Figure B.7: CO2-He 3/8-inch Nozzle, Steady, Mach 3 Heated

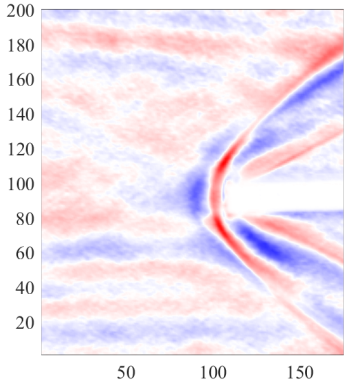

(a) Mode 1

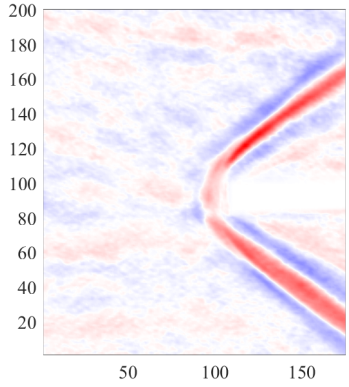

(b) Mode 2

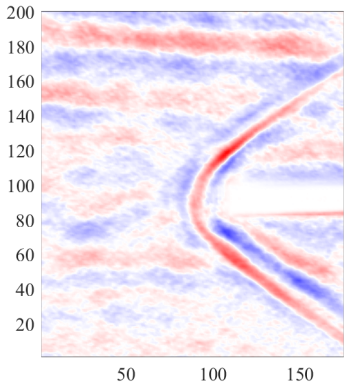

(c) Mode 3

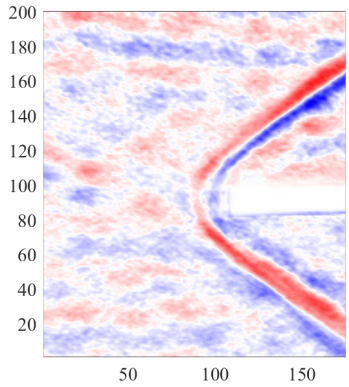

(d) Mode 4

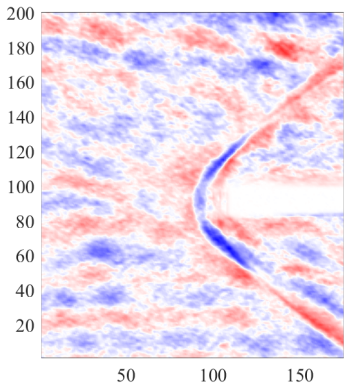

(e) Mode 5

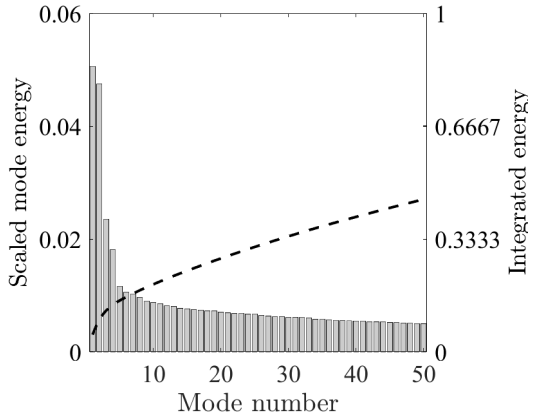

(f) Modal Energies

Figure B.8: Nitrogen-Nitrogen 1/8 inch nozzle POD modes and energy distribution.

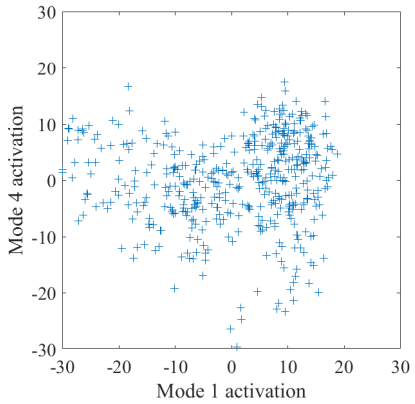

(a) Mode activations of modes 1 and 4

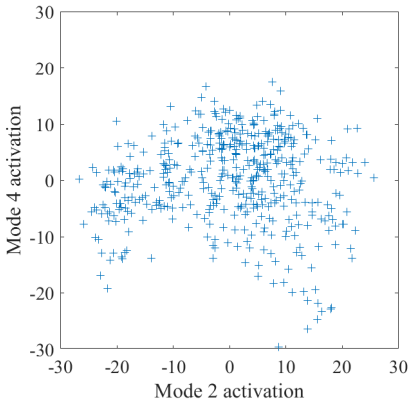

(b) Mode activations of modes 2 and 4

Figure B.9: Nitrogen-Nitrogen 1/8 inch nozzle POD modes.

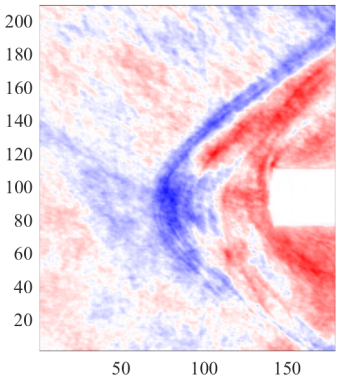

(a) Mode 1

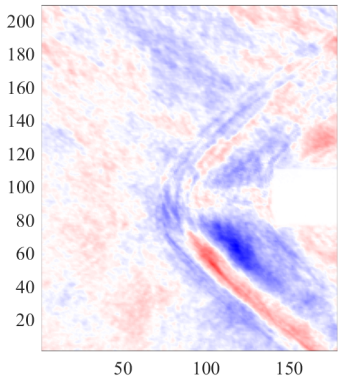

(b) Mode 2

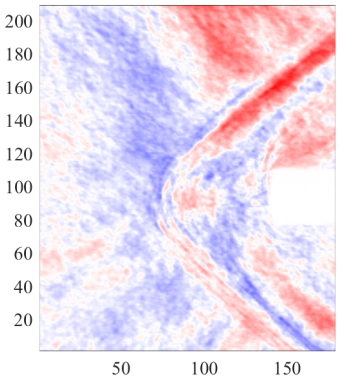

(c) Mode 3

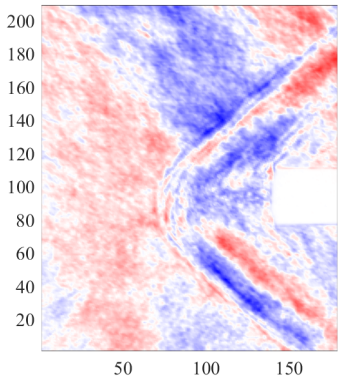

(d) Mode 4

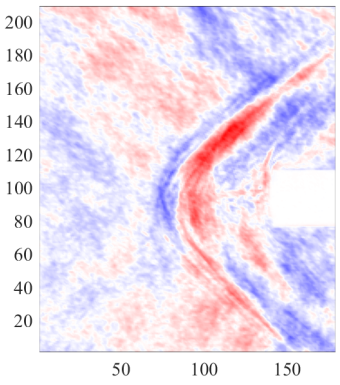

(e) Mode 5

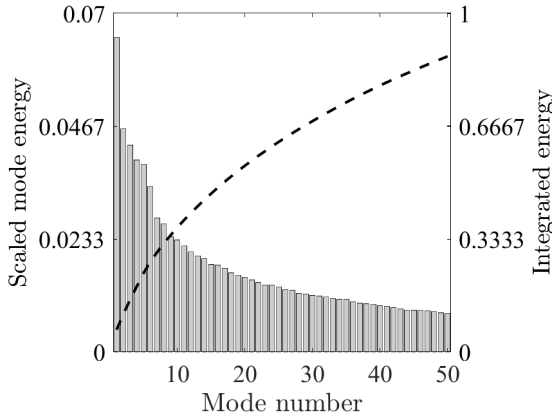

(f) Modal Energies

Figure B.10: Nitrogen-Nitrogen 1/4 inch nozzle POD modes.

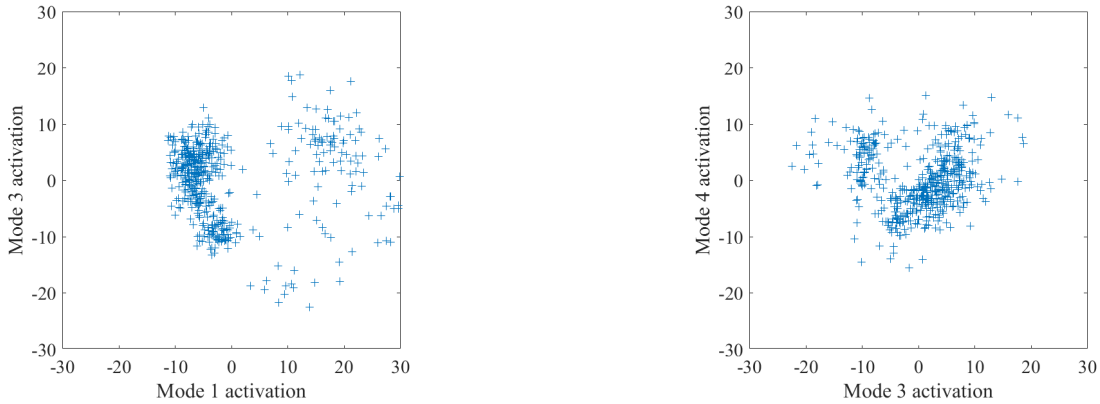

(a) Mode activations of modes 1 and 3

(b) Mode activations of modes 3 and 4

Figure B.11: Nitrogen-Nitrogen 1/4 inch nozzle POD modes.

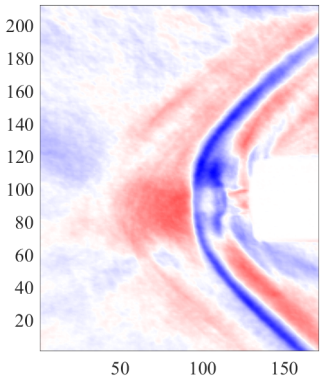

(a) Mode activations of modes 1 and 3

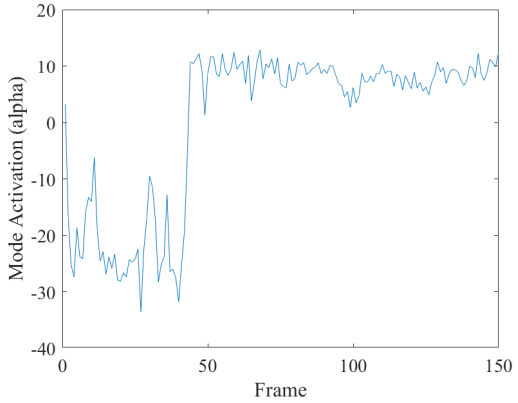

(b) Mode activations of modes 3 and 4

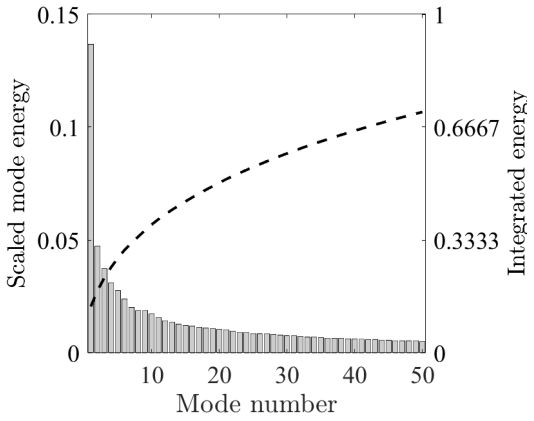

(c) Mode activations of modes 3 and 4

Figure B.12: Nitrogen-Nitrogen 1/4 inch nozzle POD modes.

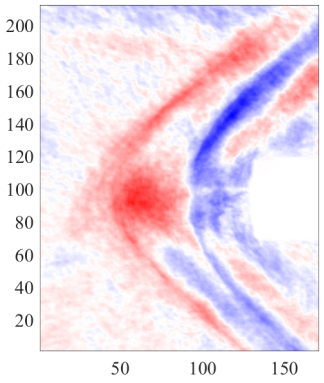

(a) Mode 1

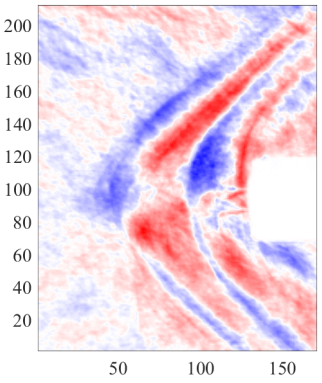

(b) Mode 2

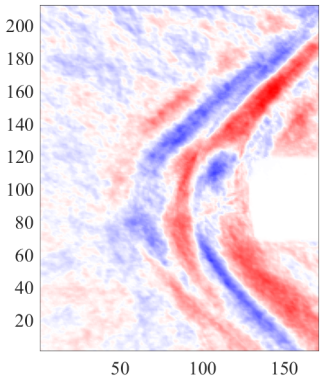

(c) Mode 3

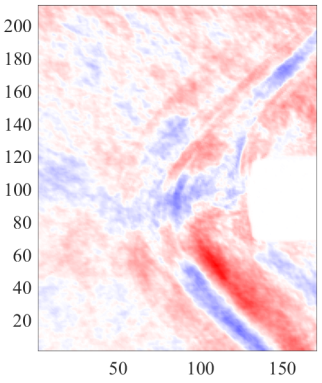

(d) Mode 4

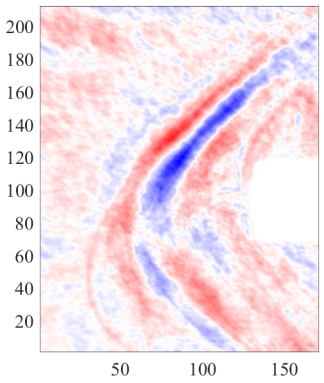

(e) Mode 5

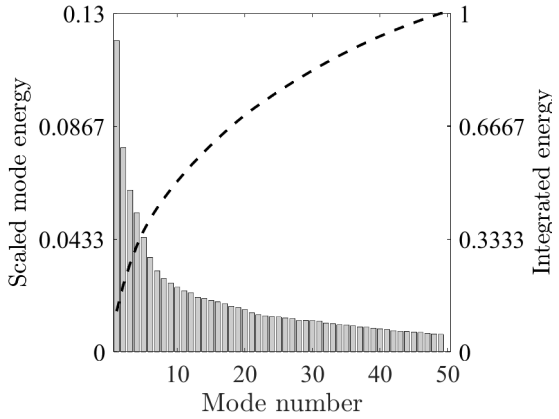

(f) Modal Energies

Figure B.13: Nitrogen-Nitrogen 3/8 inch nozzle POD modes, P_e/P_{02} =0.7.

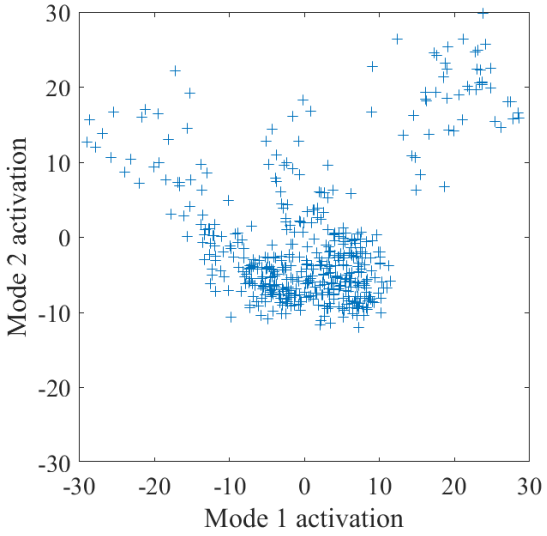

Figure B.14: Modal activation coefficients for modes 1 and 2, Ni-Ni 3/8 inch nozzle, P_e/P_{02} =0.7.

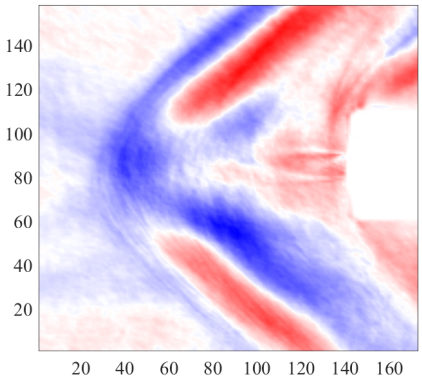

(a) Mode 1

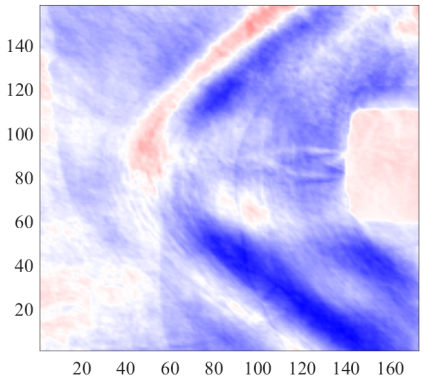

(b) Mode 2

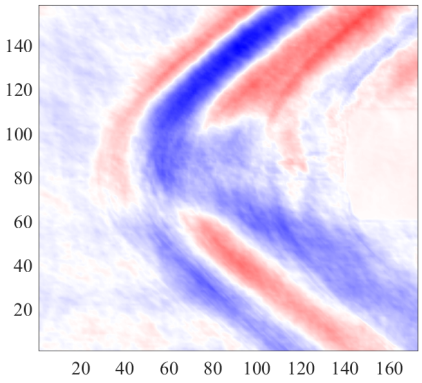

(c) Mode 3

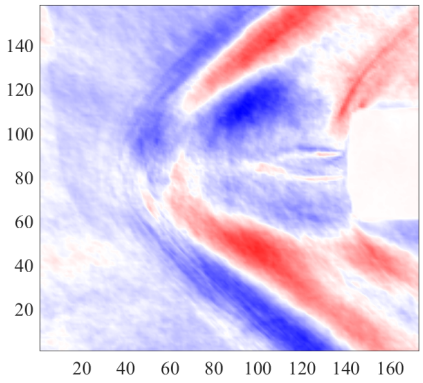

(d) Mode 4

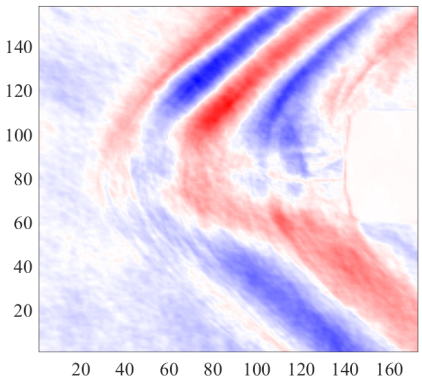

(e) Mode 5

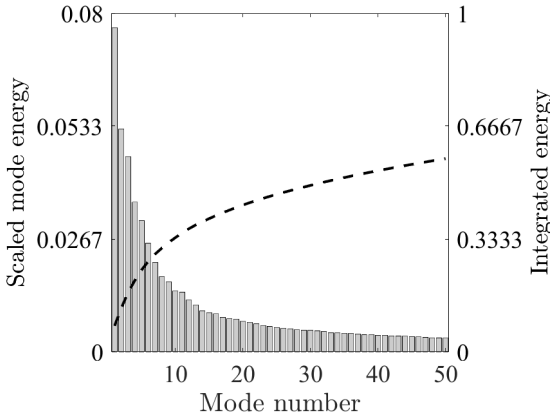

(f) Modal Energies

Figure B.15: Nitrogen-Nitrogen 3/8 inch nozzle POD modes, P_e/P_{02} =0.6.

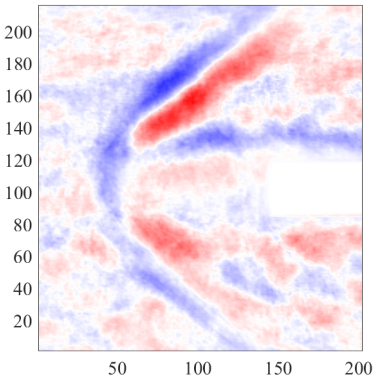

(a) Mode 1

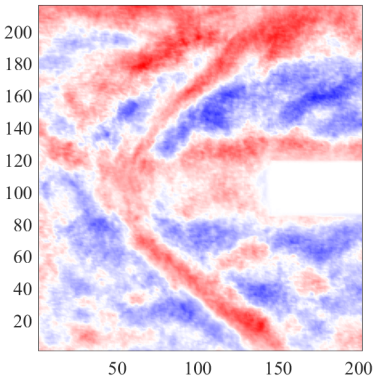

(b) Mode 2

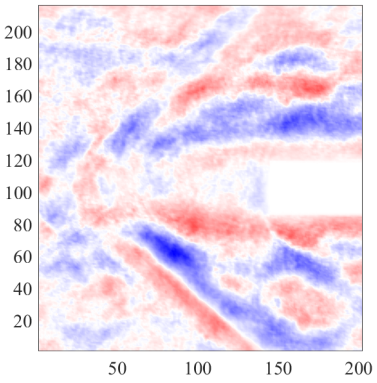

(c) Mode 3

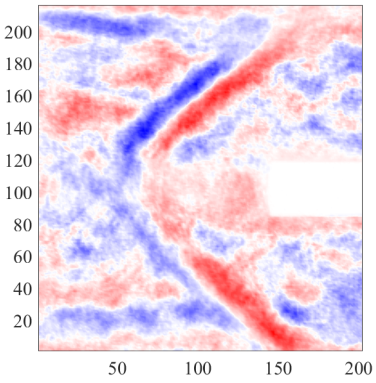

(d) Mode 4

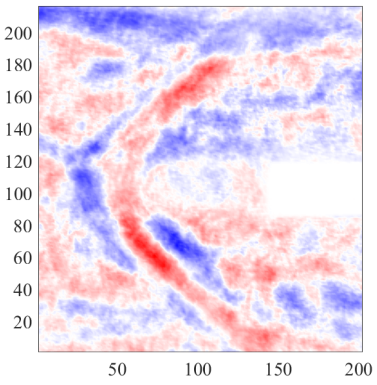

(e) Mode 5

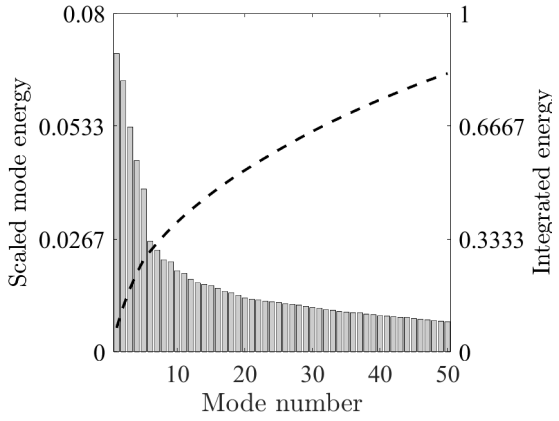

(f) Modal Energies

Figure B.16: Carbon Dioxide-Helium 1/4 inch nozzle POD modes.

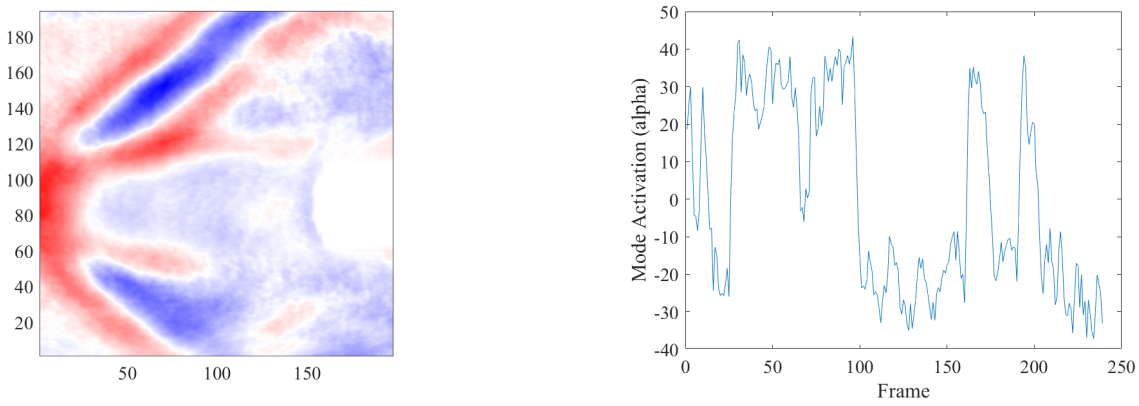

(a) Mode

(b) Mode activations

Figure B.17: Nitrogen-Nitrogen 1/4 inch nozzle POD modes.

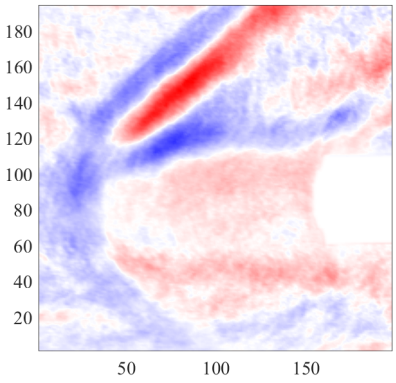

(a) Mode 1

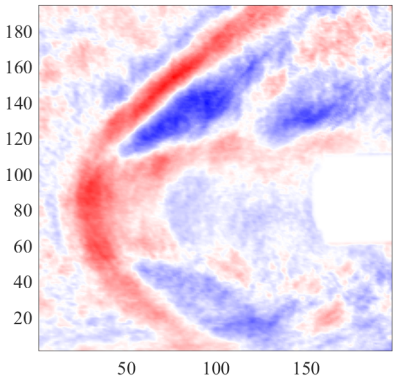

(b) Mode 2

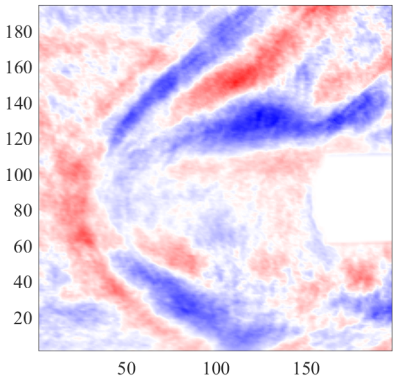

(c) Mode 3

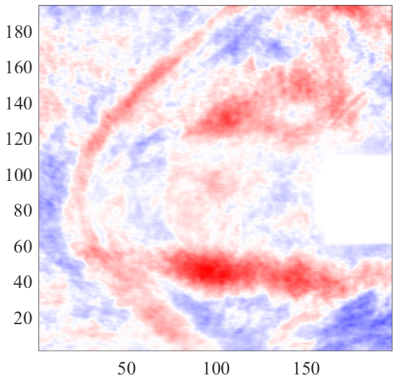

(d) Mode 4

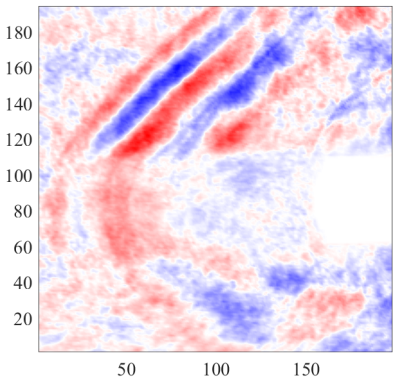

(e) Mode 5

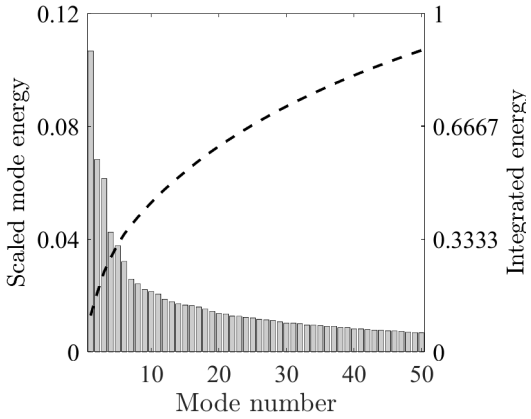

(f) Modal Energies

Figure B.18: Carbon Dioxide-Helium 3/8 inch nozzle POD modes, unsteady type 1.

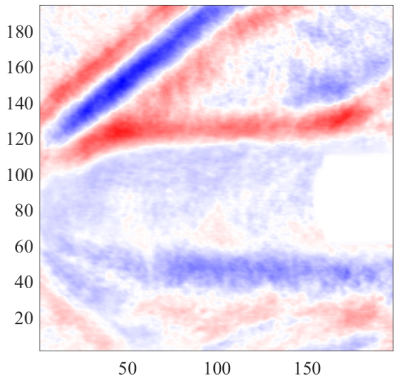

(a) Mode 1

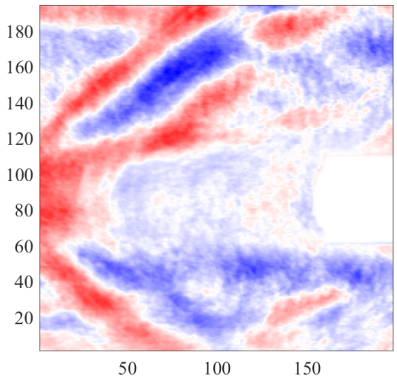

(b) Mode 2

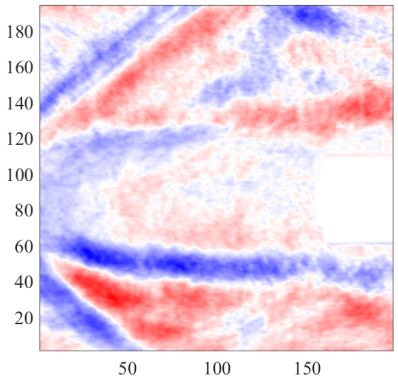

(c) Mode 3

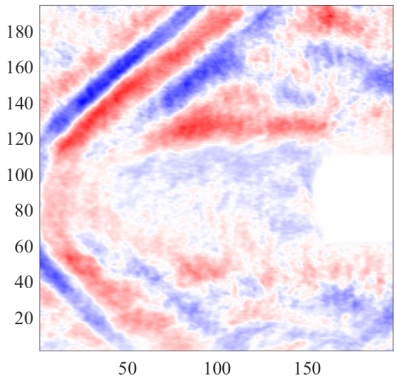

(d) Mode 4

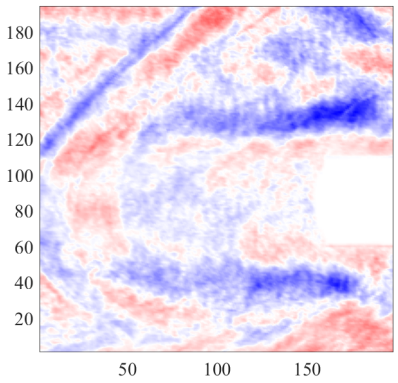

(e) Mode 5

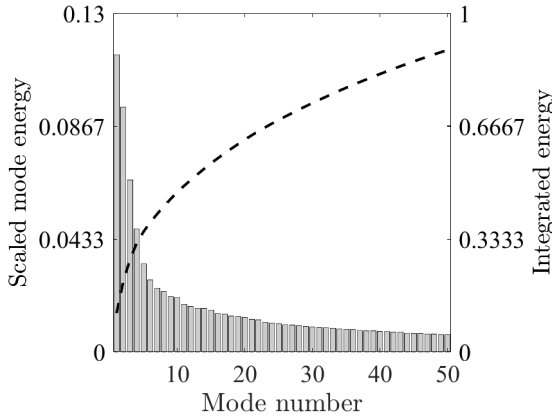

(f) Modal Energies

Figure B.19: Carbon Dioxide-Helium 3/8 inch nozzle POD modes, unsteady type 2.

Appendix C

ADDITIONAL FIGURES, NASA DATASET

(a) Mode (b) Mod

Figure C.1: 253

(a) Mode (b) Mod

Figure C.2: 171

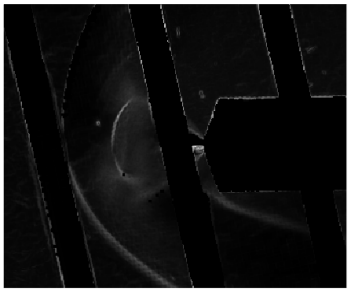

(a) Mode

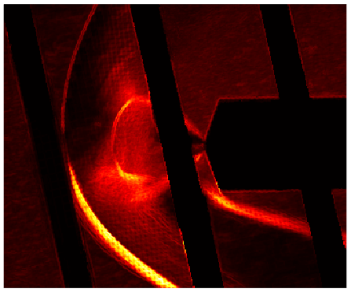

(b) Mod

Figure C.3: 318

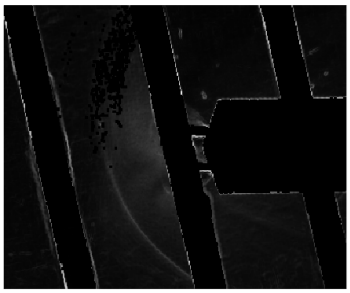

(a) Mode

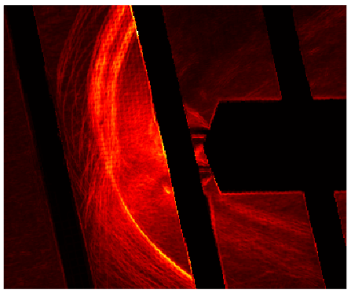

(b) Mod

Figure C.4: 194

(a) Mode

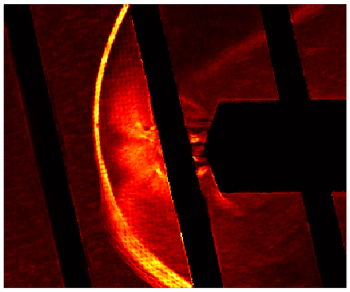

(b) Mod

Figure C.5: 288

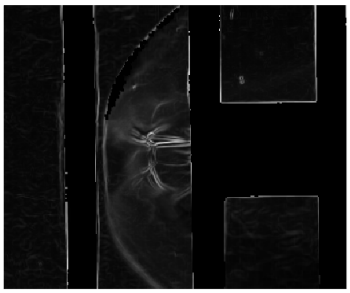

(a) Mode

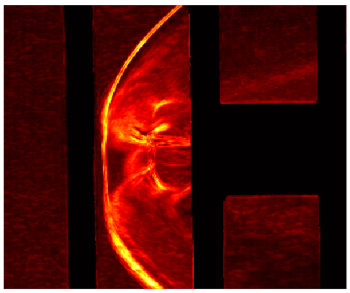

(b) Mod

Figure C.6: 306, Ct 2

(a) Mode (b) Mod

Figure C.7: 306, Ct3

(a) Mode (b) Mod

Figure C.8: 139, α=0°

(a) Mode (b) Mod

Figure C.9: 139, α=4°

(a) Mode (b) Mod

Figure C.10: 139, α=8°

(a) Mode (b) Mod

Figure C.11: 139, α=12°

(a) Mode (b) Mod

Figure C.12: 139, α=20°

(a) Mode (b) Mod

Figure C.13: 286, Ct 0.5

(a) Mode (b) Mod

Figure C.14: 286, Ct 1

(a) Mode (b) Mod

Figure C.15: 286, Ct 2

(a) Mode (b) Mod

Figure C.16: 202

(a) Mode

(b) Mod

Figure C.17: 266

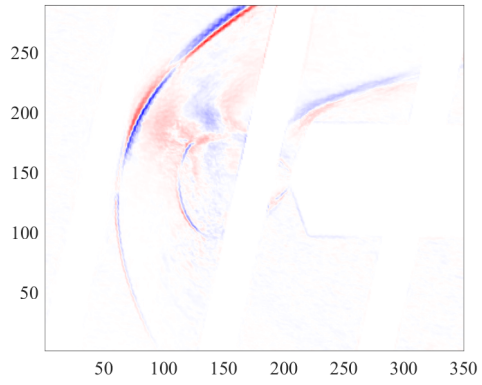

(a) Mode 1

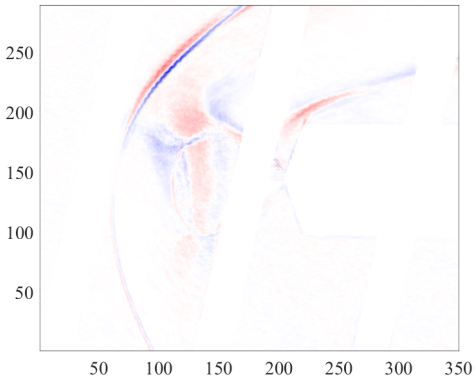

(b) Mode 2

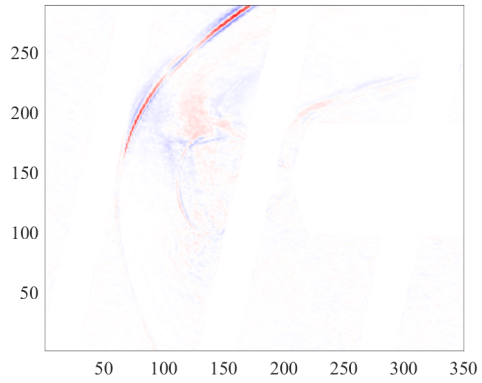

(c) Mode 3

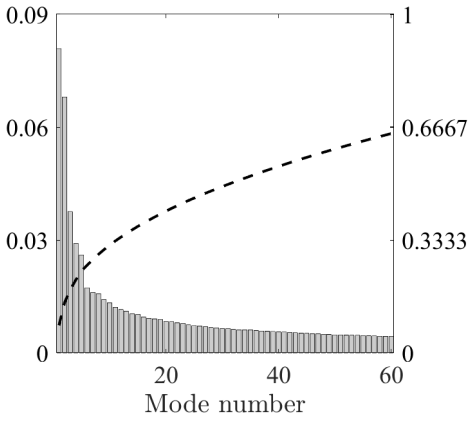

(d) Modal Energy Distribution

Figure C.18: Case 318: Center nozzle Mach 2, C_T 2, α=12°.

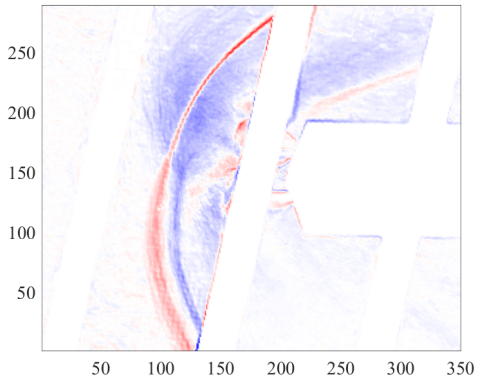

(a) Mode 1

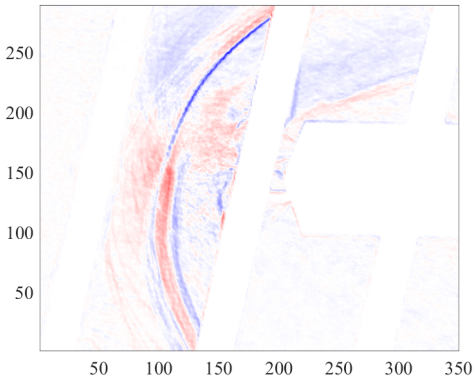

(b) Mode 2

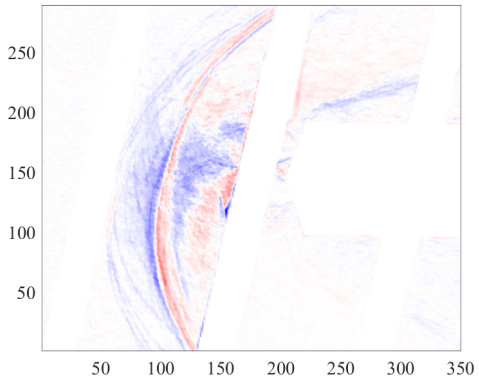

(c) Mode 3

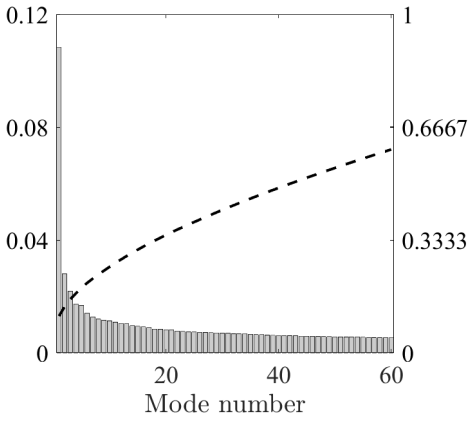

(d) Modal Energy Distribution

Figure C.19: Case 194: Tri-nozzle, Mach 2, C_T 2, α=12°

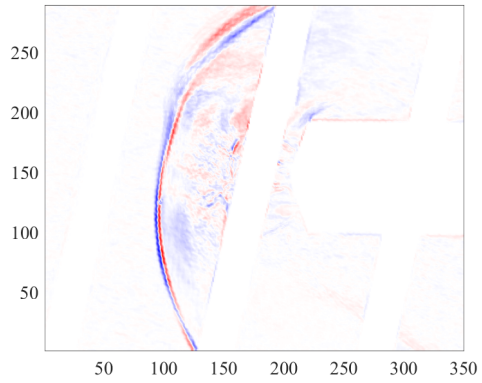

(a) Mode 1

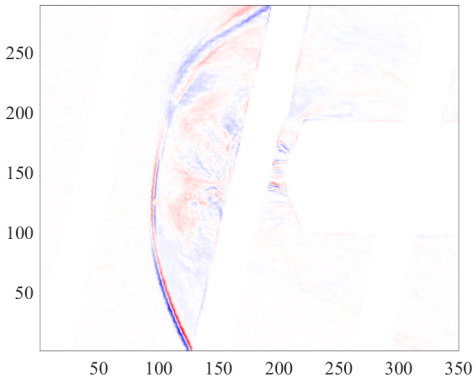

(b) Mode 2

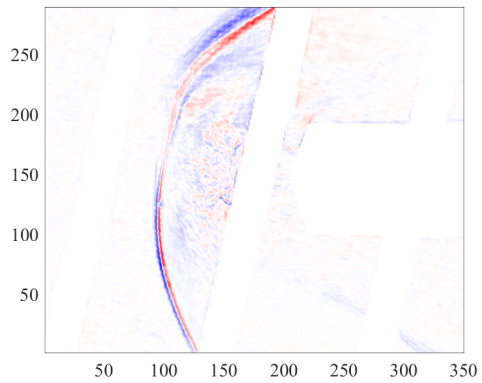

(c) Mode 3

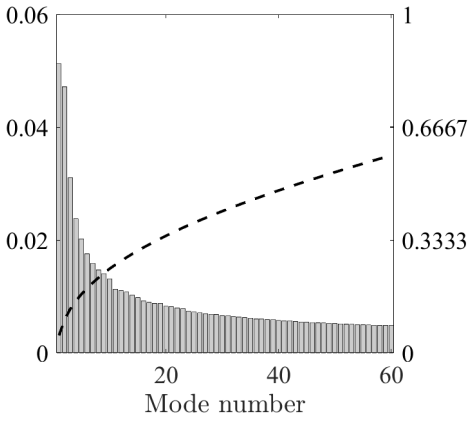

(d) Modal Energy Distribution

Figure C.20: Case 288: Quad nozzle, Mach 2, C_T 2, α=12°

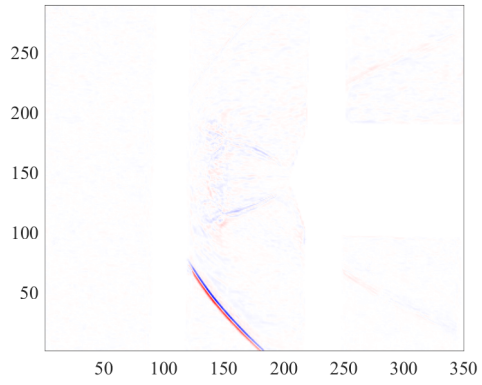

(a) Mode 1

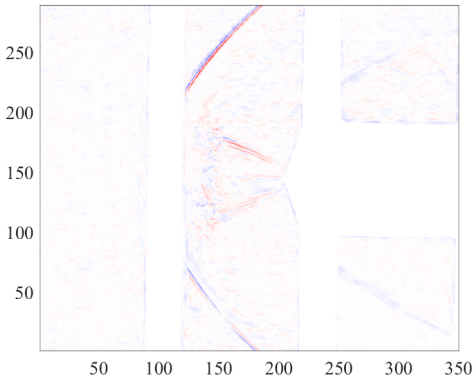

(b) Mode 2

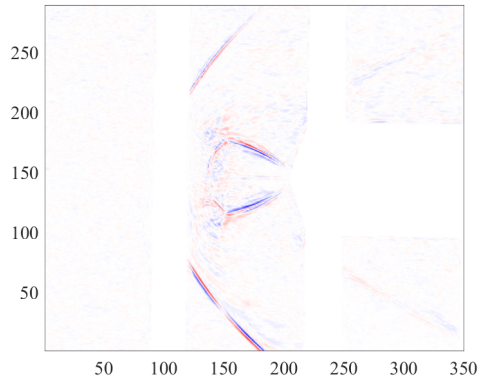

(c) Mode 3

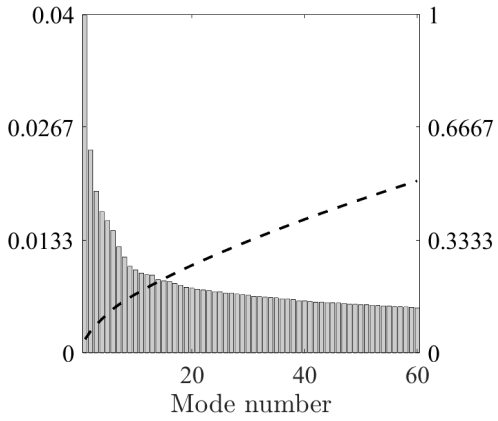

(d) Modal Energy Distribution

Figure C.21: Case 139: Center nozzle, Mach 2, C_T 1, α=0°

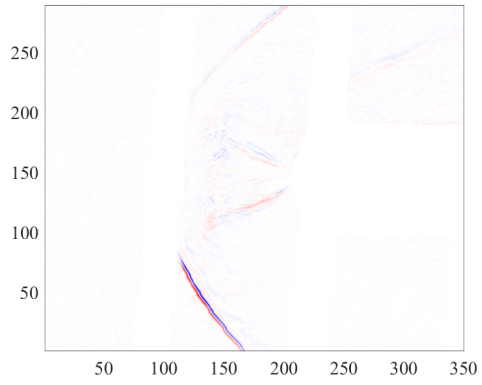

(a) Mode 1

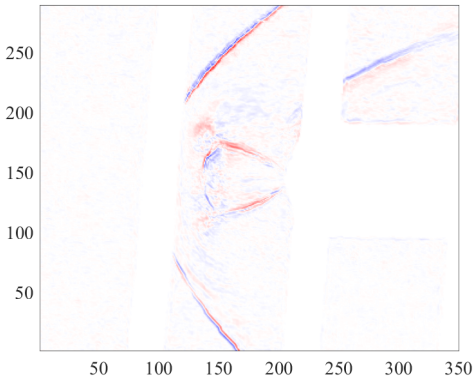

(b) Mode 2

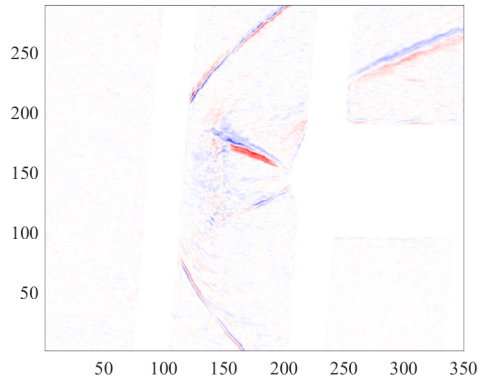

(c) Mode 3

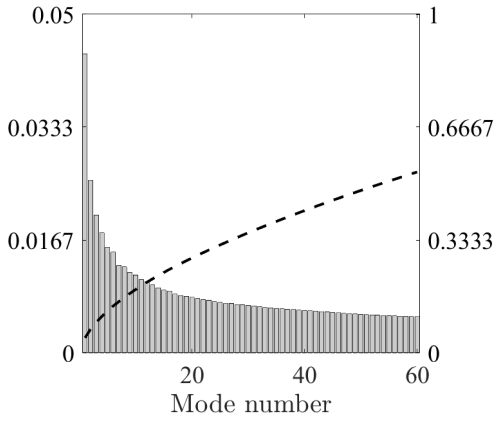

(d) Modal Energy Distribution

Figure C.22: Case 139: Center nozzle, Mach 2, C_T 1, α=4°

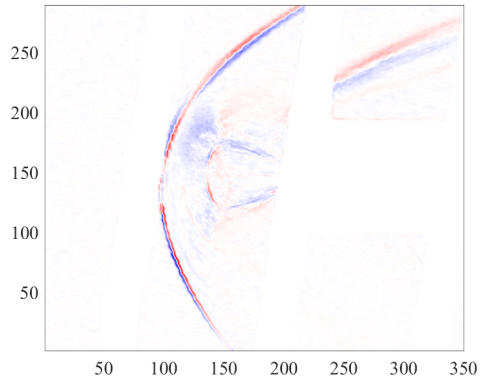

(a) Mode 1

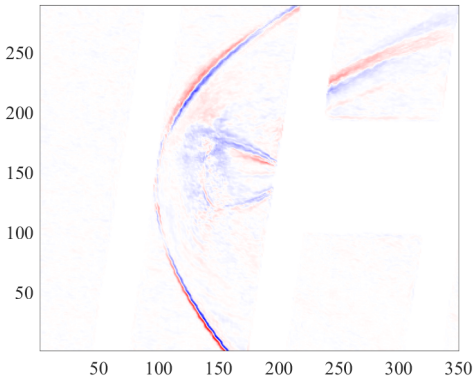

(b) Mode 2

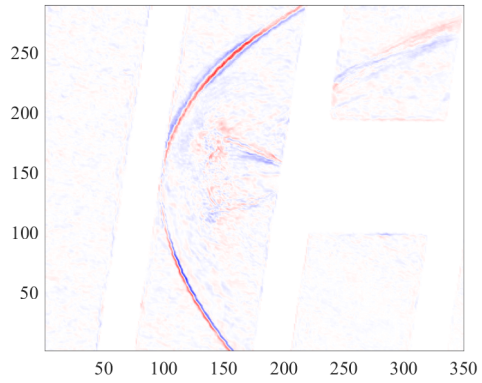

(c) Mode 3

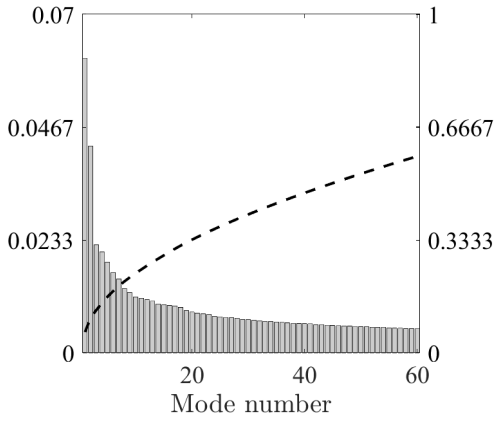

(d) Modal Energy Distribution

Figure C.23: Case 139: Center nozzle, Mach 2, C_T 1, α=8°

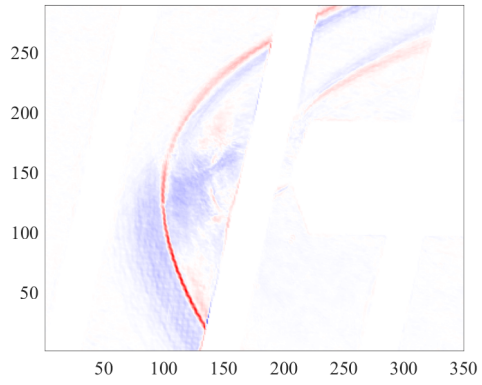

(a) Mode 1

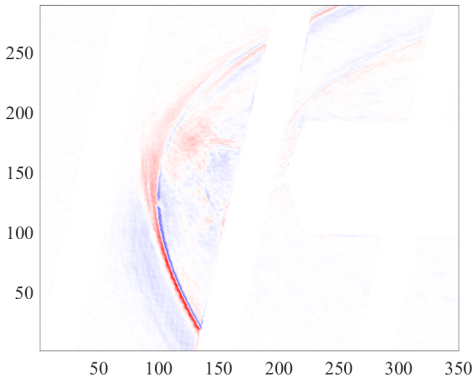

(b) Mode 2

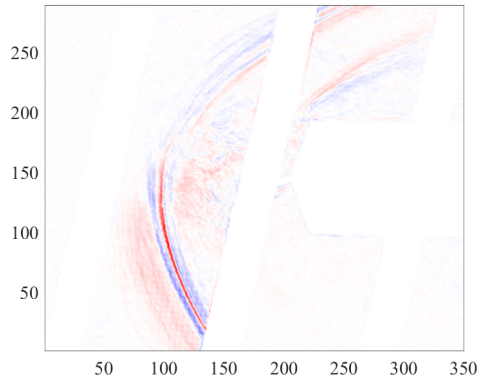

(c) Mode 3

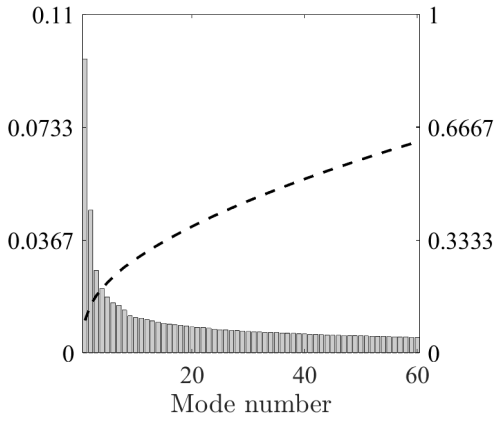

(d) Modal Energy Distribution

Figure C.24: Case 139: Center nozzle, Mach 2, C_T 1, α=12°

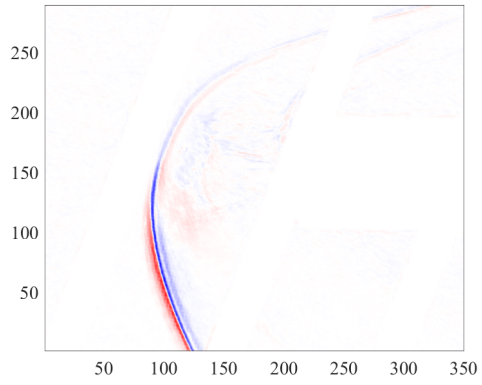

(a) Mode 1

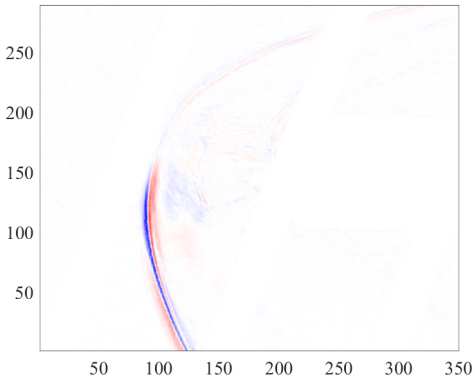

(b) Mode 2

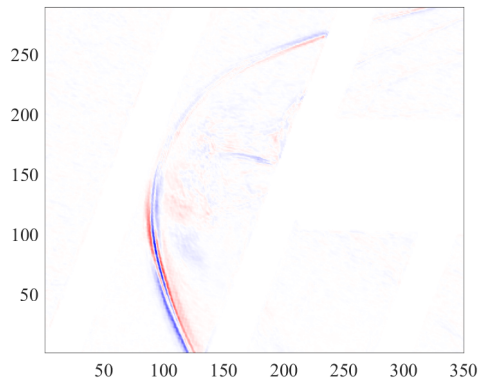

(c) Mode 3

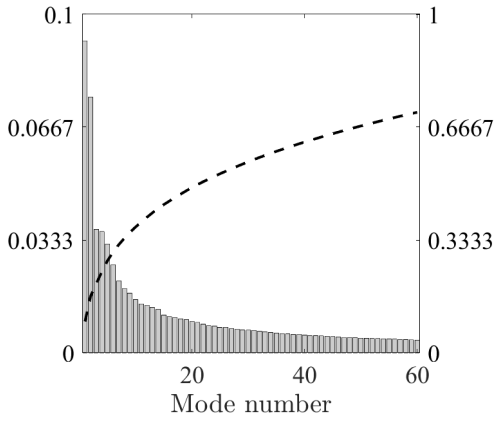

(d) Modal Energy Distribution

Figure C.25: Case 139: Center nozzle, Mach 2, C_T 1, α=20°

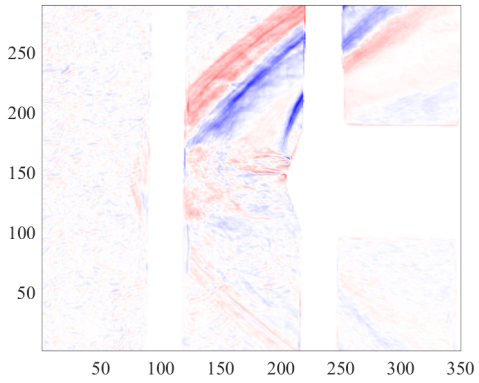

(a) Mode 1

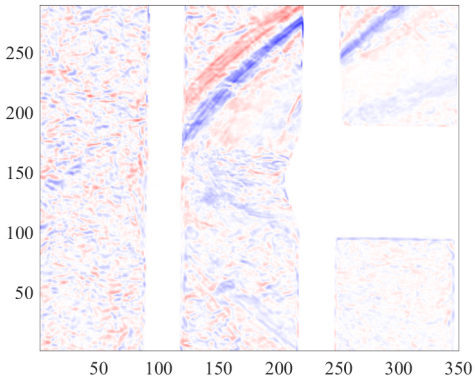

(b) Mode 2

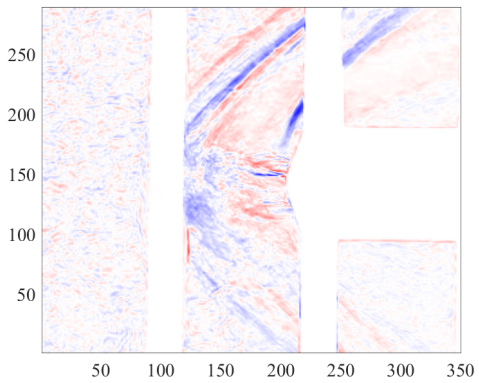

(c) Mode 3

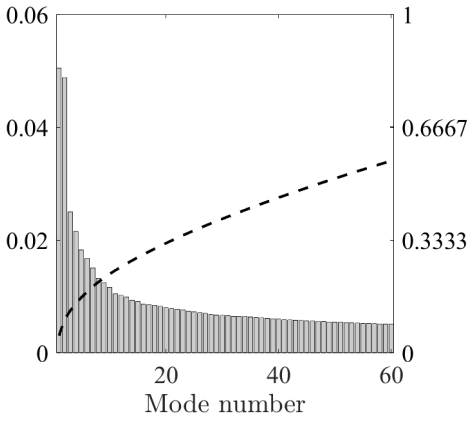

(d) Modal Energy Distribution

Figure C.26: Case 286: Quad nozzle, Mach 2, C_T 0.5, α=0°

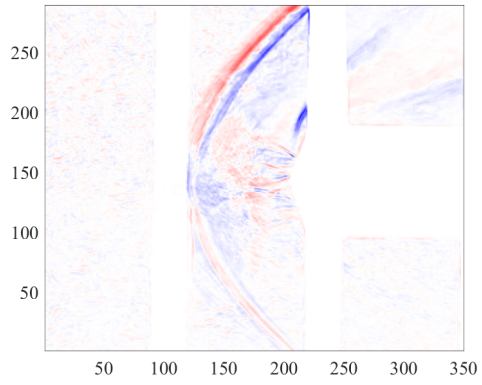

(a) Mode 1

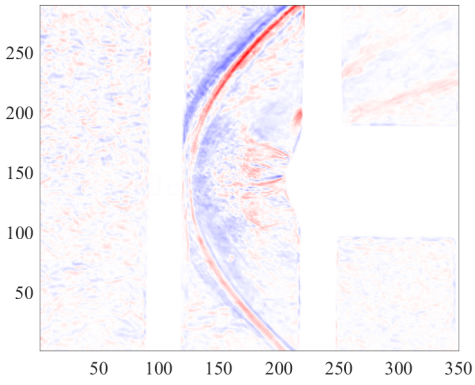

(b) Mode 2

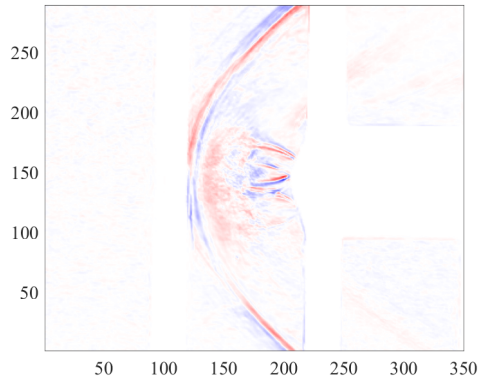

(c) Mode 3

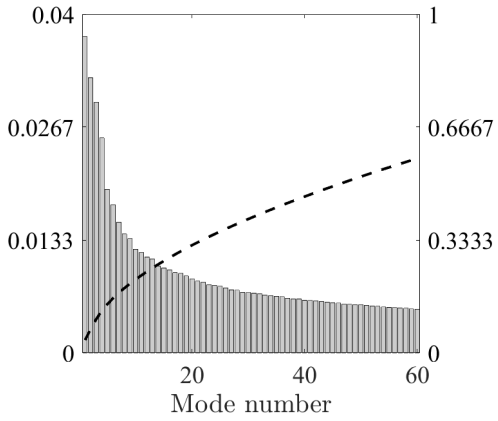

(d) Modal Energy Distribution

Figure C.27: Case 286: Quad nozzle, Mach 2, C_T 1, α=0°

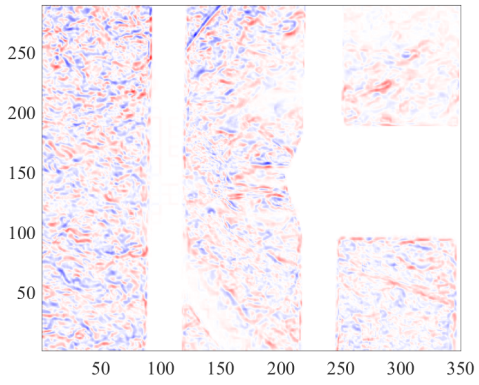

(a) Mode 1

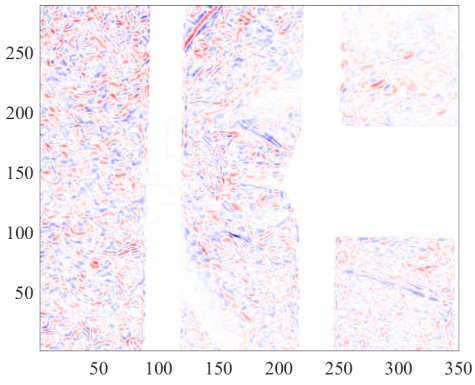

(b) Mode 2

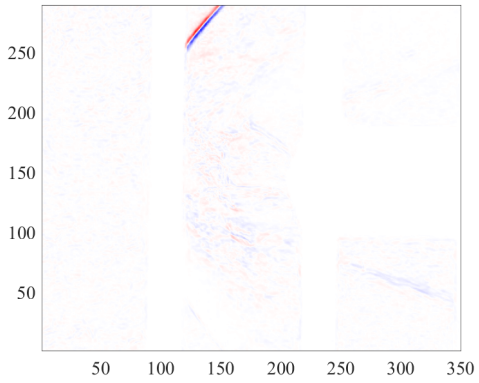

(c) Mode 3

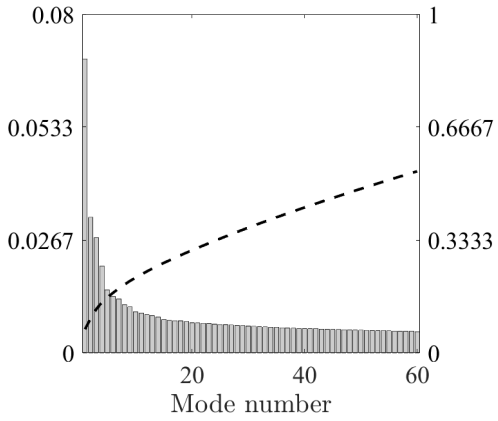

(d) Modal Energy Distribution

Figure C.28: Case 286: Quad nozzle, Mach 2, C_T 2, α=0°

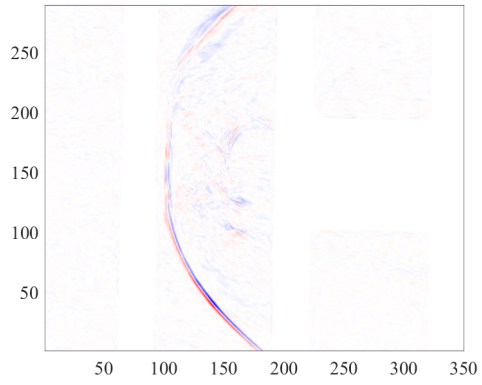

(a) Mode 1

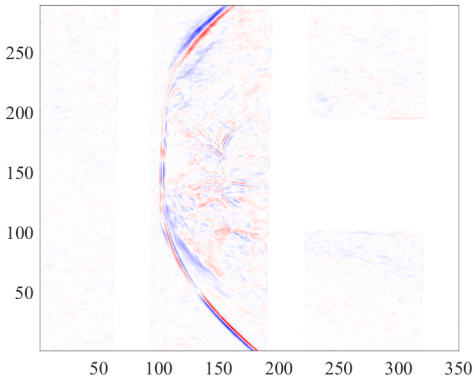

(b) Mode 2

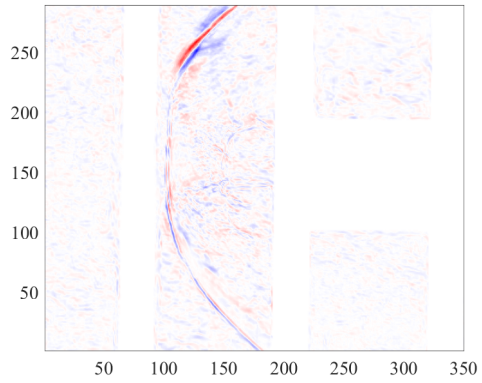

(c) Mode 3

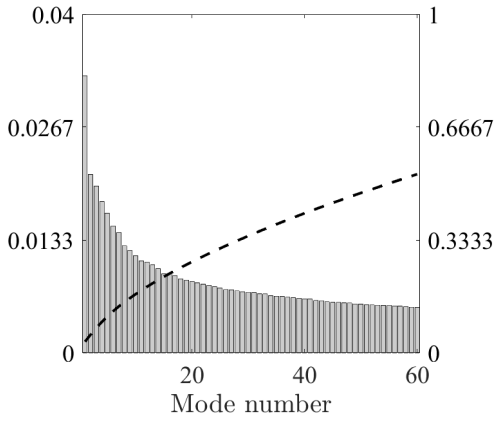

(d) Modal Energy Distribution

Figure C.29: Case 306: Quad nozzle, Mach 3, C_T 2, α=0°

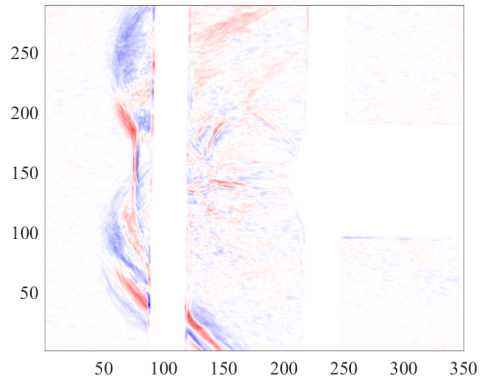

(a) Mode 1

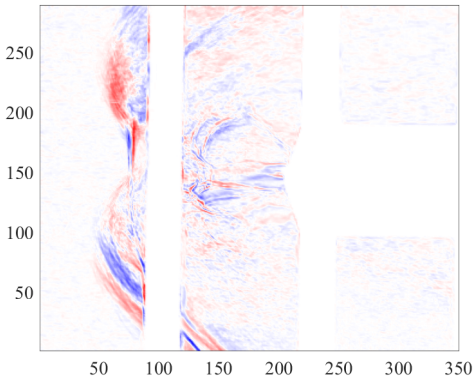

(b) Mode 2

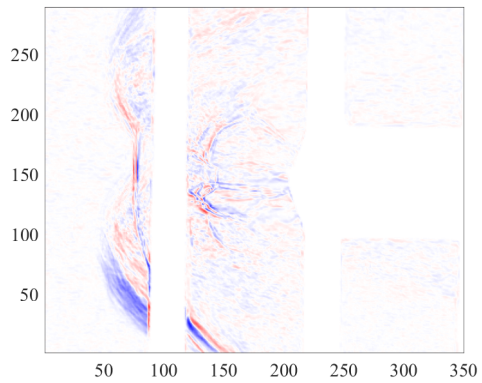

(c) Mode 3

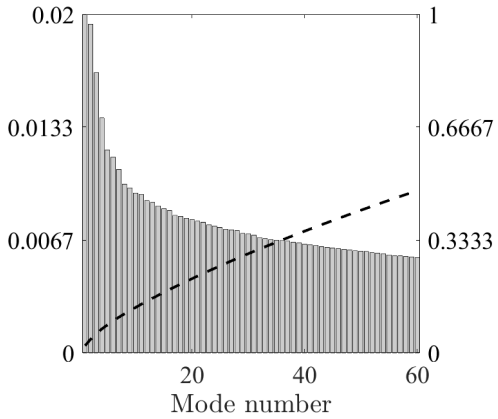

(d) Modal Energy Distribution

Figure C.30: Case 306: Quad nozzle, Mach 3, C_T 3, α=0°

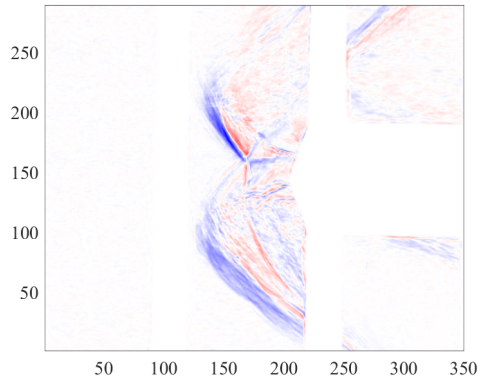

(a) Mode 1

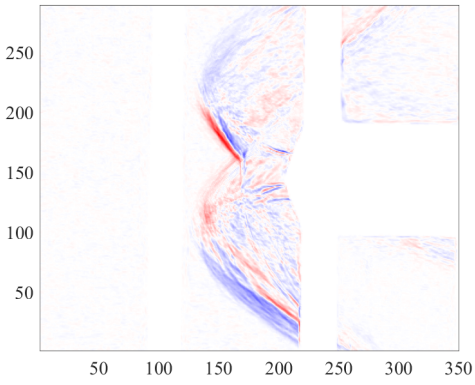

(b) Mode 2

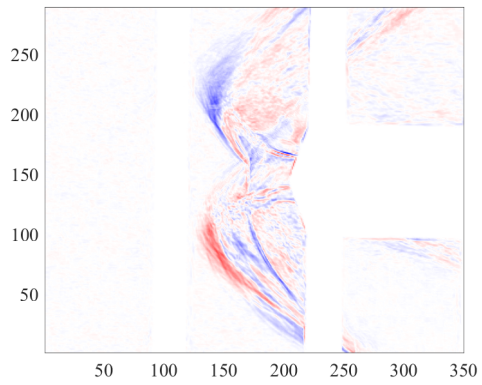

(c) Mode 3

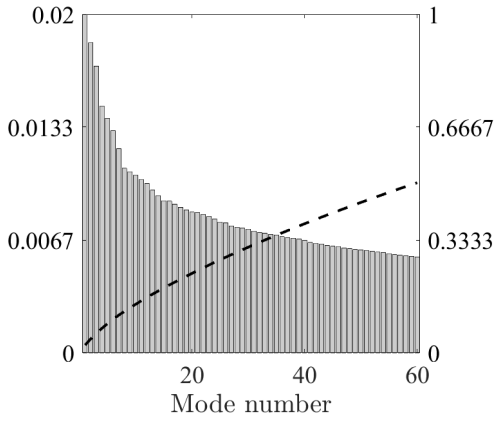

(d) Modal Energy Distribution

Figure C.31: Case 202: Tri nozzle, Mach 2, C_T 0.5, α=0°

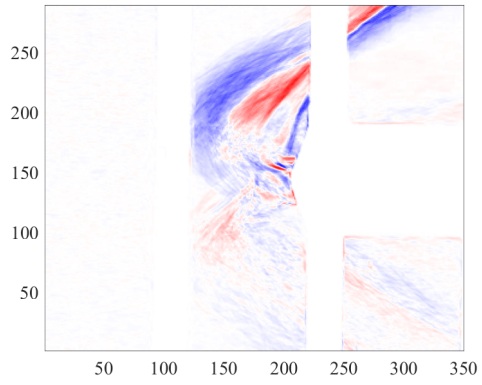

(a) Mode 1

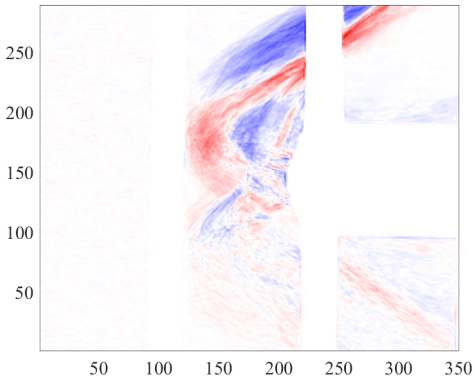

(b) Mode 2

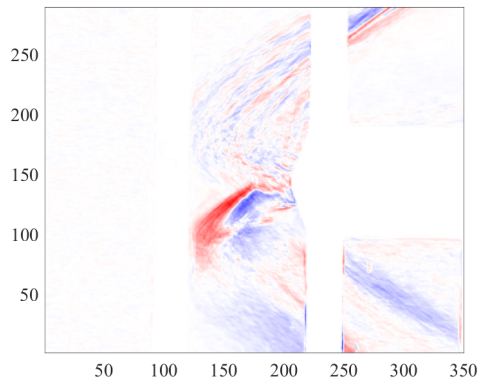

(c) Mode 3

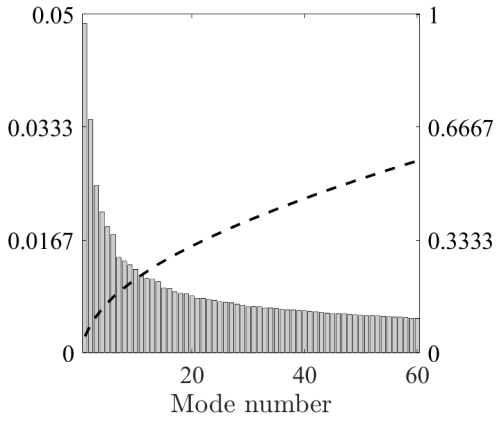

(d) Modal Energy Distribution

Figure C.32: Case 266: Tri nozzle, Mach 3, C_T 0.5, α=0°

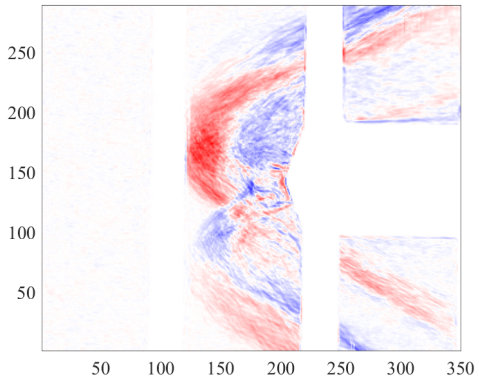

(a) Mode 1

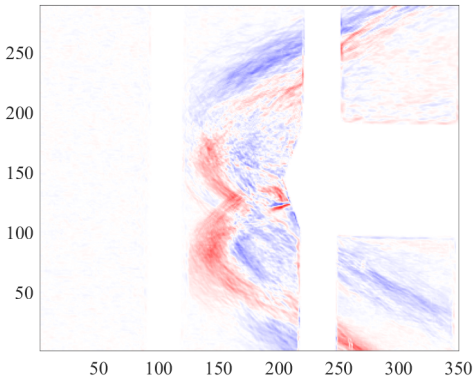

(b) Mode 2

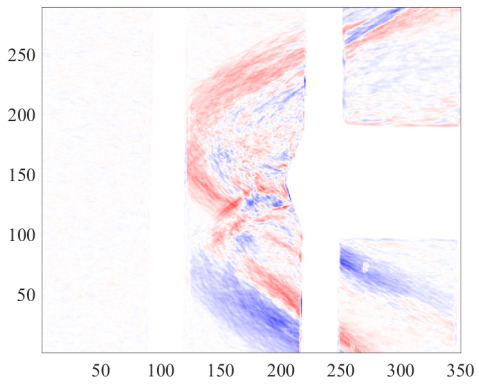

(c) Mode 3

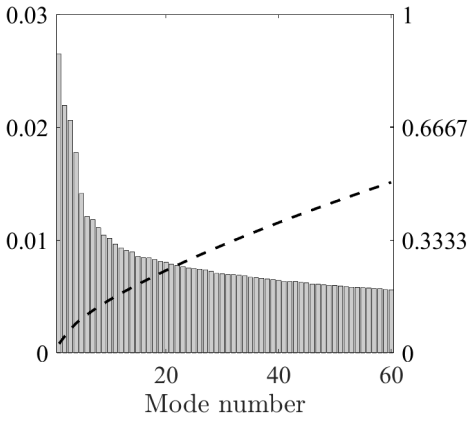

(d) Modal Energy Distribution

Figure C.33: Case 253: Tri nozzle, Mach 4, C_T 0.5, α=0°